



Flexible and Spectrum Aware Radio Access through Measurements and Modelling in Cognitive Radio Systems

FARAMIR

Document Number D4.2

Neighbourhood Mapping Technology and Algorithm Report

Contractual date of delivery to the CEC:	31.10.2011
Actual date of delivery to the CEC:	31.10.2011
Project Number and Acronym:	248351 - FARAMIR
Editor:	Ioannis Dagres, Andreas Polydoros (IASA)
Authors:	Ioannis Dagres (IASA), Natalia Miliou (IASA), Andreas Polydoros (IASA), Jad Nasreddine (RWTH), Jaap van de Beek (HWSE), Sun Guolin (HWSE), Berna Sayrac (FT), Sebastien Grimoud (FT), Marko Angjelinoski (UKIM), Daniel Denkovski (UKIM), Valentin Rakovik (UKIM), Vladimir Atanasovski (UKIM), Liljana Gavrilovska (UKIM)
Participants:	IASA, RWTH, HWSE, FT, UKIM
Workpackage:	WP4
Security:	PU
Nature:	R
Version:	1.0
Total number of pages:	95

Abstract:

This deliverable documents various techniques and methodologies suitable for radio field estimation and source characterization/localization (also known as “neighborhood mapping”), all of which are critical entries in a dynamic REM. In the process of researching these topics, a number of important results have been obtained:

- A new framework for source detection and approximate localization has been proposed, based on a rather simple idea: first estimate appropriately-chosen parameters and then use the results to perform detection (a reversal of usual thinking). A highly accurate approximate analysis of the proposed test has been provided, enabling performance characterization and optimization.
- It was also shown that it is possible to identify the AOAs of multiple distinct paths, all emanating from a single source, which arrive at a passively-receiving array in different temporal “energy piles”. This is possible via a two-stage processing approach, and this can be achieved regardless of whether there is training-data information or not (i.e., it can be done blindly).
- A technique for obtaining field estimation via Maximum Likelihood in a shadow-fading environment has been derived, involving localization and power estimation of an unknown number of sources in a given band.
- A direct field-estimation approach has been explored based on the recently-popular method of *compressed sensing* (sparsity), applied for the scenario of LTE in TVWS.
- Another direct field-estimation method has been proposed based on a Gaussian model, whereby estimation is performed under a Bayesian framework for incorporating partial information. This method was applied for a scenario of self-configuring and self-optimizing femto-cells.
- Finally, an analysis and related comparisons of three different interpolation techniques were presented. These were the ordinary Kriging interpolation, the Inverse Distance Weighting (IDW) modified Shepard’s method and the gradient plus Inverse Distance Squared (GIDS) method. A comparison was performed for both indoor and outdoor scenarios.

Overall, a number of novel and promising approaches have been laid out, examined in greater detail and assessed on selected application scenarios.

Keywords: Detection, Localization, Radio Interference Field Estimation, Neighbourhood mapping

Document Revision History

<i>Version</i>	<i>Date</i>	<i>Author</i>	<i>Summary of main changes</i>
0.1	19.7.2011	IASA	TOC
0.5	28.9.2011	IASA, HWSE, FT	Joint detection/localization, Joint localization + Tx power estimation, LTE in TVWS + Reconstruction techniques, Bayesian methods for indirect RIFE for in-band femto
0.6	14.10.2011	UKIM	Interpolation techniques for direct RIFE
0.7	17.10.2011	IASA, HWSE, UKIM, RWTH	AoA estimation, experimental results for LTE in TVWS, Dynamic spectrum access in cellular networks, Introduction initial contribution for Fusion techniques
0.8	26.10.2011	IASA, UKIM, FT	Restructuring of chapter 3, Fusion section, Introduction, Edits
0.9	27.10.2011	IASA	Final edits
1.0	31.10.2011	Janne Riihijärvi (RWTH)	Integration of final edits and contributions for delivery to EC
1.0f	31.10.2011	Petri Mähönen (RWTH)	Coordinator review and approval

Table of Contents

1	Introduction	6
2	Source characterization: detection, parameter estimation and localization	11
2.1	Introduction	11
2.2	Noise-Robust source detection based on ranging-parameter estimation	12
2.2.1	State of the Art on source detection and proposed approach.....	12
2.2.2	Description of the proposed test.....	14
2.2.3	Performance assessment.....	17
2.3	Angle-of-Arrival estimation in dense multi-path environments.....	24
2.3.1	State of the Art on AoA estimation and proposed approach.....	24
2.3.2	Description of the proposed estimator	25
2.3.3	Performance assessment.....	33
2.4	Fusion methods for localization	37
2.4.1	Introduction to fusion methods.....	37
2.4.2	Description of basic fusion methods.....	37
2.4.3	Performance assessment.....	40
2.5	Joint transmit power estimation and localization	42
2.5.1	State of the Art and model description	42
2.5.2	Algorithm description	43
2.5.3	Performance assessment.....	44
3	Spatial interpolation techniques for RIFE.....	58
3.1	Introduction	58
3.2	Description of proposed techniques	60
3.2.1	The Kriging interpolation	60
3.2.2	Inverse Distance Weighting modified Shepard's interpolation	63
3.2.3	Gradient plus Inverse Distance Squared interpolation	64
3.2.4	Compressed Sensing Techniques	65
3.3	Performance assessment	69
3.3.1	Indoor (WLAN) and Outdoor (GSM) scenario investigation.....	69
3.3.2	An in-band femto-cell urban scenario.....	73
3.3.3	Compressed-sensing techniques for LTE in TVWS	77

4	Conclusions.....	85
5	Appendix – Derivations from Section 3.2.1.2.....	87
	References.....	92

1 Introduction

A major innovative dimension of FARAMIR is the use of advanced signal-processing techniques performed cooperatively between sensors, based on real-time measurements on the ground, in order to derive and exploit spatial information about various radio emitters and their effect on the observable spectrum. These radio emitters are presumed scattered *in the neighborhood* of the sensing devices, thus enabling the concept of *neighborhood mapping*. The goal of such processing is to empower, update and enhance the content of the radio environment maps (REMs) in the said locality. Here we assume non-cooperative (passive) reception by the sensors, meaning that the emitting sources under identification cannot be interrogated as to their location. The processors/sensors will exploit whatever reception and signal-processing resources they have residing with them, and make inference based on whatever is received by them in a particular bin of the time/frequency plane.

The search range in frequency ("spectral band") will be assumed common and known to all sensors. Furthermore, we assume sufficient temporal synchronization among all sensors, such that both the window of observed interval is commonly known and agreed upon by all but also, if the technique requires it, sufficient common-clock accuracy is provided for time-stamping of time-of-arrival-based techniques. Although a robustness analysis may eventually be needed to assess the impact of imperfections in these assumptions, it is commonplace to assume that these are satisfied at an adequate level for the applications at hand. After all, source location and neighborhood mapping for purposes of REM updates and spectral access are not critically dependent on super-resolution accuracy¹; a decent level of accuracy suffices to assess the effect of radio propagation and interference maps for the class of envisioned applications.

The use of radio features of a received waveform in order to locate either an emitter or a receiver is by now standard practice. Position location is a major source of application-space innovation and is used extensively; anyone familiar with the GPS in their phone will attest to that. As a result, the literature in books, papers and documents is very rich. Still, the sensing requirement of cognitive radio raises challenging faces not typically encountered in these applications, and this is the direction of the present work in FARAMIR. In fact, a close look at the specifics of position-location mechanisms in commercial systems (cellular, satellite, etc.) reveal that the presumed environment is conducive to such mechanisms and the challenges are typically associated with implementation costs, hardware imperfections, efficiency of numerical solutions in the general processor and the like. For example, the source (the base station or handset, the access point, the satellite) is known to be there during the measurement (*no source detection* needed); it is known that only one radio source exists in the channel of interest and the time of interest for the processing at hand (*single-source problem*); the received signal strength is sufficiently above the noise after post-processing, i.e., at the decision-SNR level² (*high-SNR regime*); observations can be long, sometimes in many

¹ Military applications typically differ in that regard.

² The *decision-* or *output-SNR* should not be confused with the *Input SNR*. The former equals the latter times the time-bandwidth (TB) product, which is typically a very large number (it equals the number of processed

seconds or minutes; processing can be delay-tolerant; and, last but not least, the channels tend to be benign, as in Line-Of-Sight (LOS) conditions. Under these fairly lax assumptions, which are typically met in actual practice, solutions focus less on the sophistication of the signal processing and more on implementation advantages, as mentioned above.

Sensing in cognitive radio faces challenges that are a combination of difficulties insinuated above. To list a few:

- The presence of the sought signal is unknown and must be assessed by processing the data; that is, there is no point in attempting Root-Mean Squared Error (DSA) in a given band if the PU is known *a priori* to be there; the whole idea is to find out when it is *not* there and act. Detection, therefore, plays a critical role, and it is no accident that much of the sensing literature in CR has focused on the detection problem. This detection task is compounded by difficulties such as weak source signals, hidden nodes, and unknown or fluctuating noise floor (giving rise to the familiar phenomenon of the *SNR Wall* [6]), all of which make passive source detection a tough mission.
- Whereas commercial systems are not designed with multiple signals occupying the same time/frequency bin simultaneously³, this cannot be ruled out in cognitive radio. Multiple emitters may co-exist not only in a given band at different frequencies (a topic of intense research focus below), but also in a given band *at the same frequencies*. This raises the level of difficulty immensely, since other “dimensions of discrimination” must be sought to separate them (e.g., different directions/angles of arrival, thus demanding array-based/MIMO processing or equivalent spatial discrimination ability). The problem is compounded by the fact that the number of such sources is typically unknown also, necessitating tools from the “number-of-signals-estimation” literature.
- At a higher level, one has to discern exactly what a “signal” means in this context. There are always “signals” received, albeit weak, from a large number of sources dispersed in the universe around us; which type of signal do we exactly seek to isolate and find? This leads to notions of signal sorting, in conjunction to the other tasks above, thus compounding the problem even further.
- Ground propagation is far from LOS. There are ample, natural as well as man-made objects that reflect energy all around, giving rise to *multipath fading*. This is a very serious issue in ground-propagation modeling, and different localization techniques deal with it differently. Power-based measurements tend to collect all such reflected energy and process it, thus glossing over that aspect of the problem. Phase pseudo-coherent techniques (angle of arrival, time of arrival), which tend to be much more efficient due to their relative immunity to propagation statistics (shadowing), suffer significantly from the omission of the modeling and accounting of multipath. Although statistical and spatial-

samples, numbering in the thousands or millions). Thus, an input SNR of -30 dB (as in spread-spectrum systems) can be easily converted to +10dB decision-SNR.

³The exception being spread-spectrum/CDMA/3G, where however orthogonality is achieved at the code level at the expense of the bandwidth resource.

averaging techniques have been explored for countering this problem, it remains a major issue and source of major inaccuracy in the quest for source-neighborhood mapping.

- Estimating the radio field in a given area of interest is a problem germane to many cognitive-radio applications and a major entry of REM's, yet the technical challenge is significant because of the multi-dimensionality of the addressed space.

Addressing all the above challenges is a tall order; the field is huge and the technical difficulties real. Therefore, the philosophy developed in this project is to "peel the onion" one step at a time: Fundamentally new and original signal-processing techniques have been sought and developed that deviate from those well-studied in the literature. These techniques deal with one problem at a time, each within the respective challenging model identified above, at the depth afforded by the resources, providing a roadmap for further exploration and synthesis down the road. This way, the benefits accrued from the system-level integrated implementation of such techniques can provide a solid platform for truly enhanced localization and neighborhood mapping that can enrich the databases of the future. This is still "work in progress", but new results have already emerged that show major promise. To highlight:

- Power-based sensor measurements (of the type that is easiest to collect, with minimal hardware complexity) have been combined in a properly modeled shadow-fading environment in order to perform optimal (maximum-likelihood) multiple-source localization and transmit power estimation. This leads subsequently to radio-field estimation (in the indirect class of techniques) which is a major entry of REMs. In addition, the same technique is shown to be usable in an innovative way (via proper thresholding) for source-presence detection. This is a manifestation of a new approach whereby estimation results are employed for source-detection purposes⁴.
- Detailed multipath modeling is included in time-of-arrival and angle-of-arrival processing, distinct from classic correlation sub-space methods in arrays (e.g., MUSIC), which leads to enhanced-resolution maximum-likelihood estimation methodologies with strong results. The pathology of sub-space-based methods to same-source (i.e., totally correlated) paths is thus eliminated.
- The challenge of the SNR Walls in classic sensing is shown to be eliminated in a novel class of feature-based detectors which *skip power dependence altogether*. This is a significant advance, both conceptually (using the statistics of features such as TOA/TAOA for source detection has not to the best of our knowledge been explored before) but also practically, in that the need to know well and with minimal ambiguity the noise level, due to thermal and man-made noise and extraneous interference, in order to perform satisfactory and robust detection is a demanding assumption; therefore, the ability to overcome this requirement raises intriguing possibilities.
- The high resolution and robustness of individual signal processing/sensing techniques is combined with appropriately defined geometric engines for a final answer in localization

⁴ The classical paradigm being that you first detect and then estimate.

(what is called herein “fusion methods”), providing high-quality results for the problem at hand.

- Elaborate techniques for field estimation have been constructed, based on the ML principle, with parallel efforts to reign into the associated computational complexity.

In accordance with the above, the present deliverable is structured as follows:

First, we draw a distinction between methodologies that account for the existence of signal sources *explicitly* and proceed to perform inference on them: detect their presence, estimate their number, their location (also termed “localization”), their parameters (including emission power) and, finally, the radio effect they induce in their space (the “field” they induce); this is all described in Chapter 2. In contrast to that, Chapter 3 describes methodologies that do not account for the source(s), namely the so-called *direct* methods for field estimation.

Regarding Chapter 2, first single-source detection is described via the new methodologies introduced (“estimation-based detection”) and the SNR-uncertainty benefits detailed. We show how an SNR wall no more exists and performance improves monotonically with collected record length. This necessitates temporal parameter estimation and inter-sensor cooperation, as described.

Subsequently, maximum-likelihood methods are presented for operation in significant multipath. The formulation is general and assumes a calibrated array, thus yielding both AOA as well as TOA information (to be precise, inter-path temporal information). The ability to detect with precision the many angles emanating from a single source via multiple paths leads to the ability to identify the leading path (also known as Line of Bearing—LOB) and subsequently perform LOB-based positioning. Although the current formulation is for a single source creating multiple impinging planes, the extension to multiple sources is theoretically straightforward (albeit conjectured to be computationally intensive). We briefly mention sub-space methods (MUSIC) that can indeed yield multiple LOBs for multiple distinct sources, but with the caveat that these methods are multipath-sensitive and in general not recommended for on-the-ground propagation (unless the sources are high up and not subject to significant multipath). Thus, the research front of ML-based array processing for multiple sources on the ground remains a further goal.

The above methods rely on pseudo-coherent processing of features, all of which require estimation of the complex gains associated with the source under consideration (hence the term “pseudo-coherent”). This leads, however, to the estimation of significant features of spatial (angle), temporal (time of arrival) or mixed (angle/time) nature. We show how these estimates can lead to localization via the deployment of proper “engines” or fusion centers. Because this last field is vast, we confine our expose to selective methods. We note, however, that there is space for improvement here also, particularly in view of the generation and exploitation of soft quality metrics of the estimated parameters.

We then proceed in the next section to address measurements that are not pseudo-coherent as those above; instead, they are fully non-coherent and rely on power measurements. The question

is then what can be assessed in a non-coherent regime. As mentioned, the benefits of these approaches center on their simplicity; power in a band is fairly straightforward to measure. On the other hand, their sensitivity to the propagation regime is also known. Nonetheless, a detailed statistical modeling of the shadowing offers an avenue towards advanced maximum-likelihood-based methods for multi-source localization, power estimation and, indirectly, presence-detection (under an assumption of a known minimum transmission level). These techniques address Radio-Interference Field Estimation-RIFE (RIFE) in what can be viewed as indirect methodology. RIFE is also known in the literature as Interference Cartography and represents the Power Spectral Density (PSD) of an RF environment as a function of spatial coordinates in a pre-defined area and, possibly, time (for a dynamic environment). We also note that an alternative route to source detection is based on simple power measurements (but with sensitivity to propagation characteristics) plus all the intermediate steps required for field estimation. The advantage of the methodology here is that multiple co-existing sources can be detected, all at once. The corresponding task (multi-source detection) for temporally-based only features is not yet formulated due to the implied need to perform Multi-User Detection⁵ (MUD) of spectrally overlapping sources, a computationally intensive task⁶. We relegate this aspect of source detection to the chapter detailing field estimation via power measurements, since it is a direct by-product.

A related but philosophically different approach is followed in Chapter 3, namely *direct* field estimation (i.e., without resorting to source identification). Spatial interpolation comprises the essence of the direct method for estimating the RIFE, in contrast to the indirect one examined before. There is a variety of methods which target spatial interpolation and which have been exploited in different scientific and research areas. In general, all these interpolation methods can be divided into four main groups: (1) local neighborhood approaches, (2) geo-statistical approaches, (3) variational interpolation approaches and (4) compressed sensing. Four different spatial interpolation methods are proposed and assessed for direct RIFE. More specifically the scenarios under investigation includes RIFE for LTE in TV White Space (TVWS), indoor WLAN and outdoor GSM as well as in-band femto-cell configuration and optimization.

In subsequent work within this WP, these techniques will be cross-evaluated and contrasted in real-field tests and measurements. Finally, Chapter 4 offers the conclusions for this deliverable.

⁵ Note the distinction in terminology here: in MUD, the term “detection” refers to separating the bit-streams of overlapping sources that are known *a priori* to be there. This is different from the notion of source-presence detection, as discussed here.

⁶ Different bands can be handled via TOA/TDOA, of course, it is the same identical frequency that presents this problem.

2 Source characterization: detection, parameter estimation and localization

2.1 Introduction

Characterizing an information source can prove very useful in order to enrich Radio Environmental Awareness (REA) in a wireless communication system. Furthermore, it can be used as an intermediate step for the estimation of the power spectral density in space and time, what has been previously already defined as RIFE. Source characterization mainly refers to identifying the presence, number, location and power spectral density of transmitting sources; all these questions are indeed treated in this chapter. There could potentially be further source characteristics one could investigate, eg. signal bandwidth etc.

The localization of an emitter based on partial or full knowledge of the transmit (*Tx*) signal is a widely investigated field in the literature as well as in practice. For this purpose, various ranging techniques are engaged for spatially localizing the radio sources (emitters). These techniques provide sensor-local estimates in terms of distance or orientation related to the neighbors of a cognitive radio device. This sensor-local information (estimation) is then usually gathered from multiple CRs and further combined appropriately in order to provide the location estimates. The most usual types of information used for ranging techniques are the following:

Time of Arrival: This is the Time of Arrival (TOA) of a known or unknown (i.e., blindly processed) Rx signal. Known signals are usually named “pilot signals”, which are pre-designed for a specific communication system. The Time Difference of Arrival (TDOA) can be treated as a special case of TOA when the sensors are not clock-synchronized with the transmitter (as is true in most cases in cognitive radio scenarios).

Angle of Arrival: This is the Angle of Arrival (AOA) of a known or unknown (blindly processed) Rx signal. The same assumptions hold as in TOA estimation.

Power, or Received Signal Strength (RSS): This is the total power that is received from a known or unknown signal. The measurement bandwidth can be narrowband (in order to sense a small number of transmitters) or wideband (for sensing a potentially large number of transmitters). The time horizon of the measurements is also a very critical parameter.

After estimating the position-related signal parameters such as RSS, TOA, TDOA and AOA, source position estimation can be performed based on various techniques. In addition to the position of the sources, another crucial parameter for the scenarios of interest in FARAMIR is the transmit (*Tx*) power level. All this information, together with a radio propagation model can be used to characterize the interference field of an area of interest.

In Section 2.2 a noise-robust test to detect the presence of a source is proposed that can be used along with ranging parameter estimators for purposes of detection and approximate localization. A simple conceptual framework is proposed that naturally generates techniques with immunity to

parameter uncertainties for detecting the presence of an unknown source in broadband noise. At the cost of longer observation time, they allow SNR-wall-free detection. They also lend themselves to precise analysis and parametric optimization. In Section 2.3 the known problem of estimating the AOA of an emitting source is addressed via passive radio means, namely an antenna array. The challenges in the considered scenarios are (a) time-varying, terrestrial multipath propagation with medium-to-low SNR and (b) very short capture records (single-packet processing). A two-stage estimation procedure is presented: first an overall channel estimation stage followed by a AOA extraction method suitable to both blind (no training data employed) as well as training-assisted cases. In Section 2.4 we review some basic fusion techniques for localization. The problem of estimating the average transmitted power, number and location of a multitude of sources in a wireless environment is addressed in Section 2.5. In particular, based on power measurements of sensors placed in known locations in space, a technique is developed which employs the ML criterion in order to derive the aforementioned parameters of the transmitting sources in a shadow-fading environment. In this work, the ML estimator is described theoretically and simulation results are presented that corroborate the theoretical claims in scenario specific example.

2.2 Noise-Robust source detection based on ranging-parameter estimation

2.2.1 State of the Art on source detection and proposed approach

Source sensing, meant as classic binary hypothesis testing (presence detection) of a source in a given spectral band, an important function in cognitive radio and other applications, must typically be performed in the absence of detailed knowledge of at least some aspect of the system and signal model. This lack of knowledge may range from simply not knowing some of the channel characteristics, such as the channel complex gain in a flat-fading channel (but knowing precisely either the signal shape or some parts of the signal, e.g., its pilots or preambles), all the way to knowing nothing about the sought signal or the intervening channel. The latter case is the easiest to handle, meaning that then one can only resort to non-coherent, moment-based processing (energy detection, autocorrelation, spectral correlation/cyclo-stationary processing, etc.). This latter class of techniques is popular with the sensing community because it demands the least from the algorithm designer, although it is still subject to optimization of its various parameters (for instance, which correlation or cyclic-frequency terms to incorporate in the detection statistic and with what weight). Still, it has the appeal of simplicity, invoking the least set of assumptions, and it may work well for high enough SNR. In addition, energy (quadratic) detection is indeed mathematically optimal under very specific modeling assumptions (Gaussian signal in Gaussian noise). If the signal is not patently Gaussian but unknown in its features, it still makes sense as an "agnostic" solution [4]. The difficulty with energy detection is that it is brittle when the noise level is not precisely known, because then the false-alarm-based threshold cannot be set with accuracy. This leads to the known "SNR wall" phenomenon [5], [6]. Ways to somewhat bypass this sensitivity to the relative ignorance of the noise level have been explored in depth and tend to center on autocorrelation or spectral-correlation techniques that omit the zero-lag term,

which includes the mean value of the noise level (although there is still dependence on the noise level to set the threshold, just less) [7].

On the other extreme, the signal may be known in shape, including the values of its data symbols for some duration (for instance, pilot symbols). This can be exploited in a matched-filter or signal-correlation operation, akin to what is done in coherent receivers for digital communication operation. The result will be a coherent accumulation of voltage during this correlation interval and a concomitant increase in collected energy versus the purely sample-by-sample non-coherent processing of the energy detector (which suffers the so-called "non-coherent combining loss"). Therefore, matched filtering which exploits such knowledge will result in an SNR shift for performance (an SNR benefit). We note, however, a fundamental difference between coherent filtering in coherent comm. receivers and pseudo-coherent processing in sensing receivers: the latter cannot exploit the exact channel knowledge (gain and phase) enjoyed by a coherent comm. receiver due to the carrier synchronization/equalization pre-processing that the comm. receiver enjoys. As a result, there will be a non-coherent (complex-norm) operation at the end of the sensing receiver processing, and therefore, in that sense, *all sensing receivers are non-coherent in nature*; there is no such thing as a fully coherent sensing receiver. The only difference between classic non-coherent processing and matched-filter processing is whether the squaring operation takes place sample by sample or at the end of the observation interval.

Here, a new framework for Constant-False-Alarm-Rate (CFAR) [8] feature-based detection is proposed. We focus on (but are conceptually not limited to) spatial signal features that arise due to the reception of the signal at different points in space. These features allow detection (*first*, and that is the novelty) as well as subsequent localization of unknown sources based on an estimation pre-processor. The proposed family of statistical tests is based on the appropriate processing of the received samples in order to create successive and statistically independent estimates of signal features that have meaning if and only if a signal is present. By first quantizing the feature range and subsequently estimating the most probable value for the feature under consideration, a histogram is created which signifies the relative probabilities for the different (discrete) sub-regions on the value of the feature. Based on an analytical description of this histogram, a test is created on the existence or not of the signal, as well as the value of the feature (as an immediate fringe benefit). The whole procedure takes therefore two steps: the first where successive estimates of a feature are made *as if the signal exists* and a second where these estimates are employed in order to decide on the binary hypothesis of the signal existence, as well as the feature value.

A large number of tests that assume accurate knowledge of the noise level have been proposed [4], [9]. These tests are expected to have better performance than the one proposed but suffer from SNR walls. Tests that are CFAR without the knowledge of the noise level have also been proposed, [7],[10], that use a self-normalizing approach but are difficult to analyze and thus optimize. Here, by locating the position (in feature space) of the maximum of the histogram as the appropriate statistic for the final binary test, a decision is made on the existence of a signal, as well as on the value of the feature should the decision be positive; otherwise, this value is meaningless.

It is also shown here that the analysis of the performance of this scheme is straightforward, thus allowing for subsequent optimization of the test.

This section is organized as follows: In Sub-Section 2.2.2 the histogram test is described, which a fundamental part of the proposed approach. Besides the description, an approximate analysis is provided along with simulation results for assessing its accuracy. Two application examples in Sub-Section 2.2.3 demonstrate the breadth of the concept, one for cyclic-prefix-based (CP) detection plus one for time difference of arrival (TDOA) -based detection and localization. The details for proper data processing, together with an analytic performance description are provided. Simulation results are given in Sub-Section 2.2.3.3.

2.2.2 Description of the proposed test

In this section we describe a simple, non-linear test that will be used as the cornerstone for the proposed approach. Within this framework, different localization as well as feature estimation techniques already available in the literature can be employed. A test description is provided at a fairly abstract level, with specific instantiations described in the following sections for clarity.

2.2.2.1 Analysis

We address the following binary hypothesis problem: under \mathbf{H}_0 (no signal present) we observe the outcome of a purely random choice between N_L events, denoted by h_i ($i=1,\dots,N_L$). Under \mathbf{H}_1 (signal present) one specific event, denoted by h_c , has a larger probability of occurrence than the rest. This is the simplest scenario that we analyse here; extensions to multiple events of higher probability are under investigation. Let y_k be the k -th observation. Then, for \mathbf{H}_0 ,

$$p(y_k = h_i) = \frac{1}{N_L} \quad (2.1)$$

whereas for \mathbf{H}_1 ,

$$p(y_k = h_c) = p, \quad p(y_k = h_i) = \frac{1-p}{N_L-1} < p \text{ for } i \neq c \quad (2.2)$$

Here $p(y_k = h_i)$ is the probability of observing the event h_i . After N_b observations we wish to decide on the prevailing hypothesis for a given target probability of false alarm P_{fa} . At the same time, an estimate of the event with the highest probability of occurrence (under \mathbf{H}_1) is produced.

The following test is proposed for the just-described joint detection /estimation problem: Define

$$T = \max(\text{hist}(\mathbf{y})) \leq \lambda \quad (2.3)$$

the test for the detection task, and $\hat{c} = \text{index}(T)$ for the estimation, where $\mathbf{y} = [y_1, y_2, \dots, y_{N_b}]$ is the total vector of observations, $\text{hist}(\cdot)$ is the histogram operator, namely a counter for the number of

occurrences for each of the N_L events, $\max(\cdot)$ is an operator that provides the value of the largest number of the input vector and $\text{index}(\cdot)$ is its index. Other tests could also be devised with possibly better performance, but the currently proposed test is simple and performs almost optimally in the parameter regions of interest.

For \mathbf{H}_0 , $\text{hist}(\mathbf{y})$ is a length- N_L vector of random variables (rv), $\hat{h}_i \in [0, 1, \dots, N_b]$, each following a binomial distribution with probability density function (pdf)

$$p(\hat{h}_i = x) = \binom{N_b}{x} p(h_i)^x (1 - p(h_i))^{N_b - x}, \quad (2.4)$$

with $x = 0, 1, \dots, N_b$ and its cumulative distribution function (cdf)

$$F_i(x) = P(\hat{h}_i \leq x) = \sum_{r=0}^x \binom{N_b}{r} p(h_i)^r (1 - p(h_i))^{N_b - r}, \quad (2.5)$$

To analyze the performance of the proposed test, the cdf of the maximum of these N_L rv's is required. A simple approximation can be provided by ignoring their correlation. The cdf of the maximum is given by

$$F_{N_L:N_L}(x) = F_i(x)^{N_L} \quad (2.6)$$

Using this approximation, the P_f for a threshold value λ is

$$P_f(\lambda) = 1 - F(\lambda)^{N_L} \quad (2.7)$$

Using the same rationale for the \mathbf{H}_1 case, the probability of detection (P_d) is approximated by

$$P_d(\lambda) = 1 - F_c(\lambda) F_i(\lambda)^{N_L - 1} \quad (2.8)$$

2.2.2.2 Accuracy of approximations

We now examine the accuracy of the above approximations for this type of test, since it is the most critical part for guaranteeing the level of false alarm while optimizing the probability of detection. The discrete distributions that describe both hypotheses are generated by N_L uniform and continuous rv's, where the maximum is chosen at each sample test. In order to produce the required statistics for the \mathbf{H}_1 case, $(N_L - 1)$ rv's are generated with support in $[0, 1]$ plus one in $[0 + s, 1 + s]$, where s is chosen so that the probability of indeed being the maximum in the set equals p . This is done by solving numerically the following equation for p : $p = (1 - s^{N_L}) / N_L + s$.

By producing the N_L rv's for each hypothesis and choosing the index i of the maximum, we can produce the h_i 's that fit the above scenario for any arbitrary values of p , N_L , N_b .

We now demonstrate the approximation of the analysis and the performance of the test for some indicative values of the aforementioned parameters. In Figure 1 we demonstrate the accuracy of (2.7) for $N_L = 100$ and $N_b = 10, 100, 1000$. In Figure 2, we demonstrate the accuracy of (2.8) for $N_L = 10$, $N_b = 100$ and $p_c = 0.2, 0.4$ and 0.6 . We conclude that the proposed analysis follows the simulation results with very high accuracy for the discussed cases; all other simulations performed extensively have the same behaviour (not shown here). All basic tools are now in place to achieve a target ROC, with the classic definition of $\text{ROC} = (P_f, P_d)$. We now proceed to show specific instantiations of the theory for detection (only) as well as joint detection/localization in examples of common interest.

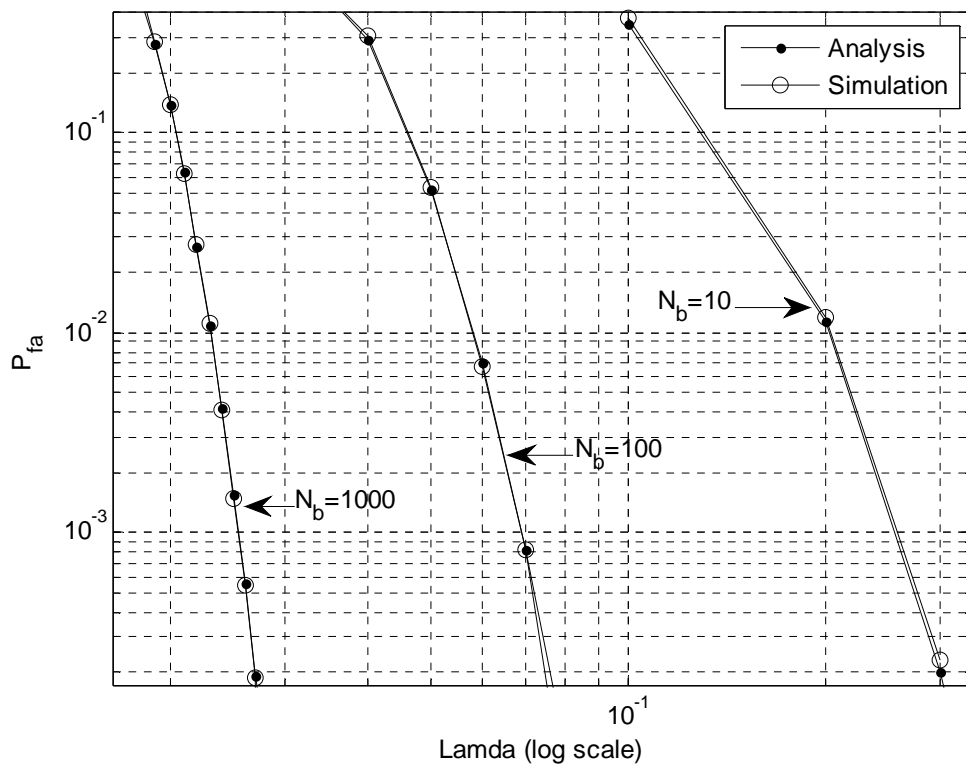


Figure 1: Probability of false alarm vs. lambda.

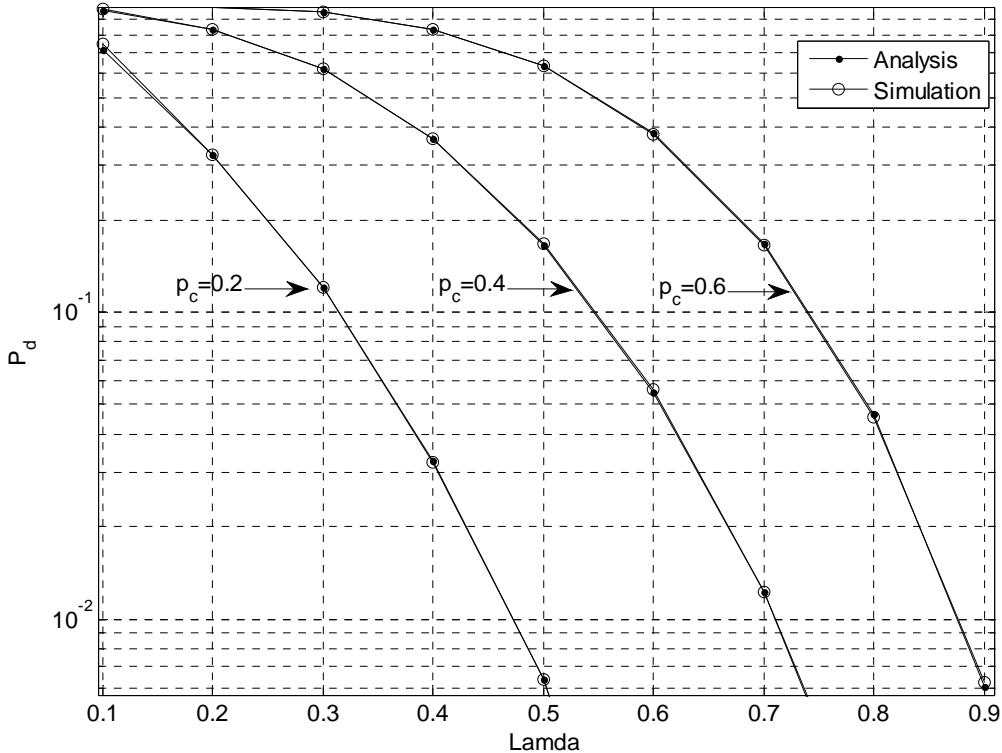


Figure 2: Probability of detection vs. lambda.

2.2.3 Performance assessment

To assess the performance of the proposed framework, we employ two examples. The first example involves the detection of an OFDM source based on its cyclic prefix (CP). The second involves the joint detection/localization of a source based on TDOA estimation. Both examples can be treated in a unified manner under the proposed framework. The only difference (besides parameterization constraints) is what feature is chosen to represent the test. In the first example it is the symbol synchronization time, while in the second it is the TDOA between two different points in space. Both exhibit a periodicity: due to the symbol rate in the first case and due to the spatial coherence bandwidth of a source in the second.

2.2.3.1 Cyclic prefix based OFDM detection

Let N_{cp} be the cyclic prefix length, N_{FFT} the FFT length, and $N_{S-total}$ the total number of OFDM symbols received. We assume the signal bandwidth and the above parameters known. The proposed processing is depicted in Figure 3. Since the starting time of a symbol is unknown, the ambiguity range is $N_{cp} + N_{sym}$, equal to the previously defined N_L . For each of the N_L possible events, the following two vectors are defined: $\mathbf{r}_{1,i} = [y(i + k(N_{cp} + N_{sym})), \dots]$ and $\mathbf{r}_{2,i} = \mathbf{r}_{1,i+N_{cp}}$, with

$k \in (0,..N_{s-total})$; $i \in (1,..N_{cp} + N_{sym})$. Classic estimation of the symbol starting time involves the inner product of $\mathbf{r}_{1,i}$ with $\mathbf{r}_{2,i}$ for all possible candidate values of i . In low SNR, it has been shown [12] that it suffices to use the real part of the inner product, i.e.

$$\hat{t} = \arg(\max(\text{real}(\mathbf{r}_{1,i}^H \mathbf{r}_{2,i}))) \quad (2.9)$$

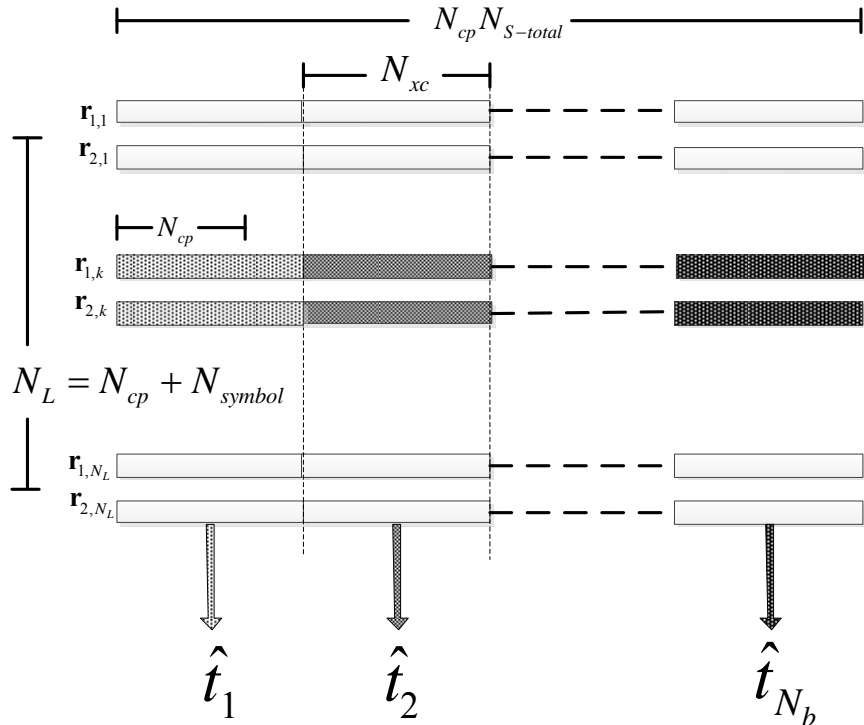


Figure 3: Proposed processing for CP-based detection example.

As shown in Figure 3, N_{xc} is the number of samples employed here for each estimate ($1 \leq N_{xc} \leq N_s$). The constraint imposed by the finite number of samples is described by the following inequality $N_b N_{xc} \leq N_s$. We can now compute, for any set of desirable parameters, the threshold that guarantees the desired P_{fa} . In addition, knowledge of the SNR level, with any level of accuracy, enables parameter optimization for a target ROC.

2.2.3.2 TDOA based source detection/localization

Here the proposed framework is adopted as a test for detecting a source via TDOA estimation. The envisioned scenario assumes multiple pairs of sensors doing an identical test, and then properly combining the individual TDOA estimates for a final statistic. The focus here is on the intermediate step of individual TDOA estimations, not the final geometric transformation of these multiple estimates to localization.

Let r_1, r_2 be the two received sequences by two spatially distinct sensors, both of which either observe noise only or signal plus noise. The signal, if present, is modeled as a white process

(extension to colored signals is straightforward). Then, employing classic cross-correlation-based estimation as shown in (2.9), the lag corresponding to the maximum value is the candidate TDOA estimate.

This is conceptually equivalent to an autocorrelation- feature detection test, since it is still the same (noiseless) signal that is received at both sensors under H_1 . Instead of trying to solve for the optimal detector under some (partial) knowledge of the noise statistics, the proposed framework is again engaged, leading to a true CFAR test because the P_{fa} is fully independent of the noise level.

Figure 4 demonstrates how statistically independent TDOA estimates can be generated. Clearly, at least two estimates are needed for non-trivial tests. Let N_L be the range of values of TDOA, N_s be the total number of samples, N_b be the number of TDOA estimates, and N_{xc} be the number of samples used for producing each estimate. These parameters are constrained by the inequality $N_b N_{xc} + N_L \leq N_s$.

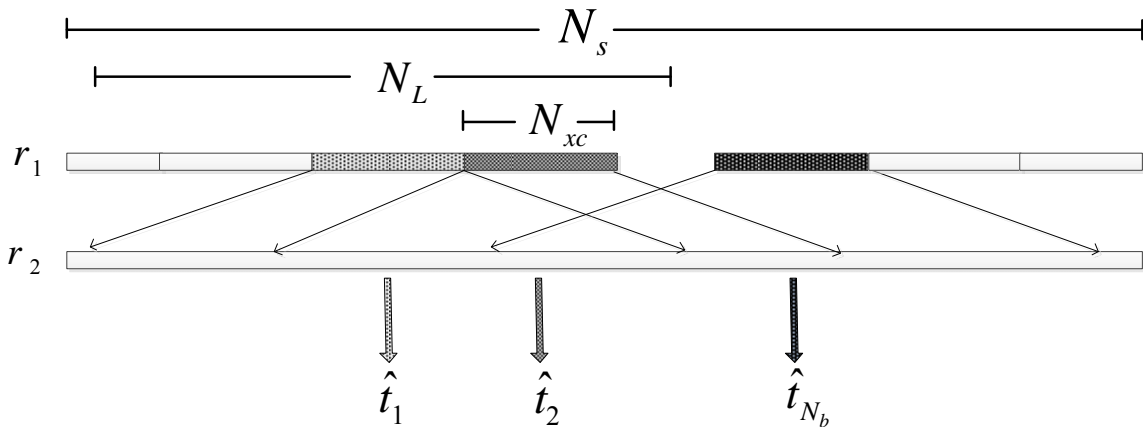


Figure 4: Proposed processing for TDOA-based detection example.

The previous description of the histogram-based test indicates that the probability of successful detection P_d can be maximized for a given P_{fa} level, under parametric choices that are subject to some constraints. From an estimation-only point of view, TDOA accuracy increases with N_{xc} . But since at least two estimation samples are needed for a non-trivial test, a certain degradation of TDOA estimation accuracy is expected. It will soon be evident that a trade-off exists between the two tasks of detection (signal detectability) and final estimation (localization accuracy). We note, however, that such a trade-off is eventually artificial and rather created by system-level constraints such as processing complexity, data-exchange bandwidth, etc. It is not a fundamental law, in other words, since estimation/localization can be re-performed after successful detection by optimally employing the whole data set. In that sense, parameter estimation is understood here chiefly as a detection pre-processor, leading to the concept of *estimation-based detection*.

2.2.3.3 Performance analysis

To analyze performance, the description of the test statistics should be derived. The distribution of the sum of products of normal r.v's resulting from the cross-correlation operation has been described in [12], where a Gaussian approximation is used based on the central-limit theorem. In [12], a CP-based detector is described, leading to an analysis that is applicable to the present one. As mentioned before, at low SNR, only the real part of the cross-correlation need to be employed with very small degradation in performance. The relevant test statistics can be approximated as $N(0, \sigma^2), \forall i$ for the \mathbf{H}_0 case, while for the \mathbf{H}_1 , $N(\mu, \sigma^2)$ for $i=c$ and $N(0, \sigma^2)$ for $i \neq c$, where $\sigma^2 \approx \sigma_n^2 / 2N_L$, $\mu = \sigma_s^2$, with σ_n^2 the variance of the complex additive Gaussian noise and σ_s^2 the variance (power) of the Gaussian-modeled signal. For \mathbf{H}_0 , since all h_i 's possess the same distribution, the probability that any one of them corresponds to the maximum has been derived in a previous section. Thus, P_{fa} is described by (2.7). For \mathbf{H}_1 , the probability of choosing the right lag, $p(h_c)$, must be derived in order to be able to compute and optimize P_d . This probability is, in fact, the familiar probability of correct decision of M-ary orthogonal signals in additive Gaussian noise, given by

$$p_c(\mu, \sigma^2, N_L) = \frac{1}{2\pi\sigma^2} \int_{-\infty}^{\infty} \left(\int_{-\infty}^a e^{-\frac{z^2}{2\sigma^2}} dz \right)^{N_L} e^{-\frac{1}{2\sigma^2}(a-\mu)^2} da \quad (2.10)$$

Many approximations are known for computing the above integral [13]. Unfortunately, they all target bit error probabilities which must be very small to be useful, thus not suited for the present detection problem. Numerical algorithms for approximating (2.10) for the parameter ranges of interest have been employed for the performance assessment.

2.2.3.4 Simulation results for cyclic prefix based detection

Typical OFDM values from the DVB standard are employed, such as $N_{cp} = 1024$, $N_{FFT} = 8192$ or from the LTE standard, such as $N_{cp} = 36$, $N_{FFT} = 512$. Figure 5 plots the required sample size as a function of SNR for achieving a given ROC. The purpose here is to compare the new test performance versus the radiometer when the latter operates either under ideal conditions (perfectly known noise level) or non-ideal ones (uncertainty in the noise level), thus demonstrating the immunity of the proposed class of tests to noise uncertainty. We conclude that the new tests are comparatively inefficient under ideal conditions (an SNR loss versus the ideal radiometer under no noise-level uncertainty). But when a u-parameterized uncertainty on the noise level exists, the radiometric detectors are 'tuned' to the worst-case noise level for guaranteeing the P_{fa} level (see [6] for details). Then, the proposed scheme becomes superior and exhibits no wall; the only effect is an SNR loss, proportional to u (in dB). The worst case plotted is for $u=1$ dB, causing a radiometric SNR wall at about -3 dB, while the proposed test improves continuously with SNR.

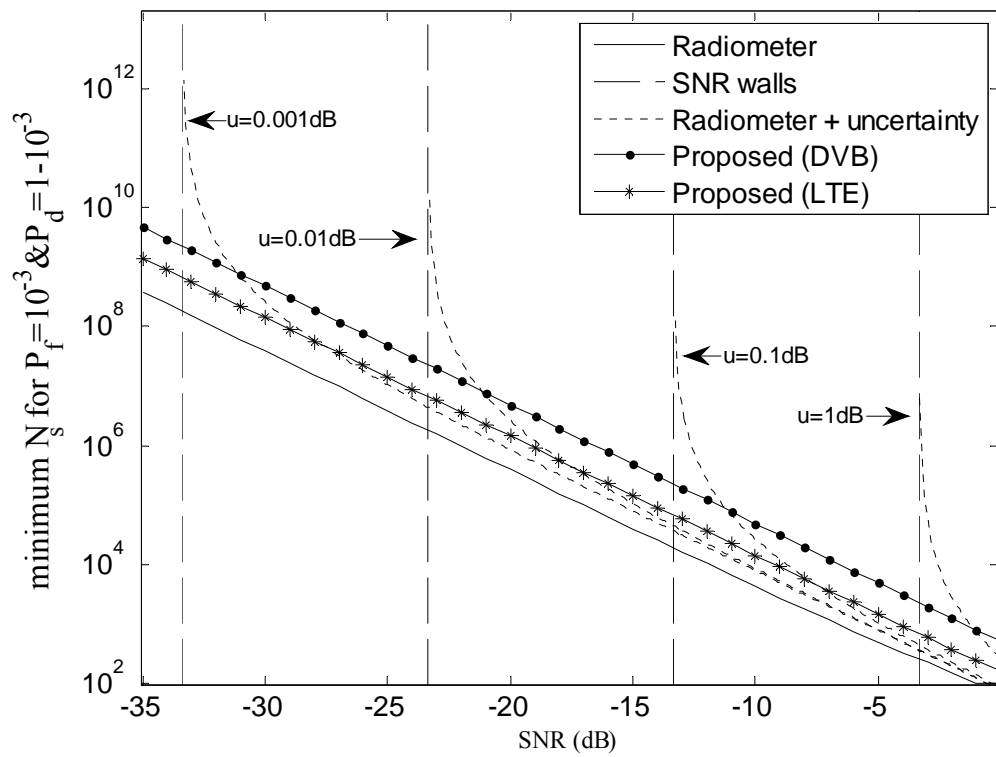


Figure 5: Sample size versus SNR.

Since non-radiometric detectors in general are affected by limited processing time due to channel coherence, Figure 6 demonstrates the performance degradation of the proposed scheme based on a maximum allowable interval for coherent processing. It can be seen that a maximum value for N_{xc} results in a slope change at a certain SNR point. Performance degrades, but still no SNR wall appears.

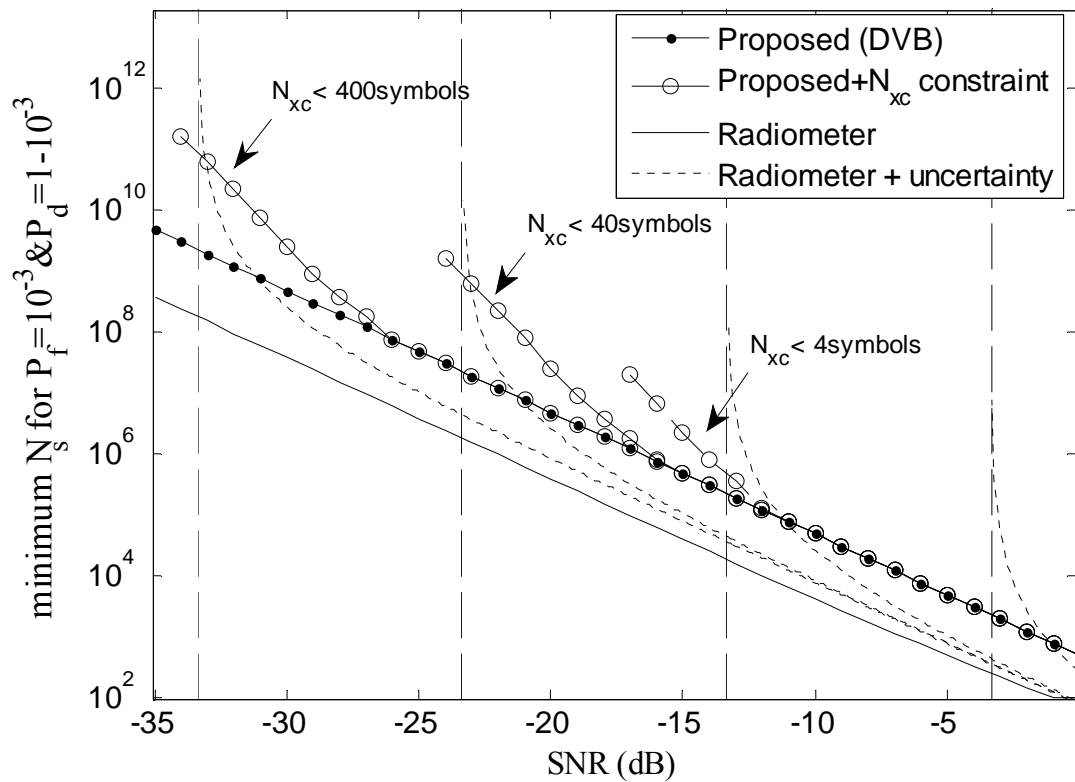


Figure 6: Sample size versus SNR.

2.2.3.5 Simulation results for TDOA based detection/estimation

Since the two problems (CP and TDOA) are analytically similar, all results presented in the previous section can be mapped to an equivalent TDOA problem. In order to re-interpret the performance results of the previous section in a TDOA example, we equate the uncertainty region to one OFDM symbol. Thus, an SNR gain of $(N_{cp} + N_{FFT}) / N_{FFT}$ is to be expected.

The following simulation results measure the required number of samples under different conditions. In Figure 7 we set FA at 0.1%, the PD at 99% and plot the required number of estimates as the uncertainty region increases; this is done for four fixed N_{xc} values. In Figure 8, we plot the optimum number of required samples versus the uncertainty region for maximizing detection (most of the time $> 99\%$), when we constrain the number of available samples. The presented curves have been smoothed out in order to remove the scaling effects due to the use of a discrete binomial distribution.

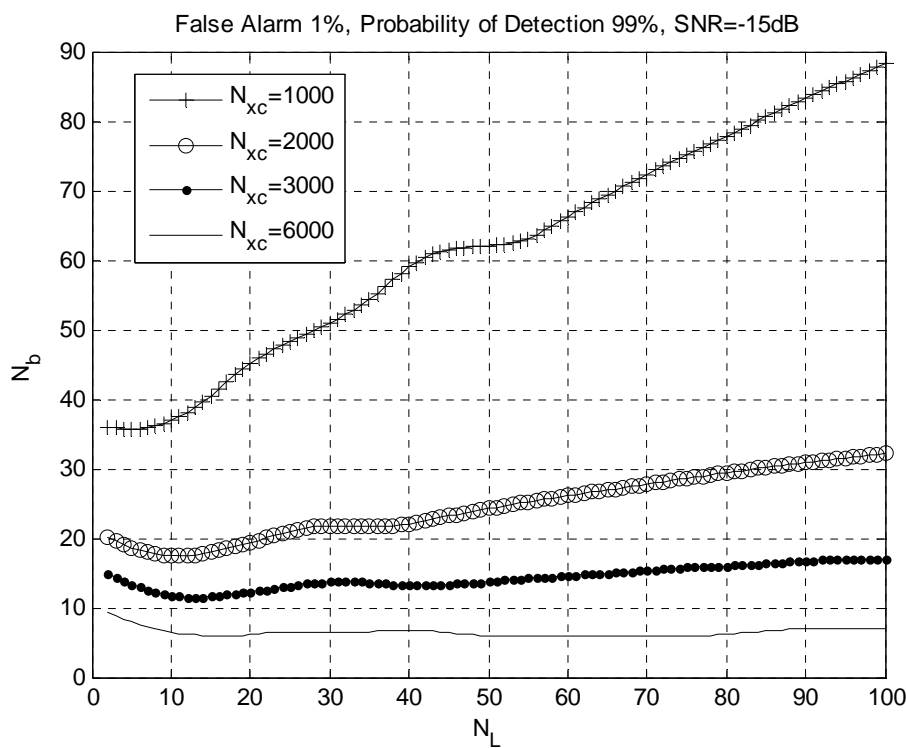


Figure 7: Needed number of estimates vs. the uncertainty region.

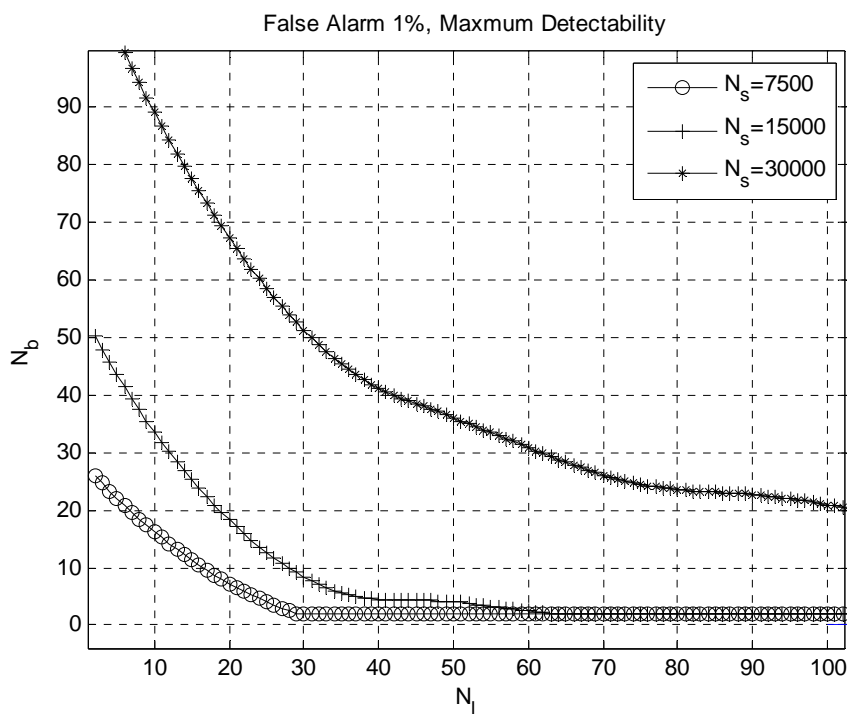


Figure 8: Optimum number of estimates vs. the uncertainty region for fixed number of total samples.

2.3 Angle-of-Arrival estimation in dense multi-path environments

2.3.1 State of the Art on AoA estimation and proposed approach

AOA-based techniques have the potential to provide localization with very high accuracy, much higher than competing techniques. This is because the direction of arrival of an RF wavefront may be performed with great accuracy, a few degrees, and that leads to very a very fine estimate of directionality. This, however, obviously depends on the achievable accuracy that is allowed both by the surrounding environment (i.e., the degree of angle spread) as well as on the resolution of the employed signal-processing methodology. In any case, the notion of AOA exists, and we may even speak of the "Line of Bearing (LOB) to indicate the conceptual line connecting the transmitter with the receiver. If the transmitter is physically visible, we talk of the Line Of Sight (LOS) as a special case of the LOB; if it is not visible, the LOB still exists as a geometrical concept, regardless of the specifics of the signal under consideration. On the other hand, in many such systems, "TOA" does not have a well-defined meaning since no explicit timing reference may available; in other words, there may not be away to acquire or estimate the absolute time of the transmission. Even then, however,, the ability to estimate the Path Temporal Separation (PTS), defined as the TDOA *between the propagation paths of the same source message*, is very important because it can facilitate the estimation of the AOA of the various propagation paths. This is particularly true whenever their number is larger than the number of array elements.

The AOA literature is indeed vast; quite numerous AOA estimation schemes have been developed and analyzed over the past three decades [15]. Traditional approaches tend to be *non-signal-specific*, meaning that they extract AOA information directly from the raw array vector observations without exploiting specific details about the signal structure. These approaches, in other words, do not model parametrically the waveform structure of the transmitted modulation format; rather, they just assume generic signal samples without any further detail incorporated in the model. The number of impinging propagation paths that can be spatially separated using such approaches is limited by both the number of array elements and the temporal correlation of the paths. The most familiar of those are the subspace-based algorithms in MUSIC [17] which perform eigen-decomposition of the spatial correlation matrix in order to arrive at signal and noise subspaces [15]. We will call these *subspace-based methods* because they employ either of the two subspaces (signal sub-space or noise sub-space) to estimate the AOA. Therefore, their performance depends on the accuracy of separating these two subspaces, which in turn requires a large number of statistically independent received samples. These algorithms fail to provide meaningful AOA estimates when the number of temporal observations is small and/or when they operate in a coherent multipath environment. Techniques like spatial smoothing [18] can remedy the latter problem at the expense of a resolution reduction. Several studies (e.g., [19]) have demonstrated that within this class of non-signal-specific approaches, ML-based algorithms provide performance superior to that of subspace-based algorithms, especially when the number of available temporal observations and/or the SNR are fairly low. ML-based algorithms are capable of operating in a variety of challenging propagation environments, including those with significant multipath without the need for pre-processing the received signal. In order to overcome the limitations that

the traditional approaches impose on the number of received propagation paths that can be spatially separated, a two-stage, *signal-specific* approach was developed in [20]. The first stage of this approach estimated the Overall Channel Impulse Response (OCHIR), which includes the overall effects of the propagation channel plus those of the transmit and receive filter. In the second stage, the OCHIR estimates were converted to TOA/AOA estimates using two-dimensional versions of traditional array processing algorithms. We note, however, that either subspace or ML-based algorithms could be used in this second stage. The advantages of this broad, signal-specific approach are: (a) it can be used to spatially separate propagation paths whose number may exceed the number of array elements (provided that there is enough temporal separation between the paths), and (b) it allows for the joint TDOA and AOA estimation of each propagation path, assuming an arbitrary time for the first path. In [10], OCHIR estimates are obtained using multiple *known* data blocks (i.e., training sequences) plus the Batch Least-Squares (LS) algorithm. Due to the high computational complexity of the ML-based conversion algorithms, the authors in [20] emphasized the use of subspace-based algorithms for the OCHIR conversion task. The particular implementation presented in [20] has limited applicability because (a) it relies on the existence of multiple training data blocks, which may not be available in any FARAMIR scenario of interest, and (b) it assumes that the physical propagation channel de-correlates quickly and is thus statistically independent between data blocks, clearly not the case in static or quasi-static propagation environments. This latter de-correlation assumption, however, is crucial for the construction of a consistent estimate of the spatio-temporal correlation matrix that the subspace-based conversion algorithms require. Thus, in the absence of such de-correlation, other methods should be sought.

In this Section we therefore focus on the extension of the aforementioned two-stage approach to environments where training data may not be available and the collection records may be very small (thus not enabling correlation-matrix construction). A reduced-complexity, LS-based conversion algorithm is introduced for the second stage which first estimates the PTS and then uses these PTS and OCHIR estimates to estimate the path-AOAs. The present conversion algorithm is applicable to both static as well as non-static (time-varying) propagation environments and can provide reliable estimation performance *even when a single observation data block is available*. The performance results included here show that the AOA estimation performance of this procedure is close to the Cramer-Rao Lower Bound (CRLB) in a variety of challenging propagation scenarios.

2.3.2 Description of the proposed estimator

The following sub-sections describe the overall considered model in detail:

2.3.2.1 Signal Model

Let $s(t)$ denote the transmitted signal waveform:

$$s(t) = \sum_k d_k h_t(t - kT) \quad (2.11)$$

where $\{d_k\}$ denotes the sequence of (memorylessly)-modulated symbols, T denotes the symbol duration, and $h_t(t)$ is the pulse-shaping filter. For the multipath model, the waveform for the p^{th} ($p=1,\dots,P$) propagation path can be expressed as follows:

$$r_p(t) = c_p(t) \cdot s(t - \tau_p) \quad (2.12)$$

where $c_p(t)$ and τ_p denote the p^{th} propagation path's time-varying complex gain and TOA, respectively. The time-varying complex gain is modeled as

$$c_p(t) = c_p \exp\{j2\pi f_{D,p} t\} \quad (2.13)$$

where $f_{D,p}$ denotes the p^{th} propagation path's frequency of arrival (FOA) and c_p is the corresponding time-invariant complex gain, which is considered to be constant during one observation data block, but varying independently between different data blocks.

For an one-dimensional antenna array, the received waveform at the m^{th} ($m=1,\dots,M$) array element is given by

$$x_m(t) = \sum_{p=1}^P a_m(\phi_{a,p}) \cdot r_p(t) + w_m(t) \quad (2.14)$$

where $a_m(\phi_{a,p})$ is the array response to the p^{th} propagation path's azimuth AOAs ($\phi_{a,p}$) and $w_m(t)$ represents the zero-mean AWGN.

The receive filter, $h_r(t)$, is modeled as a generic anti-aliasing brick-wall filter, followed by a sampler of sampling frequency $f_s = 1/T_s = N_s \cdot 2B = N_s / T$. Here, B is the transmitted signal bandwidth and N_s is the *integer* over-sampling ratio. The output of the receive filter is then given by

$$\begin{aligned} z_m(t) &= x_m(t) * h_r(t) \\ &= \sum_{p=1}^P a_m(\phi_{a,p}) c_p \left(\exp\{j2\pi f_{D,p} t\} s(t - \tau_p) * h_r(t) \right) + (w_m(t) * h_r(t)) \\ &= \sum_{p=1}^P a_m(\phi_{a,p}) c_p \exp\{j2\pi f_{D,p} t\} \tilde{s}(t - \tau_p) + \tilde{w}_m(t) \end{aligned} \quad (2.15)$$

thus the output of the sampler at time kT_s can be modeled as follows:

$$z_m[k] = \sum_{p=1}^P a_m(\phi_{a,p}) c_p \exp\{j2\pi f_{D,p}(kT_s)\} \tilde{s}(kT_s - \tau_p) + \tilde{w}_m[k] \quad (2.16)$$

where the filtered-noise samples, $\tilde{w}_m[k]$, are zero-mean, temporally and spatially uncorrelated, Gaussian random variables.

For the signal model presented above, it can be shown that the samples of the complex envelope of the observed waveform at the m^{th} ($m=1,\dots,M$) array element can be also modeled as follows:

$$z_m[i,j] = \mathbf{d}^T[i,j] \cdot \mathbf{h}_m[i,j] + \tilde{w}_m[i,j], \quad 0 \leq i \leq N-1, \quad 0 \leq j \leq N_s - 1 \quad (2.17)$$

Here, N is the observation length (in number of symbols) and N_s is the number of samples per symbol (assumed integer). The convolution of the transmit filter with the impulse response of the physical propagation channel and the receive filter is represented by the $(L_c+1) \times 1$ vector of OCHIR coefficients $\mathbf{h}_m[i,j]$, where L_c is the memory of the OCHIR (in number of symbols). The vector $\mathbf{d}[i,j]$ consists of L_c+1 data symbols, assumed independent and uniformly distributed over a finite alphabet A (in the examples below, A is taken as the binary alphabet). The noise samples $\tilde{w}_m[i,j]$ are zero-mean, temporally and spatially uncorrelated, Gaussian random variables.

Since the receive filter is anti-aliasing brick-wall, meaning no distortion of the received signal, the OCHIR coefficients are just the convolution of the transmit filter with the impulse response of the physical propagation channel. Although the impulse response span of the channel is usually short, the temporal span of the transmit filter can occasionally be very long (think of Nyquist pulses). Yet, in a tap-delay line model of the transmit filter, usually only a few T -spaced taps carry significant power. We thus arrive at the following model for the samples of the observed waveform's complex envelope:

$$z_m[i,j] = \check{\mathbf{d}}^T[i,j] \cdot \check{\mathbf{h}}_m[i,j] + \check{w}_m[i,j], \quad 0 \leq i \leq N-1, \quad 0 \leq j \leq N_s - 1 \quad (2.18)$$

where the vectors $\check{\mathbf{d}}^T[i,j]$ and $\check{\mathbf{h}}_m[i,j]$ have length $L_s < L_c + 1$. Note that the samples $\check{w}_m[i,j]$ of the "noise" in this model, are no longer uncorrelated (temporally or spatially), Gaussian random variables.

2.3.2.2 OCHIR estimation techniques

How to estimate the OCHIR coefficients depends on the nature of the modulated data waveform and the particular data transmission system. When training sequences are available, the OCHIR coefficients are estimated via these sequences and the Batch LS algorithm, as discussed in [20]. If they are not available, *blind* joint data and OCHIR estimation should be performed. One such tool is the Per-Survivor Processing (PSP) class of algorithms [21]. A PSP-LMS algorithm applicable here proceeds by defining the state-transition metrics (where μ_i is the state) as

$$\Gamma(\mu_{i-1}, \mu_i) = \sum_{m=0}^{M-1} \sum_{j=0}^{N_s-1} \left| z_m[i,j] - \tilde{\mathbf{d}}_i^T \cdot \hat{\mathbf{h}}_m[i,j] \right|^2 \quad (2.19)$$

The OCHIR estimate update is then given by:

$$\hat{\mathbf{h}}_m[i,j] = \hat{\mathbf{h}}_m[i-1,j] + \delta \cdot \left(z_m[i,j] - \tilde{\mathbf{d}}_i^T \cdot \hat{\mathbf{h}}_m[i-1,j] \right) \cdot \tilde{\mathbf{d}}_i^* \quad (2.20)$$

where δ is the LMS step size.

All OCHIR estimation algorithms of this type require knowledge of the transmitted modulation format in order to define the state diagram in the PSP trellis. If such knowledge is not available, one can resort to modulation classification techniques in multipath-fading channels (see [23]) as a pre-processor to the AOA estimator.

Here we present briefly the steps of a blind OCHIR/FOA estimation algorithm, functional for a large range of FOA values (from very small to very large). This works when all propagation paths have the same FOA. Such a situation arises when all paths arrive from a large distance and are fairly close spatially.

We first divide the FOA range into N small intervals (bins). Within each bin the FOA is estimated and refined recursively via a repeated application of a blind PSP OCHIR estimation algorithm. The FOA processing *per each bin* can be summarized as follows:

1. An initial FOA value is assigned and the received samples are de-rotated accordingly..
2. A PSP algorithm performs blind OCHIR estimation and metric computation. The phase of the OCHIR estimate is used to estimate the residual FOA value (since frequency is simply a phase differential over time).
3. The current FOA value is updated by adding the estimated residual FOA value into the previous FOA value.
4. Steps 1-3 are repeated several times for the current FOA value.
5. The final FOA estimate is the current FOA corresponding to the best metric in the trellis, over all bins.

2.3.2.3 TOA/AOA Conversion Algorithm Development

Here we show how to develop and evaluate algorithms for the conversion of OCHIR estimates to TOA/AOA estimates. In Section 0, we discuss the estimation of the number of physical propagation paths impinging on the antenna array. If this number is known or has been estimated, the algorithms presented in Section 0 can then be used to convert the OCHIR estimates to high-quality TOA/AOA estimates.

Number of Paths Estimation (NOPE):

First the number of physical propagation paths impinging on the antenna array must be estimated. Most publications (e.g., see [24] and [25]) suggest algorithms based on two well-known Information Theoretic Criteria: the Akaike Information Criterion (AIC) [26] and the Minimum-Description Length (MDL) [27]. Two NOPE algorithms that have been derived in [28] (using these

two criteria) are discussed here. The first algorithm chooses as the number of paths to be the number p that minimizes the AIC:

$$\text{AIC}(p) = -2 \cdot \ln \left[\frac{\prod_{i=p+1}^{N_{oc}} \lambda_i^{1/(N_{oc}-p)}}{\frac{1}{N_{oc}-p} \cdot \sum_{i=p+1}^{N_{oc}} \lambda_i} \right]^{(N_{oc}-p)N_e} + 2 \cdot p \cdot (2N_{oc} - p + 1), \quad p = 1, \dots, P_{\max} \quad (2.21)$$

The second algorithm chooses as the number of paths to be the number p that minimizes the MDL:

$$\text{MDL}(p) = -\ln \left[\frac{\prod_{i=p+1}^{N_{oc}} \lambda_i^{1/(N_{oc}-p)}}{\frac{1}{N_{oc}-p} \cdot \sum_{i=p+1}^{N_{oc}} \lambda_i} \right]^{(N_{oc}-p)N_e} + \frac{1}{2} \cdot p \cdot (2N_{oc} - p + 1) \cdot \ln[N_e], \quad p = 1, \dots, P_{\max} \quad (2.22)$$

where N_e is the number of OCHIR estimates, $N_{oc} = M \cdot N_s \cdot L_s$ is the number of estimated OCHIR coefficients and $\lambda_1 > \lambda_2 \dots > \lambda_{N_{oc}}$ are the sorted eigen-values of the sample correlation matrix:

$$\mathbf{R}_{\hat{\mathbf{h}}^{(e)}} = \frac{1}{N_e} \sum_{e=0}^{N_e-1} \hat{\mathbf{h}}^{(e)} \cdot \hat{\mathbf{h}}^{(e)H}$$

Here, the $N_{oc} \times 1$ vector $\hat{\mathbf{h}}^{(e)}$ ($e = 0, \dots, N_e - 1$) is given by

$$\hat{\mathbf{h}}^{(e)} = \begin{bmatrix} \hat{\mathbf{h}}_0^{(e)T} [0] \dots \hat{\mathbf{h}}_0^{(e)T} [N_s - 1] & \dots & \hat{\mathbf{h}}_{M-1}^{(e)T} [0] \dots \hat{\mathbf{h}}_{M-1}^{(e)T} [N_s - 1] \end{bmatrix}^T$$

Notice that the maximum number of distinguishable, physical propagation paths that these algorithms can estimate is $P_{\max} = N_{oc} - 1$. For a static propagation channel these algorithms do not perform very well. This is because in a static channel, the path-correlation matrix has rank 1 instead of P (the actual number of paths), which would be the case for a time-varying, fading channel.

For the static case, various other NOPE algorithms can be developed. One possible algorithm utilizes the TOA estimates via the conversion algorithm presented in the next section in order to construct a noise-power estimate for each hypothesized number of paths. The number that yields the minimum absolute error between the corresponding noise power estimate and the (externally measured) noise power is then taken as the correct one. Such a NOPE algorithm can produce very good results when the TDOA between paths is larger than T (T being the symbol duration). When the TDOA between paths is smaller, the algorithm's success rate is smaller.

Conversion to TOA/AOA estimates:

Two conversion algorithms are now presented: the first algorithm performs joint TOA/AOA estimation. It is similar the Deterministic ML algorithm [19] applied to joint TOA/AOA estimation. The computational load , however, can be prohibitive for practical systems. A reduced-complexity algorithm that estimates the PTS first and then uses the PTS and OCHIR estimates to estimate the path-AOAs would proceed as follows:

Joint TOA/AOA Conversion Algorithm

For N_e OCHIR available estimates, the $N_s \cdot L_s \times 1$ vector

$$\hat{\mathbf{h}}_m^{(e)} = \left[\hat{\mathbf{h}}_m^{(e)\top} [0] \cdots \hat{\mathbf{h}}_m^{(e)\top} [N_s - 1] \right]^T, \quad e = 0, \dots, N_e - 1, \quad m = 0, \dots, M - 1 \quad (2.23)$$

can be written as follows:

$$\hat{\mathbf{h}}_m^{(e)} = \mathbf{V}_\tau \cdot \begin{bmatrix} a_m(\phi_{a,1}) & \cdots & 0 \\ \vdots & \ddots & \vdots \\ 0 & \cdots & a_m(\phi_{a,P}) \end{bmatrix} \cdot \mathbf{c}^{(e)} + \mathbf{w}_m^{(e)}, \quad e = 0, \dots, N_e - 1, \quad m = 0, \dots, M - 1 \quad (2.24)$$

Here, \mathbf{V}_τ is the $N_s \cdot L_s \times P$ pulse-shaping matrix (also-called the *delay manifold*), whose elements are the transmit-filter responses to each of the P physical propagation path TOA's

($\tau = [\tau_1 \ \cdots \ \tau_p]^T$) and $a^{(m)}(\phi_{a,p})$ is the array response to the p^{th} ($p = 1, \dots, P$) propagation path's azimuth AOA ($\phi_{a,p}$). The vector $\mathbf{c}^{(e)} = [c_1^{(e)} \ \cdots \ c_p^{(e)}]^T$ contains the complex gains of the P physical propagation path, and the vector $\mathbf{w}_m^{(e)}$ represents the OCHIR estimation noise. On the basis of (2.24), the authors in [24] and [25] have extended "classic" AOA-only estimation algorithms (such as Stochastic Maximum Likelihood, MUSIC, ESPRIT [15]) to the problem of the joint TOA/AOA estimation. The algorithms in these references, however, are utilizing OCHIR estimates that have been obtained using multiple training-sequences. In this case, the statistical properties of the OCHIR estimation noise are presumed known and all algorithms from the "classic" array-processing literature are applicable.

For blind OCHIR estimation, the statistical properties of the OCHIR estimation noise are difficult to know in advance. An alternative is a least-squares fitting in order to derive an algorithm for joint TOA/AOA estimation. In other words, TOA, AOA, and complex gain estimates can be obtained by minimizing the following squared norm with respect to all desired parameters:

$$\|\hat{\mathbf{H}} - \mathbf{V}_{\tau,\phi} \cdot \mathbf{C}\|^2 \quad (2.25)$$

where

$$\hat{\mathbf{H}} = \begin{bmatrix} \hat{\mathbf{h}}^{(0)} & \dots & \hat{\mathbf{h}}^{(N_e-1)} \end{bmatrix} \quad \text{and} \quad \hat{\mathbf{h}}^{(e)} = \begin{bmatrix} \hat{\mathbf{h}}_0^{(e)T} & \dots & \hat{\mathbf{h}}_{M-1}^{(e)T} \end{bmatrix}^T, \quad e=0, \dots, N_e-1$$

$$\mathbf{V}_{\tau, \phi} = \begin{bmatrix} \mathbf{V}_{\tau, \phi, 0} \\ \vdots \\ \mathbf{V}_{\tau, \phi, M-1} \end{bmatrix}, \quad \text{and} \quad \mathbf{V}_{\tau, \phi, m} = \mathbf{V}_\tau \cdot \begin{bmatrix} a_m(\phi_{a,1}) & \dots & 0 \\ \vdots & \ddots & \vdots \\ 0 & \dots & a_m(\phi_{a,P}) \end{bmatrix}, \quad m=0, \dots, M-1$$

$$\mathbf{C} = \begin{bmatrix} \mathbf{c}^{(0)} & \dots & \mathbf{c}^{(N_e-1)} \end{bmatrix}$$

The LS Estimates (LSE) of all TOAs, AOAs, and complex gains are obtained by first minimizing the squared norm in (2.25) with respect to the complex gains and then minimizing the resulting function with respect to the TOAs and AOAs. The LSE of the complex gains is

$$\hat{\mathbf{C}} = \left[\mathbf{V}_{\tau, \phi}^H \cdot \mathbf{V}_{\tau, \phi} \right]^{-1} \cdot \mathbf{V}_{\tau, \phi}^H \cdot \hat{\mathbf{H}} \quad (2.26)$$

Substituting in (2.25), estimates of the TOAs and AOAs can be obtained as follows:

$$\hat{\mathbf{t}}, \hat{\mathbf{phi}} = \arg \min_{\tau, \phi} \left\{ -\text{trace} \left(\mathbf{P}_{\mathbf{V}_{\tau, \phi}} \cdot \mathbf{R}_{\hat{\mathbf{h}}^{(e)}} \right) \right\} \quad (2.27)$$

where

$$\mathbf{P}_{\mathbf{V}_{\tau, \phi}} = \mathbf{V}_{\tau, \phi} \cdot \left[\mathbf{V}_{\tau, \phi}^H \cdot \mathbf{V}_{\tau, \phi} \right]^{-1} \cdot \mathbf{V}_{\tau, \phi}^H$$

and

$$\mathbf{R}_{\hat{\mathbf{h}}^{(e)}} = \frac{1}{N_e} \sum_{e=0}^{N_e-1} \hat{\mathbf{h}}^{(e)} \cdot \hat{\mathbf{h}}^{(e)H}$$

Joint TOA/AOA estimation of this form requires a $3P$ -dimensional minimization of the function in (2.27). Such a procedure is computationally prohibitive, especially when the number of physical propagation paths is large. A reduced-complexity TOA/AOA conversion algorithm would first estimate the path-TDOA's and then use them to estimate the path-AOA's, employing only P two-dimensional minimization procedures. This algorithm is described in the next subsection.

Reduced-Complexity TOA/AOA Conversion Algorithm

First collect all OCHIR estimates in a $N_s \cdot L_s \times M \cdot N_e$ matrix:

$$\hat{\mathbf{H}}_\tau = \begin{bmatrix} \hat{\mathbf{h}}_0^{(0)} \dots \hat{\mathbf{h}}_0^{(N_e-1)} \hat{\mathbf{h}}_1^{(0)} \dots \hat{\mathbf{h}}_1^{(N_e-1)} \dots \hat{\mathbf{h}}_{M-1}^{(0)} \dots \hat{\mathbf{h}}_{M-1}^{(N_e-1)} \end{bmatrix} \quad (2.28)$$

This matrix can be written as follows:

$$\hat{\mathbf{H}}_\tau = \mathbf{V}_\tau \cdot \mathbf{C}_\phi + \hat{\mathbf{W}} \quad (2.29)$$

where \mathbf{C}_ϕ is a $P \times M \cdot N_e$ matrix containing the complex gains of the P physical propagation paths and $\hat{\mathbf{W}}$ is a $N_s \cdot L_s \times M \cdot N_e$ matrix representing the OCHIR estimation noise. An LSE criterion can estimate the path TOA's for the above model, and \mathbf{C}_ϕ can be obtained by minimizing:

$$\|\hat{\mathbf{H}}_\tau - \mathbf{V}_\tau \cdot \mathbf{C}_\phi\|^2 \quad (2.30)$$

The LSE are obtained by first minimizing the above with respect to \mathbf{C}_ϕ , and then minimizing the resulting function with respect to the path TOA's. The LSE of \mathbf{C}_ϕ is given by

$$\hat{\mathbf{C}}_\phi = [\mathbf{V}_\tau^H \cdot \mathbf{V}_\tau]^{-1} \cdot \mathbf{V}_\tau^H \cdot \hat{\mathbf{H}}_\tau \quad (2.31)$$

Substituting these LSE's into (2.30), the path-TOAs estimates can be obtained as:

$$\hat{\mathbf{t}} = \arg \min_{\mathbf{t}} \left\{ -\text{trace} \left(\mathbf{P}_{\mathbf{V}_\tau} \cdot \mathbf{R}_{\hat{\mathbf{h}}_m^{(e)}} \right) \right\} \quad (2.32)$$

where

$$\mathbf{P}_{\mathbf{V}_\tau} = \mathbf{V}_\tau \cdot [\mathbf{V}_\tau^H \cdot \mathbf{V}_\tau]^{-1} \cdot \mathbf{V}_\tau^H$$

and

$$\mathbf{R}_{\hat{\mathbf{h}}_m^{(e)}} = \frac{1}{M \cdot N_e} \sum_{m=0}^{M-1} \sum_{e=0}^{N_e-1} \hat{\mathbf{h}}_m^{(e)} \cdot \hat{\mathbf{h}}_m^{(e)H}$$

After the path TOAs, the LSE's \mathbf{C}_ϕ are obtained as

$$\hat{\mathbf{C}}_\phi = [\mathbf{V}_{\hat{\mathbf{t}}}^H \cdot \mathbf{V}_{\hat{\mathbf{t}}}]^{-1} \cdot \mathbf{V}_{\hat{\mathbf{t}}}^H \cdot \hat{\mathbf{H}}_\tau$$

Here, each row, $\hat{\mathbf{C}}_{\phi,p}$, of this matrix depends on the AOAs of only one path:

$$\hat{\mathbf{C}}_{\phi,p} = [a_0(\hat{\phi}_{a,p}) \cdot \hat{c}_p^{(0)} \cdots a_0(\hat{\phi}_{a,p}) \cdot \hat{c}_p^{(N_e-1)} \quad \dots \quad a_{M-1}(\hat{\phi}_{a,p}) \cdot \hat{c}_p^{(0)} \cdots a_{M-1}(\hat{\phi}_{a,p}) \cdot \hat{c}_p^{(N_e-1)}]$$

Re-arranging these estimates, we get

$$\left[\hat{\mathbf{c}}_{\phi,p}^{(0)} \cdots \hat{\mathbf{c}}_{\phi,p}^{(N_e-1)} \right] = \mathbf{a}_{\phi,p} \cdot \mathbf{c}_p + \hat{\mathbf{w}}_p = \begin{bmatrix} a_0(\phi_{a,p}) \\ a_1(\phi_{a,p}) \\ \vdots \\ a_{M-1}(\phi_{a,p}) \end{bmatrix} \cdot \left[c_p^{(0)} \cdots c_p^{(N_e-1)} \right] + \hat{\mathbf{w}}_p \quad (2.33)$$

The LSE's of the AOAs of the p^{th} path are

$$\hat{\boldsymbol{\phi}}_p = \left[\hat{\phi}_{a,p} \right] = \arg \min_{\boldsymbol{\phi}_p} \left\{ -\text{trace} \left(\mathbf{P}_{\mathbf{a}_{\phi,p}} \cdot \mathbf{R}_{\hat{\mathbf{c}}_{\phi,p}^{(e)}} \right) \right\} \quad (2.34)$$

where

$$\mathbf{P}_{\mathbf{a}_{\phi,p}} = \mathbf{a}_{\phi,p} \cdot \left[\mathbf{a}_{\phi,p}^H \cdot \mathbf{a}_{\phi,p} \right]^{-1} \cdot \mathbf{a}_{\phi,p}^H$$

and

$$\mathbf{R}_{\hat{\mathbf{c}}_{\phi,p}^{(e)}} = \frac{1}{N_e} \sum_{e=0}^{N_e-1} \hat{\mathbf{c}}_{\phi,p}^{(e)} \hat{\mathbf{c}}_{\phi,p}^{(e)H}$$

It follows from (2.32) and (2.34) that this TOA/AOA conversion algorithm requires a $(P-1)$ -dimensional minimization for TOA and a $(P-2)$ -dimensional minimization for AOA; therefore, it is easier to implement than the joint TOA/AOA conversion. This algorithm can achieve the Cramer-Rao Lower Bound (CRLB) in all scenarios where the path TDOA's are larger than $T/10$. For path TDOA's less than $T/10$, the algorithm fails to produce reliable TOA/AOA estimates. In these cases, the paths are indistinguishable in the time domain and can be separated only in the spatial domain.

2.3.3 Performance assessment

The performance of the PTS-AOA estimation algorithm is now assessed a GMSK-modulated signal, impinging on a 4-element uniform linear array with $\lambda/2$ inter-element spacing. Two propagation scenarios are demonstrated, whose parameters are provided in Table 1 and Table 2. The first scenario is a typical example of a coherent multipath environment. Here, only one temporal path can be physically distinguished and two spatial paths can be separated [16]. The second scenario is when the number of spatial paths exceeds the number of array elements. Here, there are only three distinct temporal paths. For both scenarios, there is only one observation data block available, consisting of 100 symbol spaced samples. OCHIR estimation is achieved via the PSP algorithm. The sample Root-Mean Squared Error (RMSE) for the estimates is shown and compared it to the appropriate CRLB, derived in [30].

Table 1: Propagation Scenario 1.

Path Parameters	Parameters Values	
	Direct Path	Reflected Path
TOA (symbol time)	0	0.01
AOA (degrees)	20	30
Power (normalized)	0.67	0.33

Table 2: Propagation Scenario 2.

Path Parameters	Parameters Values				
	Direct Path	Reflected Path1	Reflected Path2	Reflected Path3	Reflected Path4
TOA (symbol time)	0	1.0	1.01	2.0	2.02
AOA (degrees)	20	30	35	-5	-10
Power (normalized)	0.5	0.15	0.15	0.10	0.10

The AOA-RMSE results of Figure 9 and Figure 10 show that there is very good agreement between the estimation performance of the PTS-AOA estimation algorithm and the CRLB. Similar agreement can be observed in Figure 11. The results of Figure 11 clearly demonstrate that, when there is sufficient temporal separation between the propagation paths, the algorithm can provide very reliable AOA estimation even when the number of spatial paths exceeds the number of array elements. Figure 12 presents the PTS-RMSE results for the second scenario. Since the CRLB in [30] calculates the TOA-RMSE and not the PTS-RMSE, we have not plotted the bound in this Figure. The PTS-RMSE results show that very good estimation performance (less than 10% of the symbol time) can be achieved for SNR values higher than 15dB.

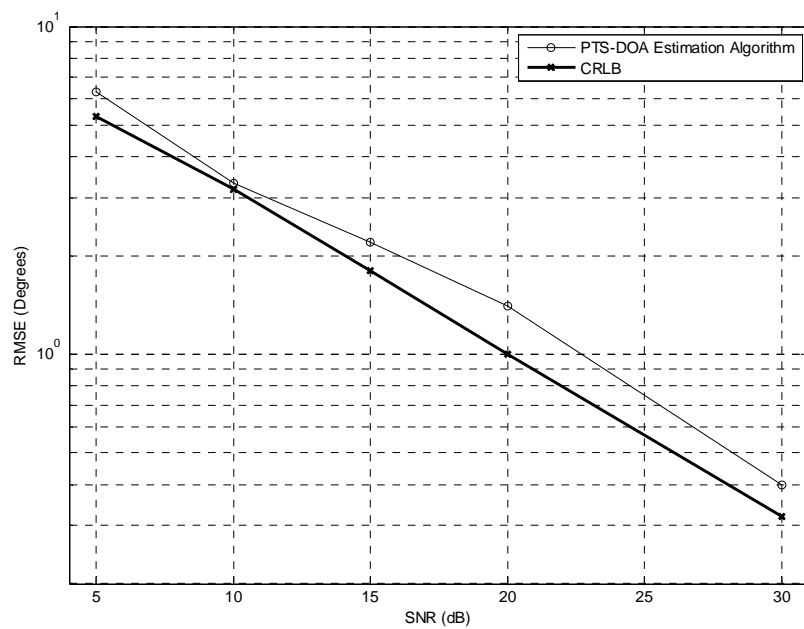


Figure 9: Scenario 1 – Direct-Path AOA Estimation.

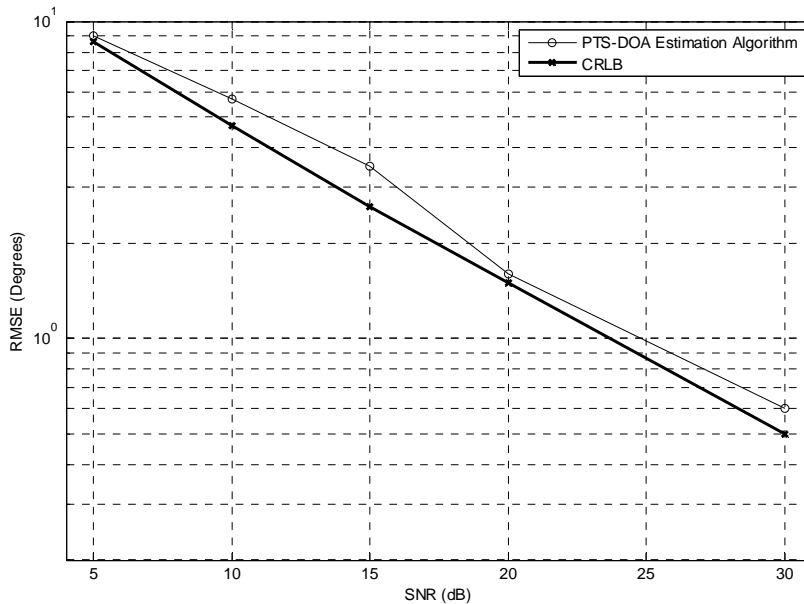


Figure 10: Scenario 1 – Reflected-Path AOA Estimation.

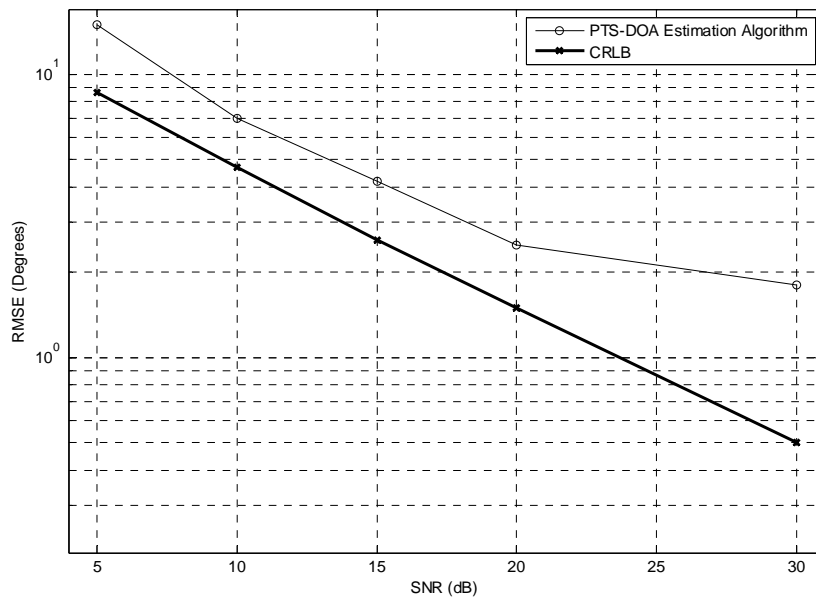


Figure 11: Scenario 2 – Direct-Path AOA Estimation.

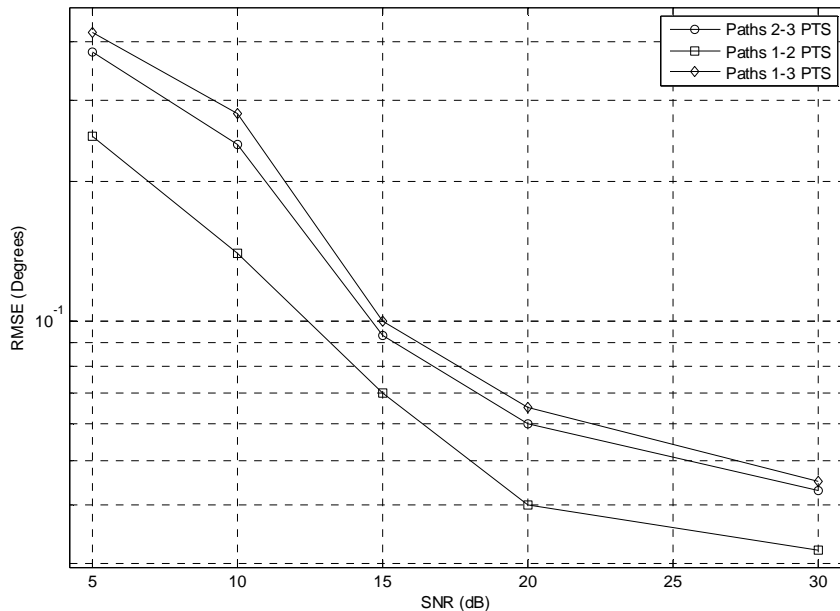


Figure 12: Scenario 2 – PTS Estimation.

2.4 Fusion methods for localization

2.4.1 Introduction to fusion methods

What we call “fusion methods” here include all these techniques that combine the different measurements/estimates from all sensors in order to localize the active sources. Several fusion techniques have been introduced in the literature; these techniques depend on what signal parameters are measured at the sensors. As already mentioned, the most common signal parameters are the time of arrival, time difference of arrival, angle of arrival and receive signal strength. Two main categories of such techniques are the probabilistic and non-probabilistic. This categorization is based on the existence or proper use of soft information from the sensors. Herein, a small overview of basic fusion techniques is given for localizing *single* sources for both categories. A huge amount of variations of those basic techniques exist in the literature along with more complicated scenarios. An excellent review of those can be found in [32] and the references therein. A novel fusion technique for multiple source characterization/localization is presented at the next chapter.

2.4.2 Description of basic fusion methods

2.4.2.1 Non probabilistic LS based fusion

The combination of TOA/TDOA/AOA/RSS measurements to localize a transmitter from multiple (more than three) sources involves the solution of an over-determined system of equations. Overviews of the different systems that emerge based on the type of measurements have been presented in [33]. Based on this work, a description of a generic system that includes all the different cases will be provided herein. Ignoring the z-coordinates for simplicity, let (x_i, y_i) denote the position of the *i-th sensor*, r_i the distance of the *i-th sensor* from the source that we want to estimate, and $\mathbf{x} = [x, y]^T$ its position. Without loss of generality the origin of the Cartesian coordinate system is set at the first sensor, $(x_1, y_1) = (0, 0)$. The generic form of the over-determined system of equations can be written as [33]

$$\mathbf{Hx} = \mathbf{b}$$

where for the various basic problems we have the specific forms as follows:

TOA:

$$\mathbf{H} = \begin{bmatrix} x_2 & y_2 \\ \vdots & \vdots \\ x_N & y_N \end{bmatrix}, \quad \mathbf{x} = \begin{bmatrix} x \\ y \end{bmatrix} \text{ and } \mathbf{b} = \begin{bmatrix} d_2^2 - r_2^2 + r_1^2 \\ \vdots \\ d_N^2 - r_N^2 + r_1^2 \end{bmatrix}$$

where $r_i = (t_i - t_0)c$ and $d_i^2 = x_i^2 + y_i^2$

TDOA:

$$\mathbf{H} = \begin{bmatrix} x'_2 & x'_2 & \frac{r_{2,1}}{2} \\ \vdots & \vdots & \vdots \\ x'_N & x'_N & \frac{r_{N,1}}{2} \end{bmatrix}, \mathbf{x} = \begin{bmatrix} x \\ y \\ r_1 \end{bmatrix}, \text{ and } \mathbf{b} = \begin{bmatrix} d'_2 - r_{21}^2 \\ \vdots \\ d'_N - r_{N1}^2 \end{bmatrix}$$

where $r_{i1} = r_i - r_1 = (t_i - t_1)c$, $x'_i = x_i - x_1$, $y'_i = y_i - y_1$ and $d'_i = x_i^2 - x_1^2 + y_i^2 - y_1^2$

AOA:

$$\mathbf{H} = \begin{bmatrix} -\sin(a_1) & \cos(a_1) \\ \vdots & \vdots \\ -\sin(a_N) & \cos(a_N) \end{bmatrix}, \text{ and } \mathbf{b} = \begin{bmatrix} 0 \\ -x_2 \sin(a_2) + y_2 \cos(a_2) \\ \vdots \\ -x_N \sin(a_N) + y_N \cos(a_N) \end{bmatrix}$$

where a_i is the estimated AOA of i -th sensor, i.e. $a_i = \arctan\left(\frac{x - x_i}{y - y_i}\right)$

For RSS (following similar manipulation as in TDOA [30] case)

$$\mathbf{H} = \begin{bmatrix} x_2 & y_2 \\ \vdots & \vdots \\ x_N & y_N \end{bmatrix} \text{ and } \mathbf{b} = r_1^2 \mathbf{c} + \mathbf{d}, \text{ where } \mathbf{c} = \begin{bmatrix} \frac{p_{rx,2} - p_{rx,1}}{5\gamma} \\ 1 - 10 \\ \vdots \\ \frac{p_{rx,N} - p_{rx,1}}{5\gamma} \end{bmatrix} \quad \mathbf{d} = \begin{bmatrix} d_2^2 \\ \vdots \\ d_N^2 \end{bmatrix}$$

Solved together with

$$r_1^2 = x^2 + y^2$$

where $p_{rx,i} = p_{tx} - 10\gamma \log_{10}(r_i / r_0) - C$

The generic LS solution of the corresponding over-determined system of equations by the use of the pseudo-inverse matrix is given by

$$\hat{\mathbf{x}} = (\mathbf{H}^T \mathbf{H})^{-1} \mathbf{H}^T \mathbf{b}$$

It is a cheap way to perform localization, sensitive though to the geometry of the sensors with respect to the position of the source and the errors of the measurements. They induce singularities to the matrices used that may deteriorate the position accuracy, or even make it impossible. Some works provide solutions to overcome these singularities based on Total Least squares criterion.

2.4.2.2 Probabilistic ML fusion

In the general case, we can model the measurements of the sensors as

$$\boldsymbol{\beta} = \theta(\mathbf{x}) + \boldsymbol{\epsilon}$$

where $\theta(\cdot)$ is a non-linear function of the position of the source, described at the previous section for four types of measurements, and $\boldsymbol{\epsilon}$ is the additive noise of the measurements assumed to be a zero mean Gaussian vector with a covariance matrix $\mathbf{S} = \text{diag}\{\sigma_1^2, \dots, \sigma_N^2\}$. The ML estimator of the location of the transmitter is given by

$$\begin{aligned}\hat{\mathbf{x}} &= \arg \min_{\mathbf{x}} (\theta(\mathbf{x}) - \boldsymbol{\beta})^T \mathbf{S}^{-1} (\theta(\mathbf{x}) - \boldsymbol{\beta}) \\ &= \arg \min_{\mathbf{x}} \left(\sum_{i=1}^N \frac{(\theta(\mathbf{x}) - \beta_i)^2}{\sigma_i^2} \right)\end{aligned}$$

This non-linear minimization problem can be solved with proper linearization, as long as we have an initial estimate close to the true minimum. This linearization can be done by using the first order Taylor approximation of $\theta(\mathbf{x})$ at \mathbf{x}_0 ,

$$\theta(\mathbf{x}) = \theta(\mathbf{x}_0) + \mathbf{P}(\mathbf{x} - \mathbf{x}_0)$$

where

$$[\mathbf{P}]_{i,j} = \left. \frac{\partial [\theta(\mathbf{x})]_i}{\partial [\mathbf{x}]_j} \right|_{\mathbf{x}=\mathbf{x}_0}$$

$[\mathbf{P}]_{i,j}$ is the (i,j) -th element of matrix \mathbf{P} and $\partial[\mathbf{x}]_j$ the j -th element of vector \mathbf{x} . A Newton-Gauss iteration the ML solution is given by:

$$\hat{\mathbf{x}}_{k+1} = \hat{\mathbf{x}}_k + (\mathbf{P}_{x_k}^T \mathbf{S}^{-1} \mathbf{P}_{x_k})^{-1} \mathbf{P}_{x_k}^T \mathbf{S}^{-1} (\boldsymbol{\beta} - \theta(\mathbf{x}_k))$$

For the different cases of $\theta(\mathbf{x})$ the first derivative is given by:

TOA:

$$\mathbf{P}_{x_k}^T = \frac{1}{c} \begin{bmatrix} \cos \phi_1 & \cdots & \cos \phi_N \\ \sin \phi_1 & \cdots & \sin \phi_N \end{bmatrix}$$

TDOA:

$$\mathbf{P}_{x_k}^T = \frac{1}{c} \begin{bmatrix} \cos\phi_2 - \cos\phi_1 & \dots & \cos\phi_N - \cos\phi_1 \\ \sin\phi_2 - \sin\phi_1 & \dots & \sin\phi_N - \sin\phi_1 \end{bmatrix}$$

AOA:

$$\mathbf{P}_{x_k}^T = \frac{1}{c} \begin{bmatrix} -\frac{\sin\phi_1}{d_1} & \dots & -\frac{\sin\phi_N}{d_N} \\ \frac{\cos\phi_1}{d_1} & \dots & \frac{\cos\phi_N}{d_N} \end{bmatrix}$$

RSS:

$$\mathbf{P}_{x_k}^T = \frac{1}{c} \begin{bmatrix} -\frac{\sin\phi_1}{d_1} & \dots & -\frac{\sin\phi_N}{d_N} \\ \frac{\cos\phi_1}{d_1} & \dots & \frac{\cos\phi_N}{d_N} \end{bmatrix}$$

where

$$\cos\phi_i = \frac{x_i - x}{d_i} \text{ and } \sin\phi_i = \frac{y_i - y}{d_i}$$

The ML approach attains the CRB in performance but with the cost of increase complexity. Bad convergence could appear based on the geometry of the sensors. In any way, a good initial point is always needed to ensure convergence and reduce the complexity. Usually a closed form method for an initial estimate is used, like those presented in the previous section.

2.4.3 Performance assessment

Some indicative performance results will be presented based on a generic scenario. We assume a square area of 1km². The SNR of the estimated parameters β is defined as

$$\gamma_d(\beta) = \frac{1}{\sigma_\beta^2}$$

where σ_β^2 is the common variance of the additive noise ϵ , defined in previous section. Results for TOA and AOA based fusion will be displayed. For the TOA case the σ_β^2 is measured in microsecond, while for AOA in radians. In Figure 13 an illustrative example of TOA and AOA based localization is given for an γ_d of 15dB. We assume that all sensors to have the same γ_d . Four sensors are used around the source of interest, placed at the middle. This is not problematic sensor geometry as it can be observed by the geometry of the error surface. The MSE comparison of LS

and ML methods for the same experiment and for an SNR range of 5 to 15dB is displayed at Figure 16. The ML methods exhibit superior performance than the LS, as expected, with the cost of increased complexity. Results from problematic sensor geometry are displayed at Figure 15, again for γ_d of 15dB and four sensors. The high sensitivity of the localization error due to the geometry of the sensors around the sources can be deduced by a visual comparison with Figure 13.

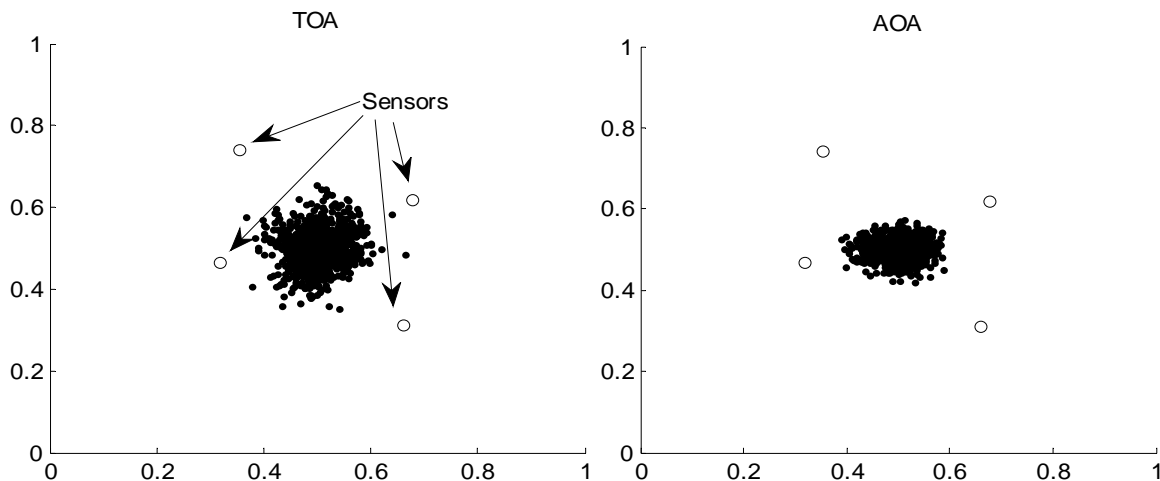


Figure 13: Location estimates for decision SNR of 15dB.

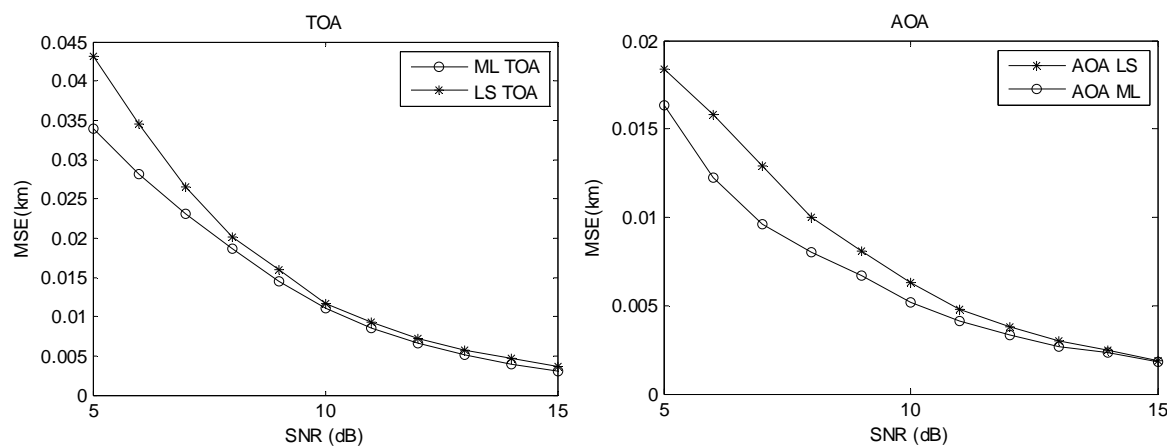


Figure 14: MSE in Km for the TOA and AOA based fusion.

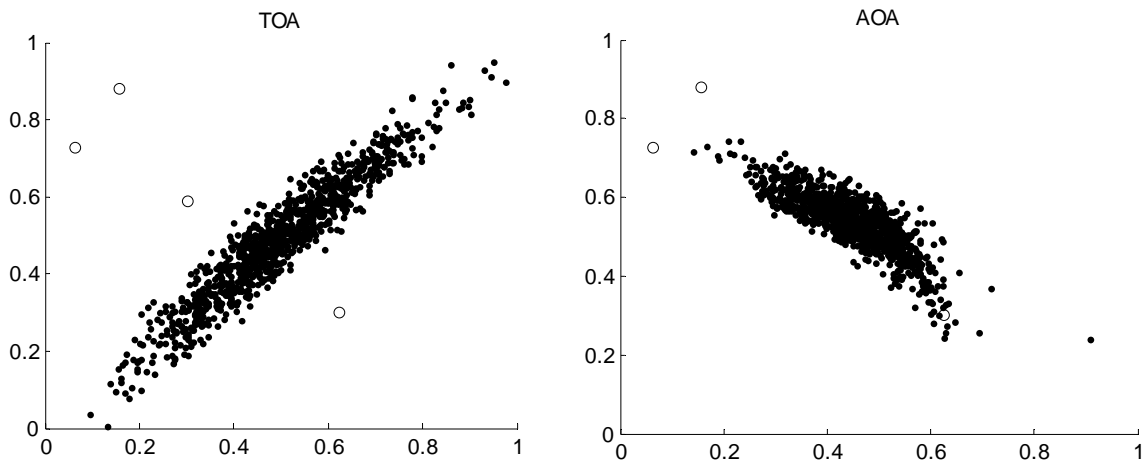


Figure 15: Location estimates for decision SNR of 15dB (problematic geometry).

2.5 Joint transmit power estimation and localization

2.5.1 State of the Art and model description

In this section we present an indirect method that obtains the RIFE by estimating the number, location and average power of the transmitting sources. Processing is based on the maximization of the likelihood function (the ML criterion). Such a technique is therefore one of arbitrary topology and probabilistic processing on the obtained measurements. In a similar setting, location and power estimation for a single-source, also based on the ML criterion, has been derived recently in [38]. The present section can be viewed as a generalization to many (and unknown in number) sources of the work in [38]. Log-normal shadow fading is incorporated in the statistical model. A number of sensors measuring power are assumed placed in known locations; we then compute the pdf of the obtained measurements, conditioned on a specific arrangement regarding the location, number and average power of the transmitting sources. We then maximize this conditional pdf over all such different arrangements. How to avoid a straightforward (and computationally intensive) exhaustive search is also discussed in the next sub-sections.

The problem of separating signal sources and identifying their number is a well-known, interesting problem. For a solution to it the reader is referred to Chung et al, [39]. This problem, however, becomes harder when combined with inference, as is the case here. In order to alleviate the difficulty of double uncertainty (i.e., number of sources and their power), we assume a grid of candidate source locations over the geographical area of interest, namely the area where the sources are actually expected to lie in; we then investigate the existence of sources on the points determined by this grid only. The resolution and coordinates of this grid are therefore critical. Their choice depends on the desired level of estimation accuracy as well as on the fading spatial characteristics. So, every grid location is a candidate source location; if a source is deemed present, we compute its power. In order to reduce the number of searchable spatial parameters, the

algorithm can be implemented so as to successively refine the resolution of the grid (say, in geographical areas where this is meaningful, i.e., where sensors are placed sufficiently densely).

We consider N sensors located in known places in the geographic area of interest, each measuring the power at this location and at a specific frequency bin and time instant. Let P_r^1, \dots, P_r^N be the collection of these measurements. As mentioned, we consider an environment described by shadow fading and path loss. In such an environment P_r^k is a random variable, for all $k \in \{1, \dots, N\}$, namely

$$P_r^k = \sum_{i=1}^S \frac{1}{d_{ik}^\alpha} H_{ik} P_t^i + \sigma_k^2$$

Here, σ_k^2 models the variance of the additive zero-mean Gaussian thermal noise corresponding to the k -th sensor and P_t^i is the unknown transmitted power corresponding to the i -th among all S possibly transmitting sources. The parameter d_{ik} is the distance between the i th possibly transmitting source and the k th sensor; α is the path-loss exponent that is assumed to be known. The propagation randomness in the above model is introduced by the shadow fading component H_{ik} which is modeled as a log-normally distributed r.v. This is generated by exponentiating a zero-mean and σ^2 -variance Gaussian random variable, henceforth referred to as $\text{InN}(0, \sigma^2)$. Note that σ^2 is assumed to be known and identical for all source-sensor pairs. The shadow-fading components are modeled as uncorrelated. This is based on the practical knowledge (see [40]) that spatial correlation drops quickly at small distances (a few meters).

2.5.2 Algorithm description

In this section we state the main result, namely the computation of the joint probability density characterizing the observations P_r^1, \dots, P_r^N . We note that the power received at each sensor depends probabilistically only on the values of the shadow fading between this specific sensor and each of the sources and is hence independent of the power received by any of the other sensors within the specified area. For a particular combination of sources transmitting some power within this area, the joint distribution of the power received at all sensors is hence a multiplication of the power distribution at each sensor. It hence suffices to describe the distribution of the power at each sensor separately.

For each $k \in \{1, \dots, N\}$ $P_r^k - \sigma_k^2$ can be approximated by a log-normally distributed random variable $\text{InN}(\mu_{p_k}, \beta_{p_k})$, where

$$\mu_{p_k} = \ln \left(\sum_{i=1}^S \frac{P_t^i}{(d_{ik})^\alpha} \right) + \frac{\sigma^2}{2} - \frac{\beta_{p_k}}{2}$$

$$\beta_{p_k} = \ln \left((e^{\sigma^2} - 1) \frac{\sum_{i=1}^s \left(\frac{P_t^i}{(d_{ik})^\alpha} \right)^2}{\left(\sum_{i=1}^s \frac{P_t^i}{(d_{ik})^\alpha} \right)^2} + 1 \right)$$

This is essentially derived from the approximation of the distribution of a sum of independent log-normally distributed random variables of Fenton and Wilkinson [36].

The joint probability law of the power received by all sensors is then given by

$$(P_r^1 - \sigma_1^2, \dots, P_r^N - \sigma_N^2) \sim \prod_{k=1}^N \text{ln}N(\mu_{p_k}, \beta_{p_k})$$

The goal is to maximize this multiplicative law for all possible combinations of P_t^1, \dots, P_t^s . This yields a non-convex optimization problem that can only be solved numerically. To this end, global optimization techniques, and in particular simulated annealing ([37]), are employed. Numerical results for such maximization are presented in the following section.

2.5.3 Performance assessment

2.5.3.1 Generic scenario

We consider two transmitting sources (of power 100 and 50, respectively) at some fixed positions in a geographical area of size 100x100 (all units are normalized to any desirable measure). Furthermore, sensors of known number and location, distributed uniformly in this area, measure the received power. As mentioned, we employ the ML technique on a pre-selected grid (of size possibly variable) in order to estimate the number and power of transmitting sources. We plot the estimated power on the points of actual transmission (points 1 and 2 in Figure 16) and on two points placed vertically to the sources (points 3 and 4 in Figure 16). Simulations are for a grid of 9 candidate locations ($S=9$), except for section 0 where the grid size is variable; also, $\alpha=2$. We employ standard convex optimization except for section 0, where simulated annealing is employed (we note that, for large grid-sizes, convex optimization typically fails to converge to the global optimum). The employment of a grid necessarily creates irreducible location errors. However, it is clear that the grid-induced error can become arbitrarily small by increasing its density.

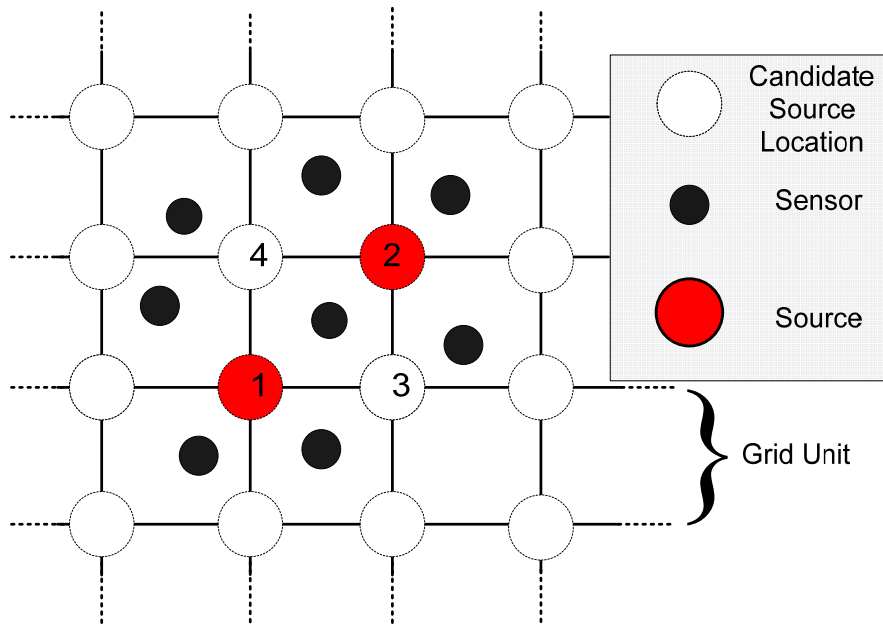


Figure 16: The ML technique on a specific configuration.

Effect of the number of sensors

Simulations were performed in order to investigate the effect of the number of sensors on the average estimated power. It can be seen in Figure 17 that increasing the number of sensors beyond some level (approximately 10) does not result in higher estimation accuracy. Simulations were performed also in different settings (higher grid density or different source positions) and it was observed that the optimal number of sensors (when uniformly distributed in space) is characterized by the grid size and, in particular, that it is $O(S)$.

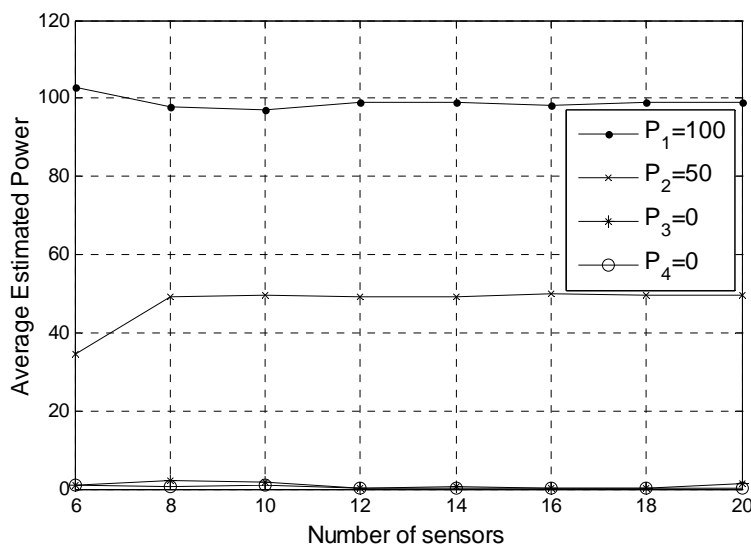


Figure 17: Effect of the number of sensors.

Effect of the grid size

The performance of the ML technique was investigated for variable grid size selection. In particular, by employing simulated annealing and with randomly chosen initial conditions, the estimated power is computed and depicted in Figure 18.

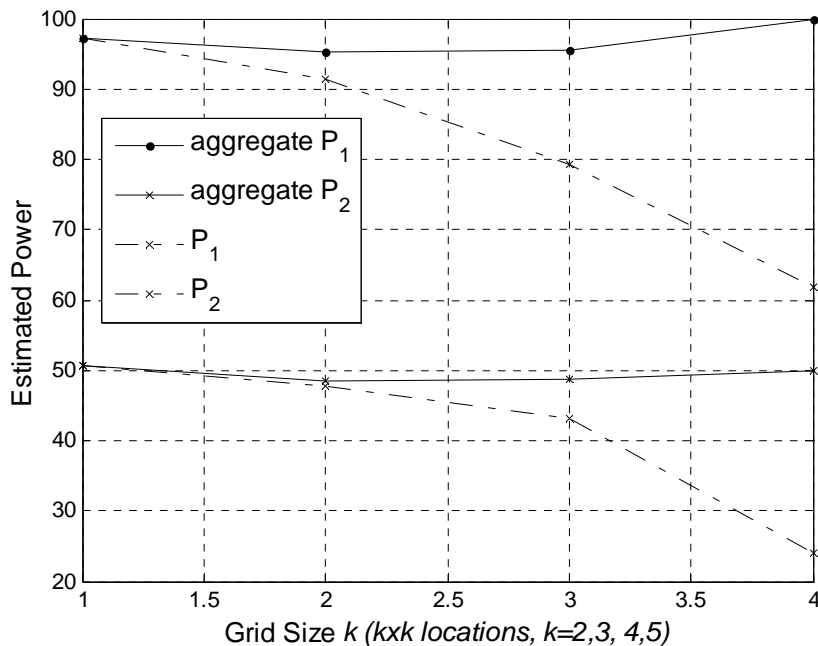


Figure 18: Effect of the grid size.

It can be observed that when the grid inter-point distance is small (dense grid), the estimated power at the actual sources' positions decreases, since substantial power is estimated also in adjacent locations around the actual ones (i.e., a spatial "diffusion" of the true power). In Figure 18 the aggregate estimated power around the location of source 1 and 2 respectively is also shown.

Effect of the shadow fading variance

The effect of the shadow fading variance (σ) was investigated in two cases: (a)when σ is assumed equal to 0.5 but, in reality, it varies between 0.1 and 1; and (b)when σ is known.

i) **Shadow Fading Variance Unknown** (hypothesized $\sigma=0.5$)

The effect of the shadow fading variance was investigated, when σ is actually unknown but is considered to be $\sigma=0.5$. It can be observed that when σ is unknown, it is in fact beneficial to overestimate it than to underestimate it, since the performance is more sensitive to the latter.

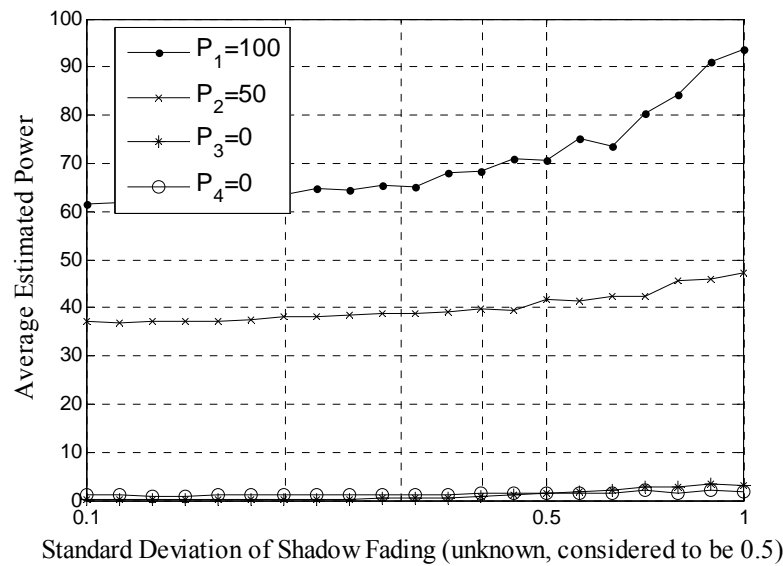


Figure 19: Effect of the shadow fading variance (when unknown).

ii) Shadow Fading Variance Known

Figure 20 depicts the effect of the shadow fading variance (when known) on the performance of the algorithm. The estimated power on the actual sources' locations decreases when σ increases, and also sources of substantial power are estimated elsewhere in the area. For higher values of the fading variance ($\sigma > 1$) the estimated power is higher in locations other than the actual sources' locations and the algorithm introduces localization error. Figure 20 depicts also a comparison of the performance when the variance is either known or unknown (performance is identical for $\sigma=0.5$ as expected).

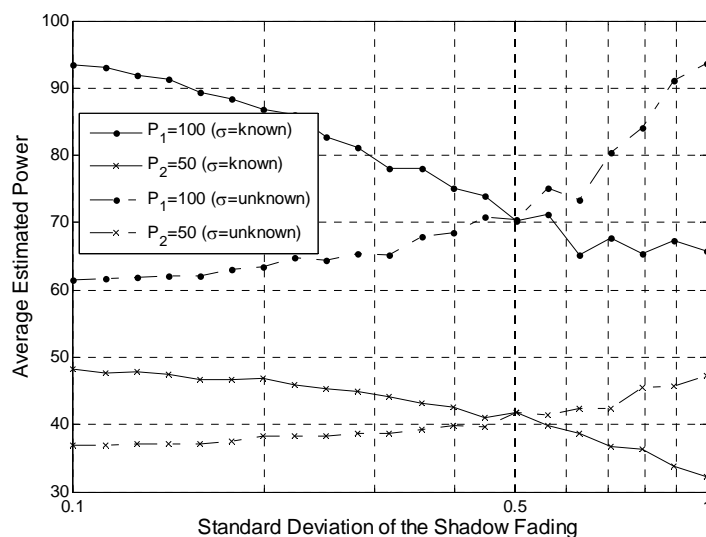


Figure 20: Effect of the shadow fading variance (when known).

Effect of an unknown additive noise

The effect of thermal noise on the performance is investigated in this subsection. In particular, we consider the following model for the received power:

$$P_r^k = \sum_{i=1}^S \frac{1}{d_{ik}^\alpha} H_{ik} P_t^i + \sigma_k |U|,$$

where U is a standard Gaussian random variable.

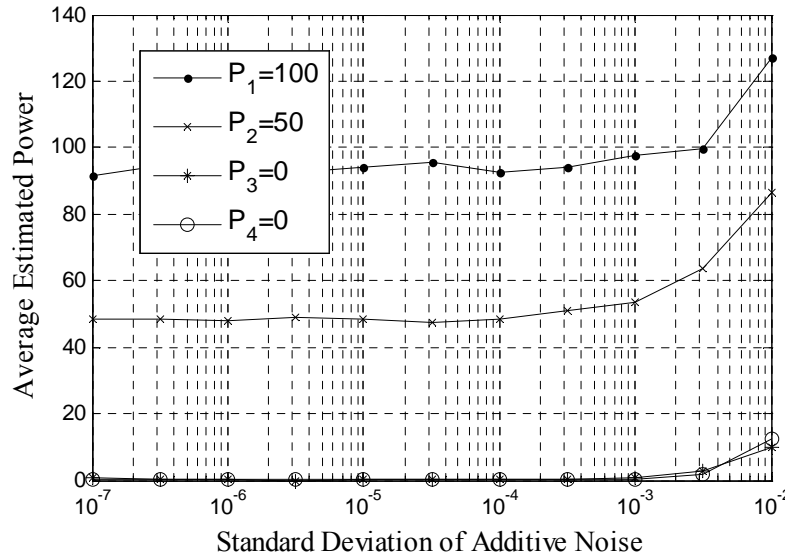


Figure 21: Effect of the additive noise variance.

We consider that the sensors are oblivious to the presence of thermal noise (both for its presence as well as for its statistics) and therefore the ML technique is employed just as described in the previous sections. In Figure 21, it can be seen that for $\sigma_k > 0.01$ the algorithm's performance is poor.

Effect of fast fading

The case where transmission is performed over multiple frequency bins is treated in this subsection. We assume that the frequency bins are far enough that the fast fading variables are independent. In particular, we consider:

$$P_r^k = \sum_{i=1}^S \frac{1}{2nd_{ik}} H_{ik} Z_{ik} P_t^i + \sigma_k^2$$

where Z_{ik} , for all $i=1,\dots,S$ and $k=1,\dots,N$, are independent chi-square distributed variables of order $2n$.

Figure 22 and Figure 23 show the mean and the variance, respectively, of the power estimation technique. It can be seen that increasing the number of (independently-fading) frequency bins is beneficial, as expected.

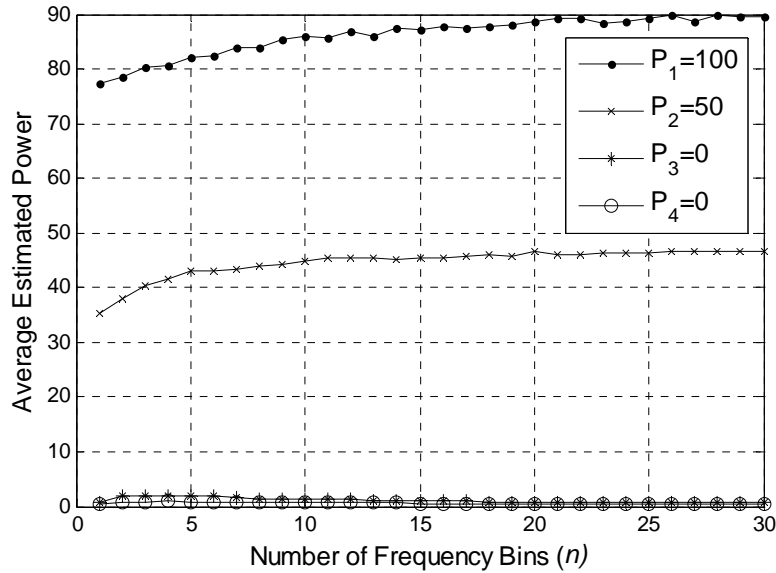


Figure 22: Effect of the number of frequency bins (mean).

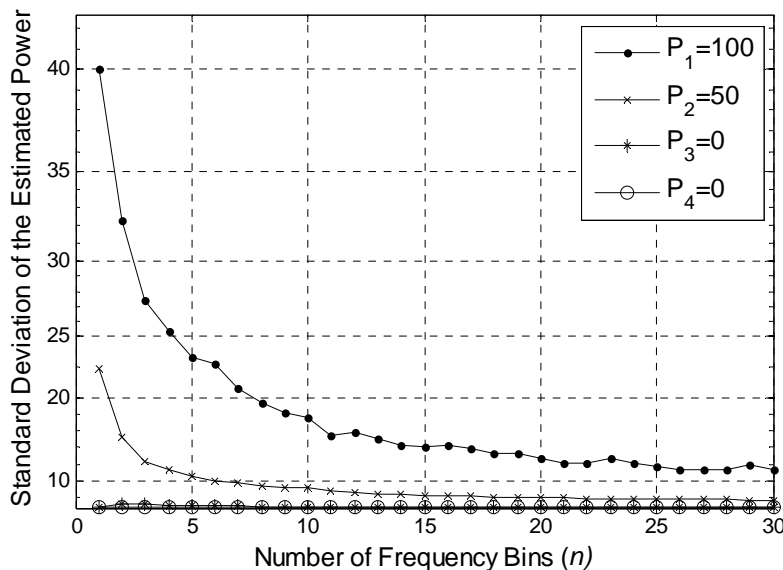


Figure 23: Effect of the number of frequency bins (variance).

2.5.3.2 A Case Study: DSA in Cellular Networks

Detecting spectrum opportunities in the frequencies allocated to cellular networks is a challenging problem due to several issues such as the requirement on pervasive coverage, presence of different services with different quality constraints, dynamic traffic patterns of primary systems, presence of several neighboring primary transmitters and adaptive primary transmit powers. The dynamism of primary traffic is taken into account by using fast and cooperative sensing techniques [41]. In some countries, the locations of cellular base stations can be known by scanning the cities or can be published based on regulatory demand. However, the transmit power can change very fast, especially if fast power control or fast scheduling is applied. Therefore, a reasonable assumption in the case of primary cellular network is to consider that the cognitive radio knows the positions of primary base stations through a local or regional database as it is suggested by FCC [42] without knowing their transmit power. In this subsection we employ the technique presented previously in this chapter in order to detect the activity of primary base stations and use this information to determine the power with which a cognitive radio can transmit known its own position and the positions of primary base stations. This work has been published in [47].

Problem Formulation and Algorithm Description

We consider a set of CR clusters (C-Clusters) deployed in the coverage area of a cellular network as shown in Figure 24. Each C-Cluster c_i is formed by a set S_i of Cognitive Nodes (C-Ns) that act also as sensors. The locations of the C-Ns follow a probability distribution D centered at the center of the cluster. The primary network involves N base stations (P-BSs) that can be either active or idle in a given channel. The activity of these base stations is supposed to be unknown by the secondary network. In particular, the transmit power P_i of an active primary transmitter i is not known. This is realistic assumption since base stations' activity in cellular networks can have very high dynamics that will lead to unacceptable signaling traffic if the activity information is to be communicated to the secondary network in real time.

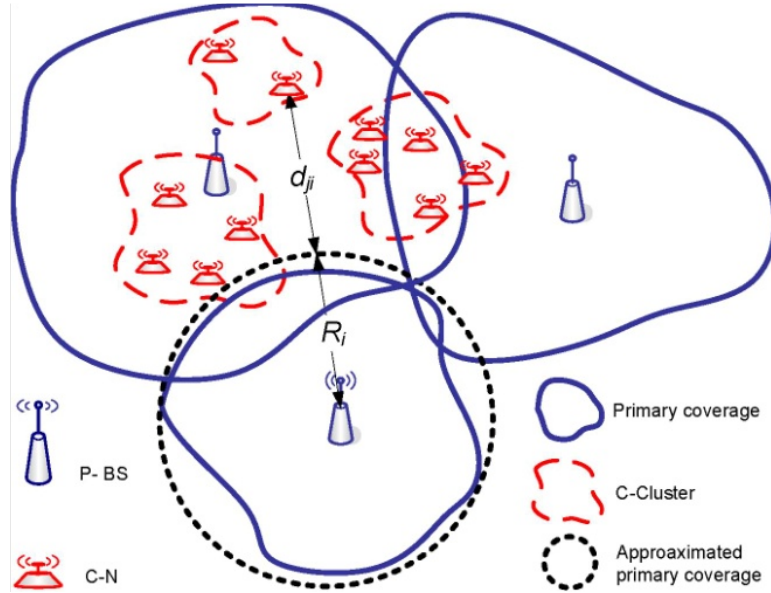


Figure 24: Primary and secondary networks .

Without loss of generality, we consider only one channel used by the primary network in our analysis. In the following we denote by Φ the set of all primary base stations and by Φ_a the set of primary active base stations using the channel of interest. The objective of our proposed DSA approach is to determine the power with which a Cognitive Node (C-N) can transmit based on the measured power on the channel of interest while respecting primary constraint. We assume that the primary constraint is a limit on the probability of interference experienced by any primary receiver i [43],[44]. This constraint is defined by

$$P\{I_i > I_{\max}\} \leq \varepsilon, \quad (1)$$

where I_i is the experience interference by receiver i due to secondary activity, I_{\max} and ε are the interference and interference probability thresholds, respectively, defined by the primary network.

We assume that all C-Ns have access to a central database that distribute the frequencies, and thus only one C-N transmits at a given channel at a given time. This assumption is not very realistic but the determination of the transmit power in a multiple secondary transmitter context is still an open issues and it is out of the scope of this work. By considering this assumption, I_i becomes the result of the transmission of one C-N and can be computed as

$$I_i = P_t^j G_{ji},$$

where P_t^j is the secondary transmit power and G_{ji} is the path gain between nodes i and j given by

$$G_{ji} = \frac{k_{sp}}{d_{ji}^{\alpha_{sp}}} \xi_{ji},$$

where d_{ji} is the distance separating the two nodes, k_{sp} and α_{sp} are propagation constants that depends on the type of the nodes, and $\xi_{ji} : \ln N(0, \sigma_{sp})$ is a log-normally distributed random variable representing the shadowing effect. The allowed transmit power can be written as

$$P_t^j \leq \frac{I_{\max} d_{ji}^{\alpha_{sp}}}{k_{sp}} e^{\sqrt{2}\sigma_{sp} \operatorname{erf}^{-1}(2\varepsilon-1)}.$$

It can be seen that the C-N needs to know its distance toward the closest active primary receiver or at least a lower bound of this distance. If the primary network is active in uplink, d_{ji} can be computed accurately since the position of the receiver (i.e., base station) is known. If the primary network is active in downlink however, only the lower bound of the distance can be estimated since the position of the receiver (i.e., terminal) cannot be known accurately. Therefore we assume that the coverage area of the primary network is known and it is approximated by the disc with radius R_i encompassing the real one. In this case the lower bound is computed as the distance between the transmitting C-N and the closest point inside the disc. Here two cases appear; if the C-N is inside the coverage area, the lower bound become 0 since the primary receiver can be at place inside the coverage area. If the C-N is outside the coverage area, the lower bound is the distance between the C-N and the closest point or worst case position (WCP) at the borders of the covering disc as shown in Figure 25 [44],[45].

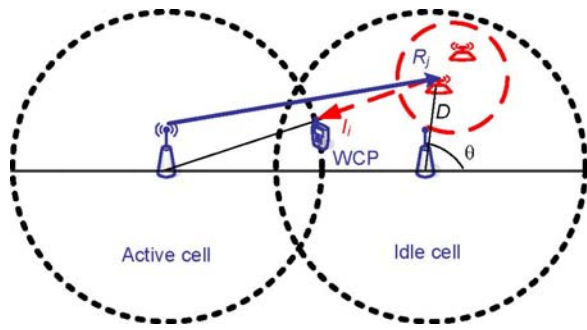


Figure 25: An illustrative example of the model with two cells.

As shown in the previous paragraph, the computation of P_t^j requires the knowledge of the distance to the closest active base station in uplink or closest point in the coverage disc of the closest active cell in downlink. In summary the closest active cell have to be detected.

The main problem in detecting the closest active cell is the presence of multiple simultaneous primary transmitters. In fact, each sensor j receives a power P_r^j , which is the aggregation of the signals received from the active primary base stations (the case of active primary terminals can be also considered)

$$P_r^j = \sum P_t^l G_{lj}$$

where $P_t^l \in \{0\} \cup [P_{\min}, P_{\max}]$ is the transmit power that can be either 0 or between a minimum P_{\min} and maximum P_{\max} specified by the used primary technology and known by the secondary network, and G_{lj} is the path gain between the primary transmitter l and C-T j

$$G_{lj} = \frac{k_{ps}}{d_{lj}^{\alpha_{ps}}} \xi_{lj}.$$

One of the difficulties to detect the active base stations is the presence of the shadowing factor $\xi_{lj} : \ln N(0, \sigma_{ps})$ between the primary transmitters and C-Ts. In the next section we show how we can detect these base stations using the previously established Maximum Likelihood Estimator (MLE) methodology.

In order to detect its closest active cell, all C-Ts in each set S_j communicate the measured received signal to the serving C-BS. The probabilistic description of P_r^j when multiple primary transmitters are active, i.e. P_t^l is non-zero for multiple values of l has been presented earlier in this section. In particular, according to the algorithm, the distribution of P_r^j is assumed represented by the log-normal distribution $\ln N(\mu_j, \beta_j)$ where

$$\mu_j = \ln \left(\sum_{l \in \Phi} \frac{P_t^l}{d_{lj}^{\alpha_{ps}}} \right) + \frac{\sigma_{ps}^2}{2} - \frac{\beta_j}{2}$$

and

$$\beta_j = \ln \left[\left(e^{\frac{\sigma_{ps}^2}{2}} - 1 \right) \frac{\sum_{l \in \Phi} \left(\frac{P_t^l}{d_{lj}^{\alpha_{ps}}} \right)^2}{\left(\sum_{l \in \Phi} \frac{P_t^l}{d_{lj}^{\alpha_{ps}}} \right)^2} + 1 \right]$$

Since we assume that the locations of the base stations are known, these expressions relate the total received power as a log-normal random variable directly to the set of active base stations and their transmit powers. We can therefore apply MLE to estimate the activities of the base stations, and subsequently estimate the allowable transmit power of the secondary node based on the state of the primary network. In the following subsection we apply this technique in order to characterize the maximum allowable secondary power.

Simulation Results

We evaluate our method in a system where the primary network is a cellular network comprising only macrocells served by base stations of 27 m height. These base stations serve mobile terminals with antenna of height 1.5 m . The C-Ns are considered to be IEEE 802.11 access nodes with antenna of height 3 m . In all simulations we consider the downlink of the primary and secondary networks, i.e., the transmitters are the P-Bs and the C-Ns. We use the Xia-Bertoni propagation model [46]. This model is chosen since it can take into account all types of propagation losses such as the one between base stations and the one between mobiles in addition to usual propagation loss between a base station and a mobile. Given a frequency f in GHz and distance d_{xy} between transmitter X and receiver Y , path loss L_{xy} is given by

$$L_{xy}(d_{xy}) = K_{xy} + \beta_{xy} \log_{10}(f) + \alpha_{xy} \log_{10}(d_{xy}),$$

where K_{xy} , β_{xy} and α_{xy} are constants computed using the Xia-Bertoni model. The obtained propagation constants are collected Table 3, where PR stands for primary receiver. We consider a log-normal shadow fading with zero mean and a standard deviation of σ . First, we shall study the performance of the proposed algorithm as function of the number of sensors in a simple scenario with two cells of 1 km radius. For this we consider that $P_{\max} = 27.4\text{ dBm}$ and $P_{\min} = 17.4\text{ dBm}$. Therefore if the secondary determine that the primary transmit power is lower than 17.4 dBm , it will identify the corresponding base station as idle. We use $\sigma = 1.38$ that corresponds to 6 dB unless otherwise stated. Simulations are repeated 200 times in order to obtain statistically significant results.

Table 3: Obtained propagation constants

	α	β	K	σ
C-T P-BS	37.6	21	113.2	[0.69;3.45]
C-T P-R	40	30	141.7	2.3

In the simulations we consider the following three scenarios:

- **Scenario 1:** One base station is active while the second is idle. The sensors are distributed uniformly inside one cell.
- **Scenario 2:** The two base stations are active. The sensors are distributed uniformly inside one cell.
- **Scenario 3:** One base station is active while the second is idle. The sensors are distributed uniformly inside the two cells.

In Figure 26, we show the cumulative distribution function (cdf) of the estimated power of the primary base stations for different numbers of sensors and considering the three scenarios. In scenario 1, the transmit power of the active base station is 24 dBm and the figure shows that with 9 sensors or more this base station is detected to be active in more than 95 %. However, this percentage drops to 60 % in the case only one sensor is in the active cell and to 40 % when the sensor is in the idle cell. This shows the importance of cooperative detection. Moreover it shows that this method can protect the primary receivers if the number of sensors is high enough. Furthermore, the figure shows that the non activity of the idle base stations with high accuracy when the sensors are in the idle cell. Even in the case of this sensor the false detection is less than 5 %. However, when the sensors are in the active cell the false detection increase to 60 % in case we have more than 9 sensors and to more than 95 % in case we have only one sensor. This shows how many opportunities can be lost due to the position of the sensors. This is normal due to the high shadowing standard deviation. For example, a sensor situated at the common boundary of two equally sized cells, with both primary transmitters utilizing same transmit powers, would have to estimate whether one or both transmitters are active based on expected difference in average received power of approximately 3 dB. However, given that the typical standard deviation of the shadowing component is 7 dB or more, we see that the differences in the activation patterns are easily overshadowed by the contributions from shadowing in terms of likelihoods. This effect can be eliminated by distributing the sensors over the the two cells as it shown in the figures representing the scenario 3. Moreover the figures representing the scenario 2 show that the sensors detect the activity of the two cells. However the level of the power of the non covering cell is significantly reduced due to the high separating distance.

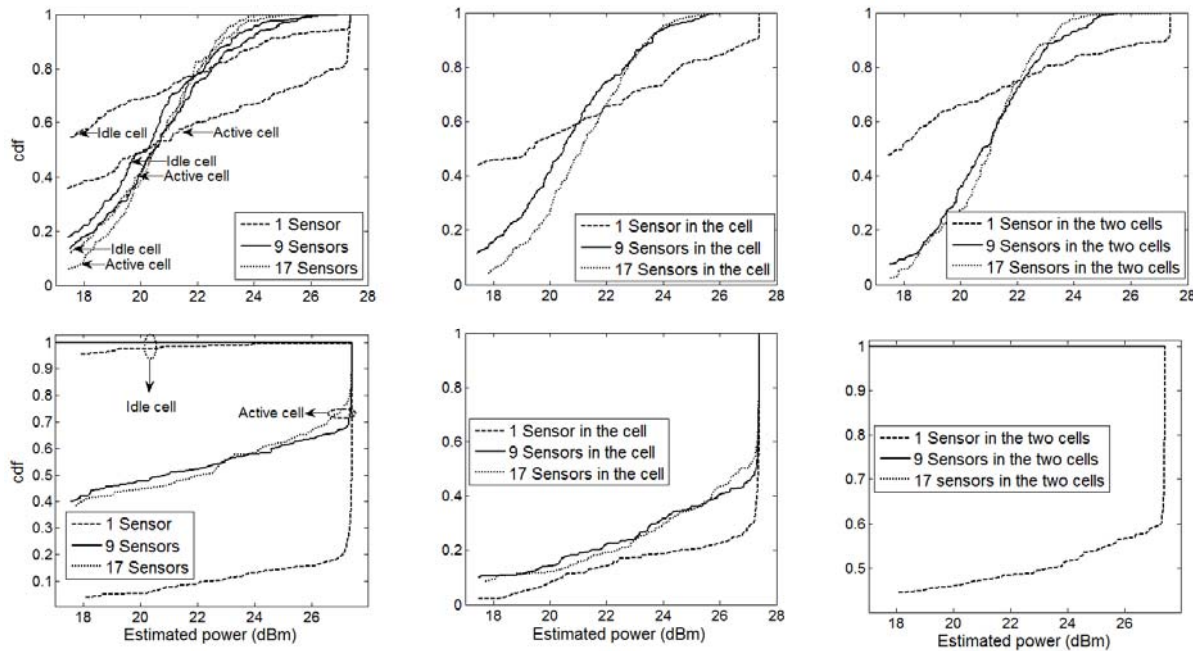


Figure 26: The distribution of the estimated power of primary base stations by secondary network. The first (resp. the second) row reflects the estimated power of the active (resp. idle) cell, while the three columns reflect the three simple scenarios.

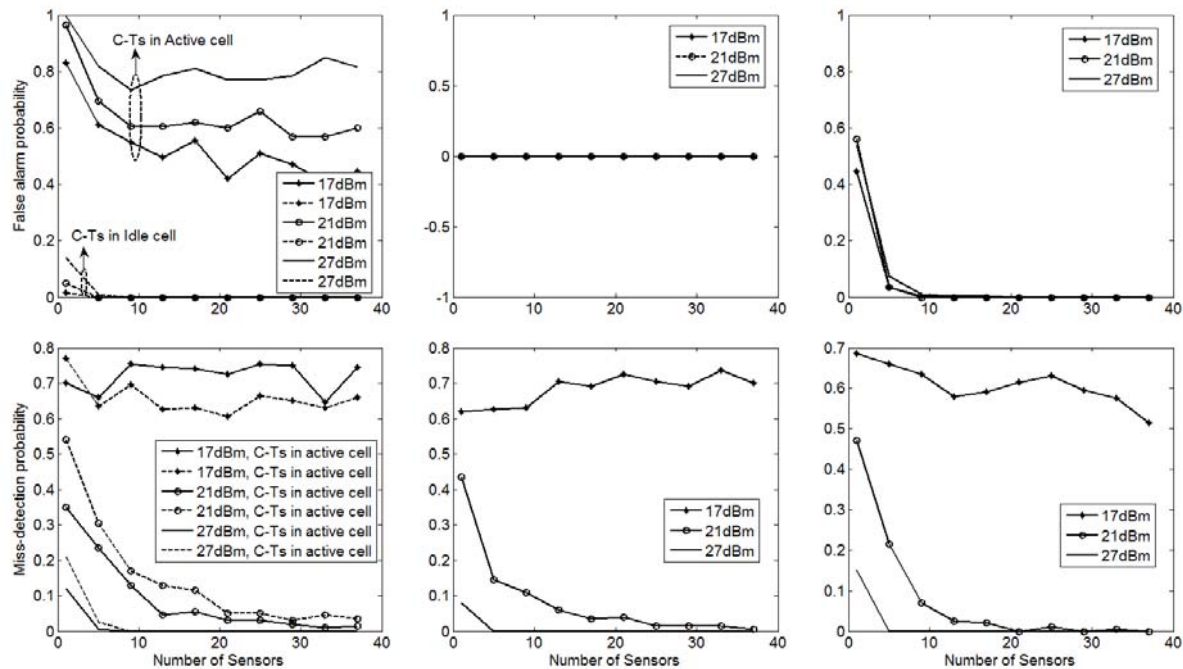


Figure 27: The variation of the false alarm probability (first line) and miss detection probability (second line) as a function of the number of sensors for different transmit power levels of the primary transmission. The three columns reflect the three simple scenarios.

In Figure 27, we show the false alarm probability (i.e, the probability that the idle base station is considered active) and the miss-detection probability (i.e., the probability that the active base station is considered idle). In this figure the effect discussed above is more clear. In addition the impact of the power is shown, where the false alarm is an increasing function whereas the miss detection is a decreasing function of the primary transmit power. This means the higher the latter the more protective will be the algorithm. Moreover, this figure shows that the number of sensors needed to protect the primary (i.e., keep the miss-detection probability lower than a threshold) decreases when the primary transmit power increases but this increase in power will decrease the possibility of detection of the spectrum opportunities. In addition when the power is very low, e.g., 24 dBm , the primary receivers cannot be protected with any number of sensors.

3 Spatial interpolation techniques for RIFE

In this chapter we address the problem of estimating the radio interference field, what was previously defined as RIFE, but now via *direct* methods that exploit spatial interpolation.

3.1 Introduction

Spatial interpolation [50] comprises the essence of the direct method for estimating the RIFE, in contrast to the indirect one examined before. As usual, the architecture assumes the collection at some central processing unit of measurements from a number of spatially distributed sensors (MCDs).. The mathematical problem is to fill out the missing values (received power or interference within a given frequency band) of the radio field in all other points, based on those measured, and do so in ways that minimize some average function the interpolation error (i.e., a function of the difference between what is true and what is estimated).

There is a variety of methods which target spatial interpolation and which have been exploited in different scientific and research areas. All these methods are, in essence, techniques for linear interpolation. In general, all these interpolation methods can be divided into four main groups: (1) local neighborhood approaches, (2) geo-statistical approaches, (3) variational interpolation approaches and (d) compressed sensing.

The first, local neighborhood methods, assumes that each spatial point influences the resulting spatial field only up to a certain distance. The interpolated points are computed by predefined functions that reflect the influence of the neighboring points in the most realistic manner. The most commonly used methods and their variations in the literature are *Inverse Distance Weighted (IDW)* interpolation [51], *Natural Neighbor* interpolation [52], *interpolation based on Triangular Irregular Network (TIN)* [53] etc.

The second, geo-statistical interpolation, extends beyond basic interpolation and relies on statistical models based on random functions and variables to model the uncertainty associated with the spatial estimation and interpolation process. The most widely used geostatistical interpolation technique is based on the *Kriging* method and its variations [50].

The variational interpolation approach is based on the assumption that the interpolation function should have very small deviations from the known positions of the measurements (received data points), while tending to be as smooth as possible in the remainder of the field. These two requirements are combined into a single condition that represents a proper *spline* function, namely the one that defines the specific the interpolation method. The *Thin Plate Spline (TPS)* and its variations [54],[55] are the most widely used methods in this variational interpolation approach.

Compressive sensing [56] is a new type of sampling theory, which predicts that sparse signals and images can be reconstructed from what was previously believed to be incomplete information. As a main feature, efficient algorithms such as ℓ_1 -minimization can be used for recovery. The theory

has many potential applications in signal processing and imaging. In this chapter, it will be shown how to employ compressed sensing for the RIFE application.

A unified framework to view all the above methods could be a linear interpolation framework: in particular, linear methods that estimate the value of an unknown function based on measurements on known other points in space are modeled as

$$\hat{f}(x^*) = \sum_{i=1}^n \lambda_i(x^*) f(x_i)$$

Where x^* is the point where we seek to interpolate, x_i are the given values of the function. Here n can be the total number of nodes where the value of the function is given, or some appropriately chosen neighborhood around point i (in fact then n is a function of x^* , ie. $n(x^*)$). The weights λ_i are solutions of a system of equations which is obtained by assuming that f is a sample-path of random process $F(x)$, and that the error of prediction

$$e(x) = F(x) - \sum_{i=1}^n \lambda_i(x^*) F(x_i)$$

is to be minimized in some sense. For instance, the squared value of $e(x)$ can be minimized (least-squares) estimation and this refers to the classical Kriging approaches. In general, other functions of $e(x)$ can be minimized and yield the required estimator. In 3.2.4 a combination of $|e(x)|$ and $e^2(x)$ is used as criterion. In 3.2.2 and 3.2.3 the λ_i are so that data is weighted during interpolation, so that the influence of one point relative to another declines with distance from the grid node. Typically a weighting power is used in order to determine the speed weighting factors drop off as distance from the grid node increases.

This section presents the analysis and comparisons of four different algorithms, all of which derive from the four aforementioned approaches. The interpolation techniques of interest are:

- In Sections 3.2.1.1 and 3.2.1.2, techniques are based on the ordinary Kriging interpolation [50], which is a geostatistical interpolation method based on spatial statistics;
- In 3.2.2, the technique is based on the IDW modified Shepard's method (MSM) [51], a local-neighborhood-based method, which is a significant improvement of the original IDW method;
- In 3.2.3, the technique is based on the Gradient-plus-Inverse-Distance-Squared (GIDS) method [57], a local-neighborhood method that combines Multiple-Linear Regression (MLR) with IDW interpolation.
- The technique in 3.2.4 is based on compressed sensing.

3.2 Description of proposed techniques

3.2.1 The Kriging interpolation

The Kriging interpolation uses the spatial statistics as a base for estimation of the missing spatial data. Specifically, the Kriging method uses semivariograms to estimate the radio field, which requires stationarity of the measurement data in order to obtain a consistent estimation. In this sense, the Kriging estimator relies on intrinsically stationary random fields. The semivariogram can be generally seen as a measure of the statistical dependence between two location points. It can be empirically estimated from the spatially distributed measurement data, but, due to the conditionally negative-definite requirement for the semivariogram function, the empirical data is generally fitted into an existing parametric semivariogram model.

There are two broad classes of fitting techniques mainly used for estimation of the parameters of the semivariogram model: Maximum Likelihood (ML) based and Least-Squares (LS) based. There also exist various theoretical semivariogram models such as Spherical, Gaussian, Exponential, Power etc.

3.2.1.1 Isotropic Matern Kriging technique

The selection of the target semivariogram model has a major impact on the Kriging interpolation performance. The analysis in this subsection considers the isotropic Matern model [58] as the chosen semivariogram model, specified by the following formula:

$$\gamma(h) = \tau^2 + \sigma^2 \left(1 - \frac{1}{2^{\kappa}\Gamma(\kappa)} \left(\frac{h}{\phi}\right)^{\kappa} K_{\kappa}\left(\frac{h}{\phi}\right)\right) \quad (3.1)$$

Here, Γ represents the gamma-function, K_{κ} is the modified Bessel function of the second kind and the terms $\tau^2, \sigma^2, \phi, \kappa$ need to be estimated by ML or LS based fitting technique, as previously mentioned. This model is based on the isotropic hypothesis that the semivariogram depends only on Euclidean distance between the points. We henceforth denote this technique as the ordinary Kriging method.

The semivariogram model with the empirically estimated and fitted parameters is further used in the estimation of the neighboring weights $\lambda_i, i = 1, \dots, n$. The basic idea is to generate an optimal linear unbiased estimator of the unobserved values of the random field. The estimator is optimal in the mean squared error (MSE) sense. Furthermore, the Kriging interpolant satisfies the un-biasness condition, i.e., it yields a zero-mean residual error. Finally, the interpolant is linear because it estimates the missing values with weighted linear combination of the available neighboring values. The weights are chosen to satisfy the optimality condition and their values are calculated using the fitted semivariogram of the random field, i.e., the constrained linear optimization can be expressed in terms of the function L :

$$L = E(P_r^k - \sum_{i=1}^n \lambda_i P_r^i)^2 - 2m(\sum_{i=1}^n \lambda_i - 1) \quad (3.2)$$

where P_r^i represents the value at location i , P_r^k represents the value at the target point k and $2m$ is the Lagrange parameter. Solving the Lagrange optimization problem in terms of all neighboring weights and the Lagrange parameter requires the fitted semivariogram model, i.e. the semivariances depending on the distance to the target estimation point. After the neighboring weights are calculated, the estimation about the interpolated value at the location k is

$$\hat{P}_r^k = \sum_{i=1}^n \lambda_i P_r^i \quad (3.3)$$

There are a number of different Kriging interpolants that differ in the assumptions made about the mean or trend of the random field [50]. Simple Kriging assumes that the mean of the field is known and constant in value. Ordinary Kriging assumes that the mean is constant but unknown. Universal Kriging assumes non-constant mean that can be represented as a linear combination of known functions. Our proposed technique is based on Ordinary Kriging only.

3.2.1.2 A Gaussian-based Bayesian technique

The proposed method is based on a Gaussian model for the underlying radio field, and the propagation (path loss) prediction is performed using a Bayesian framework. For reasons of simplicity only a single transmitter source is assumed, but the approach can be generalized to multiple sources as long as the RF measurements can be performed *per source*, i.e., source separation (through decoding) can be performed at the sensors/measurement devices.

We use the following parametric propagation model:

$$P_r^i = P_t - 10\alpha \log_{10}(d_i) + s_i + z_i$$

where P_r^i is the received power at the i^{th} sensor, P_t is the source transmit power, α is the usual path-loss coefficient, d_i is the distance between the source and the i^{th} sensor, s_i is the log-normal shadowing between the source and the i^{th} sensor, and z_i is the AWGN noise.

The main task is to predict the propagation path loss by fitting the model parameters to measurements. In order to achieve this task, we adopt a Kriging approach. Considering N sensors, we can write the received powers at those N sensors in vector-matrix form as follows:

$$P_r \equiv \mathcal{N} \left(X\beta, \frac{1}{\theta} (R(\phi) + \tau I) \right) \quad (3.4)$$

Here P_r denotes the received power vector at the sensors

$$X = \begin{pmatrix} 1 & 10\log_{10}(d_1) \\ & \vdots \\ 1 & 10\log_{10}(d_N) \end{pmatrix},$$

$$\beta = \begin{pmatrix} P_t \\ \alpha \end{pmatrix},$$

Also, $\frac{1}{\theta}$ is the variance of the shadowing and $R(\phi)$ is the correlation matrix with ϕ as the shadowing correlation distance. Furthermore, τ is the white noise variance multiplied by θ .

We assume that the correlation distance of the shadowing is exponentially decaying with the distance:

$$r_{ij} = \frac{1}{\theta} \exp\left(-\frac{d_{ij}}{\phi}\right)$$

where r_{ij} denotes the shadowing correlation and d_{ij} represents the Euclidean distance between two locations indexed by i and j .

In this model, the parameters β , θ , ϕ and τ are unknown. However, we do have some prior information on what their values might be. For instance, we know that the radiated power must be something around the power at the feeder, α is about 3.5 in urban areas and $\sqrt{\frac{1}{\theta}}$ typically ranges between 8 and 11 dB for typical outdoor “Above-RoofTop-to-Below-RoofTop” scenarios. It is tempting to include those prior information bits into the model, so we will go for a Bayesian approach and, for convenience in the derivation, we use conjugate priors when possible, parameters of which will be carefully chosen in order to reflect the prior information:

$$p(\boldsymbol{\beta}, \theta) = (2\pi)^{-\frac{\mu}{2}} |H|^{\frac{1}{2}} \theta^{\frac{\mu}{2}} \exp\left[-\frac{\theta}{2} (\boldsymbol{\beta} - \mathbf{b})^T H (\boldsymbol{\beta} - \mathbf{b})\right] \left(\frac{\nu q}{2}\right)^{\frac{\nu}{2}} \Gamma^{-1}\left(\frac{\nu}{2}\right) \theta^{\frac{\nu}{2}-1} \exp\left[-\frac{\theta}{2} \nu q\right] \quad (3.5)$$

where $\boldsymbol{\beta}$ is multivariate discrete and \mathbf{b} is discrete.

The computation of marginal distributions involved in this problem (related to the above prior) are presented in the Appendix. In particular, since (3.43) and (3.44) are weighted sums of pdfs, the expected value of the formers are weighted averages of the expected values of the latters and we therefore derive:

$$\mathbb{E}_{|\mathbf{y}}(\theta) = \sum_{\phi_k, \tau_k} p(\phi_k, \tau_k | \mathbf{y}) \frac{1}{q''(\phi_k, \tau_k)} \quad (3.6)$$

$$\mathbb{E}_{|\mathbf{y}}(\boldsymbol{\beta}) = \sum_{\phi_k, \tau_k} p(\phi_k, \tau_k | \mathbf{y}) \mathbf{b}''(\phi_k, \tau_k) \quad (3.7)$$

Any estimator is a function of measurements which properly minimizes any given cost function. We choose the minimization of the quadratic risk:

$$\hat{\mathbf{y}}_1 = \min_{\mathbf{y}_1^*} \left(\mathbb{E}_{|\mathbf{y}}((\mathbf{y}_1 - \mathbf{y}_1^*)^T (\mathbf{y}_1 - \mathbf{y}_1^*)) \right) \quad (3.8)$$

$$= \mathbb{E}_{|\mathbf{y}}(\mathbf{y}_1) \quad (3.9)$$

We can also calculate the mean squared error:

$$MSE = \frac{1}{n_1} \mathbb{E}_{|\mathbf{y}}[(\mathbf{y}_1 - \hat{\mathbf{y}}_1)^T (\mathbf{y}_1 - \hat{\mathbf{y}}_1)] \quad (3.10)$$

$$= \frac{1}{n_1} \mathbb{E}_{|\mathbf{y}} [(\mathbf{y}_1 - \mathbb{E}_{|\mathbf{y}}(\mathbf{y}_1))^T (\mathbf{y}_1 - \mathbb{E}_{|\mathbf{y}}(\mathbf{y}_1))] \quad (3.11)$$

$$= \frac{1}{n_1} \text{trace}(\text{cov}_{|\mathbf{y}}(\mathbf{y}_1)) \quad (3.12)$$

Hence the distribution (or at least the moments) $p(\mathbf{y}_1|\mathbf{y})$ is required. Its computation is presented in the Appendix.

Then if we use discrete prior for $p(\phi, \tau|\mathbf{y})$ as presented in the Appendix we can compute the resulting mean and covariance as follows:

$$\mathbb{E}_{|\mathbf{y}}(\mathbf{y}_1) = \sum_{\phi, \tau} p(\phi, \tau|\mathbf{y}) \mathbb{E}_{\phi, \tau, \mathbf{y}}(\mathbf{y}_1) \quad (3.13)$$

$$\text{cov}_{|\mathbf{y}}(\mathbf{y}_1) = \sum_{\phi, \tau} p(\phi, \tau|\mathbf{y}) \left[\text{cov}_{\phi, \tau, \mathbf{y}}(\mathbf{y}_1) + (\mathbb{E}_{\phi, \tau, \mathbf{y}}(\mathbf{y}_1) - \mathbb{E}_{|\mathbf{y}}(\mathbf{y}_1)) (\mathbb{E}_{\phi, \tau, \mathbf{y}}(\mathbf{y}_1) - \mathbb{E}_{|\mathbf{y}}(\mathbf{y}_1))^T \right] \quad (3.14)$$

This can be used for interpolation purposes, taking \mathbf{y}_1 as the measurements at every point on the grid. The shadowing only is given by:

$$\mathbb{E}_{|\mathbf{y}}(\mathbf{s}_1) = \mathbb{E}_{|\mathbf{y}}(\mathbf{y}_1) - X_1 \mathbb{E}_{|\mathbf{y}}(\mathbf{\beta}) = \mathbb{E}_{|\mathbf{y}}(\mathbf{y}_1) - X_1 \mathbf{b}''$$

3.2.2 Inverse Distance Weighting modified Shepard's interpolation

The IDW-based modified Shepard's method [51] takes a different approach for the estimation of the missing radio field data. Specifically, the MSM is a local interpolant that makes no assumptions about the nature of the radio field and makes the estimation based on multivariate functions called *nodal functions*. This is the main enhancement compared to the original IDW Shepard's method. The MSM interpolant defines a local real multivariate function for each observed point, obtained as a result of weighted LS fitting on a set of its N_q nearest neighbors. These nodal functions can take different analytical forms (may be quadratic, linear, constant etc.) and the appropriate form can be selected for different environment surroundings (emulating the correlation characteristics). These functions' parameters are estimated based on weighted LS approach, i.e., the nodal function Q_k for the observed point k with coordinates (x_k, y_k) , is calculated by minimizing the following expression:

$$S = \sum_{i=1}^{N_q} \omega_{ik} [Q_k(i) - P_r^i]^2 \quad (3.15)$$

where P_r^i is the observed value at neighboring point i , $Q_k(i)$ is the value of the nodal function Q_k in at neighboring point i with coordinates (x_i, y_i) , while ω_{ik} is the considered weight to the point i calculated with the following equation:

$$\omega_{ik} = \begin{cases} [(R_q - d_{ik})/R_q d_{ik}]^2, & \text{if } d_{ik} < R_q \\ 0, & \text{otherwise} \end{cases} \quad (3.16)$$

Here, the term d_{ik} represents the distance from the point k to the point i and R_q is a radius of influence of the observation at point i . Only the nodes whose radii of influence include the location point k have nonzero contribution to the LS fit.

Besides the nodal functions' parameters, the MSM IDW method requires the calculation of the relative weights defined by the inverse distance formula

$$W_{kl} = \begin{cases} [(R_w - d_{kl})/R_w d_{kl}]^2, & \text{if } d_{kl} < R_w \\ 0, & \text{otherwise} \end{cases} \quad (3.17)$$

where d_{kl} denotes the Euclidean distance between location points l and k , with coordinates (x_l, y_l) and (x_k, y_k) , respectively, and R_w is a radius of influence of the observation at point k . The value at this point only influences interpolated values at points within the radius R_w .

Based on the relative weights and the nodal functions the interpolated values are calculated based on the following formula:

$$\hat{P}_r^l = \frac{\sum_{k=1}^{N_w} W_{kl} Q_k(l)}{\sum_{k=1}^{N_w} W_{kl}} \quad (3.18)$$

The radii of influence R_w and R_q can be fixed [59] or can vary with k . In fact, the interpolation method proposed in [51] consists of choosing R_w and R_q large enough to include N_w and N_q observations, respectively. These parameters are of high importance for the performance of the interpolant and they can be chosen in appropriate manner to reflect the nature of the propagation channel.

3.2.3 Gradient plus Inverse Distance Squared interpolation

The GIDS interpolation method [57] combines MLR technique with IDW interpolation. Similarly to the MSM interpolant, the GIDS interpolation improves the classical IDW interpolation by introducing the usage of multivariate real functions. This technique introduces the mandatory presence of the elevation of the observed values above the reference plane. However, in terms of REMs, the introduction of the elevation is required only when the measurements are performed on different heights. Otherwise, it will only increase the computational cost without improving the fidelity of the overall technique. The elevation can also be introduced in the previous interpolation method, for achieving higher precision, sacrificing the computational and memory cost.

For given unobserved location point k with coordinates (x_k, y_k, z_k) , an ordinary least squares (OLS) regression is performed using n closest neighboring locations to calculate coefficients C_x , C_y and C_z representing the x , y and z (or elevation) gradients:

$$P_r^i = a + C_x x_i + C_y y_i + C_z z_i + \varepsilon_i \quad (3.19)$$

where a is the intercept, ε_i is the random residual and $i = 1, \dots, n$. Thus, the basic GIDS formula is:

$$\hat{P}_r^k = \frac{\sum_{i=1}^n (P_r^i + C_x(x_k - x_i) + C_y(y_k - y_i) + C_z(z_k - z_i)) / d_i^2}{1/d_i^2} \quad (3.20)$$

where \hat{P}_r^k is the predicted value at unobserved location point k , P_r^i is the value obtained by measuring at location i with coordinates (x_i, y_i, z_i) and d_i is the Euclidean distance from location i to location k .

3.2.4 Compressed Sensing Techniques

In this section we will be inspired by references [31] and [48] and cast the field estimation problem in the form of a reconstruction problem, which we will solve via techniques proposed in the recent body of work named “compressed sensing”. In Section 3.3.3 we assess the performance of these methods with the metrics described therein.

A generic model for the aggregated received power in a location j is:

$$P_r(j) = \sum_t G_{rt} d_{rt}^{-\alpha} P_t + \sigma_r^2 \quad (3.21)$$

Two aspects of this model account for today's challenges associated with solving for or estimating the above unknowns from sensor observations the (typically unknown) shadow fading and the plurality of the transmitters. As a start we will focus on the latter and ignore the shadow fading. While this may seem too much of a simplifying assumption, we will see that even for this simple model, determining the radio field is a challenge. Our model of interest is

$$P_r(j) = \sum_t d_{rt}^{-\alpha} P_t(i) \quad (3.22)$$

At this point the model is not statistical anymore (any stochastic quantities have been ignored) and what is left is a deterministic model. The approach we will be following in this section is the one of a *reconstruction* problem. We will assume that we observe *samples* of the radio field and investigate to what extent we can reconstruct the field from these samples. In particular we will be interested in the number and the nature of these samples, how many samples do we need for proper reconstruction and under which conditions can these samples be captured.

Let us focus our attention on a region of interest and let us represent this region with a *grid*, a set of grid-points, each grid-point indicating a possible physical location in the region (just as was done in Section 2.5). For instance, we can define this grid as the set of grid-points (x, y) , where x is the longitudinal coordinate and y (in degrees) is the latitudinal coordinate (in degrees) in the region. Figure 1 illustrates this concept. We will choose the density of the grid (the distance between grid-points) in accordance with the spatial resolution we require our resulting REM to have. For instance, in a residential area, a grid resolution in the order of 1-10 meters will be suitable. We will assume that there are N grid-points in our grid and we will label these points with indices $n=1, \dots, N$.

We will be interested in the identification of any radio transmitters operating in the region. In particular, a radio transmitter located in gridpoint i will emit power with $P_t(i)$ and cause a radio field that can be sensed with appropriately tuned radio receivers, the sensors. A radio sensor located in another gridpoint, j , measures the radio field in terms of received power, $P_r(j)$. Figure 28 illustrates example positions of transmitters and sensors in the grid.

We rewrite (3.24) as

$$P_r(j) = \Psi_{ij} P_t(i) \quad \text{where } \Psi_{ij} = d^{-\alpha} \quad (3.23)$$

denotes how the received power $P_r(j)$ in gridpoint j is related to the transmitted power $P_t(i)$ in gridpoint i , and where α is, as before, a known pathloss exponent and d is the (Euclidean) distance between gridpoint i and gridpoint j . Allowing each gridpoint to contain both a transmitter and a sensor, the power transfer (3.25) turns into a matrix/vector equation

$$\mathbf{p}_r = \Psi \mathbf{p}_t, \quad (3.24)$$

where \mathbf{p}_t is the $N \times 1$ vector of transmitted powers, \mathbf{p}_r is the $N \times 1$ vector of received powers and Ψ is the channel power transfer matrix

$$\Psi = [\Psi_{ij}] \quad (3.25)$$

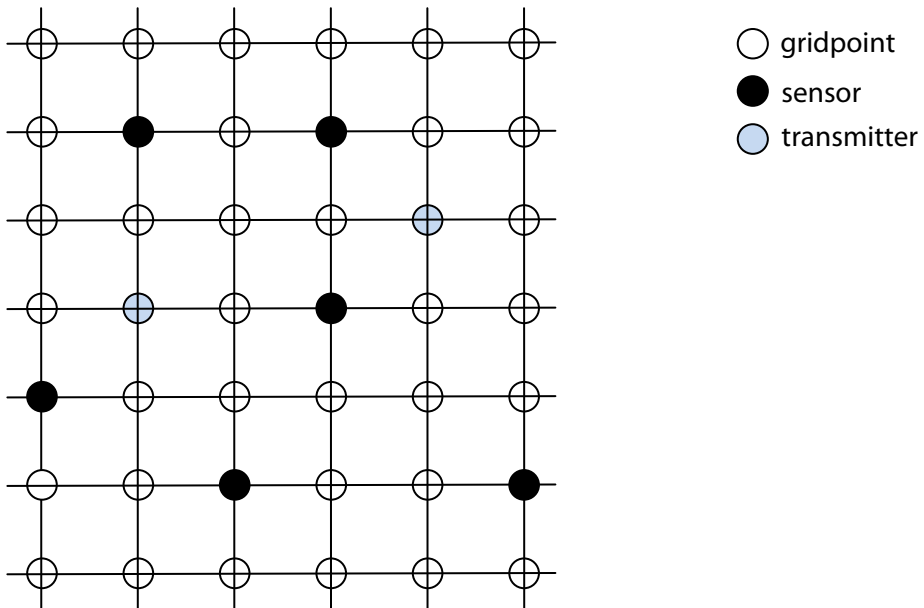


Figure 28: Example of a grid along with transmitter and sensor positions.

For decades, engineers have primarily been using sampling theory based on the assumption that the underlying signal is *band-limited* (possibly after the use of anti-aliasing filters) and, with some noticeable exceptions, that the sampling instants are regularly spaced. Not until recently, a whole body of work has been emerging for signals that satisfy another condition: rather than band-limited the signal is assumed to be *sparse*.

A signal \mathbf{y} is usually assumed to be " k -sparse", indicating that at most k samples (entries) of \mathbf{y} have a non-zero value. Alternatively, \mathbf{y} is a linear transformation of a k -sparse vector \mathbf{x} , that is, $\mathbf{y} = \Psi \mathbf{x}$, for some linear transformation Ψ . (The sampled signal \mathbf{y} is either k -sparse itself or it is the linear transformation of a k -sparse signal \mathbf{x}).

This sparsity matches the physical reality of our above problem. Typically there are only few transmitters actively transmitting (relative to the grid size N), that is, only few entries of the power vector \mathbf{p}_t are non-zero. This motivates the exploitation and investigation of the mentioned recent advances in compressed sensing.

In "compressed sensing" (also called "compressive sensing" or "compressed sampling"), the terminology "samples" ("measurements") of \mathbf{y} relates to the *linear projections* of a vector \mathbf{y} onto base vectors Φ_m . Collection of M such projections (introducing the matrix whose M rows are the M projection vectors Φ_m) then produces the measurement vector

$$\mathbf{z} = \Phi \mathbf{y}. \quad (3.26)$$

Applied to our signal model, the observed samples are then

$$\mathbf{z} = \Phi \Psi \mathbf{p}_t, \quad (3.27)$$

where Φ is an $M \times N$ measurement matrix. As a final step, in order to complete the formulation of the radio field estimation problem as a compressive sensing problem, we now have to specify the measurement matrix Φ . We will consider three categories:

1. A first choice of the measurement matrix is based on the physical fact that sensors sample the radio field in one particular location. We will denote these sensors as *static sensors* and the measurement matrix Φ associated with this choice has each of its rows contain one single non-zero entry in the particular column whose index is associated with the gridpoint where this sensor is located. All other entries are zero. In other words, the projection vectors are trivial unit vectors.
2. We also investigate a second choice of the measurement matrix associated with what we will refer to as *ideal compressing sensors*. The rows of this measurement matrix (projection vectors) contain spatial signatures (entries take values from $\{-1, 1\}$). Obviously, this choice has little realistic roots (sensors typically have no access to the field power in all grid points), but this type of ideal sensors will be indicative of the limits of this approach.
3. Finally we investigate a third category of *mobile sensors*. Exploiting our assumption that the unknown transmitters do not move and do not change their powers in time, hence the radio field is static in time, we will allow sensors to sample the radio field in different locations *at different time instants*. While moving across the region of interest, mobile sensors can sense the field in various locations and then apply the projection of these measurements onto a compressing vector, a row in Φ , whose entries are zero except for

those locations at which the mobile sensor has been sensing the field. These locations are compressed with a short signature sequence.

Now we need to distinguish between a measurement and a sample. One mobile sensor produces a series of field *measurements* in various locations as it moves from one point in the grid to another. By projecting these measurements onto a row in Φ , it then generates one *sample*, an entry of the observation vector \mathbf{z} .

The main questions we will be concerned with are: how many samples (mobile sensors) are needed and how many measurements do mobile sensors have to collect in order to satisfactorily reconstruct the entire radio field?

The problem posed is: can we reconstruct \mathbf{p}_t from the measurements \mathbf{z} ? For a small-size \mathbf{z} this is a typical under-determined system of equations and many solutions that fit the measurements exist. Spinal instinct solutions choose the minimum energy solution among all feasible solutions, by solving

$$\min \|\mathbf{p}_t\|_2 \text{ subject to } \mathbf{z} = \Phi \Psi \mathbf{p}_t, \quad (3.28)$$

However, this solution does not exploit the prior knowledge of sparsity. With this knowledge, the solution

$$\min \|\mathbf{p}_t\|_0 \text{ subject to } \mathbf{z} = \Phi \Psi \mathbf{p}_t, \quad (3.29)$$

where $\|\mathbf{x}\|_0$ = "the number of non-zero entries in \mathbf{p}_t " (the sparsest solution explaining the measurements), would be a more suitable choice. While (3.28) comes with the disadvantage that the solution typically is not sparse, (3.29) has the disadvantage of high complexity. The theory of compressed sensing has at the core of its proven results that solutions to

$$\min \|\mathbf{p}_t\|_1 \text{ subject to } \mathbf{z} = \Phi \Psi \mathbf{p}_t, \quad (3.30)$$

(where $\|\mathbf{x}\|_1 = \sum_i |x_i|$), under specific conditions for the matrices Φ and Ψ , are also solutions to,

and hence can be used to perfectly reconstruct \mathbf{p}_t from the limited number of measurements in \mathbf{z} , in a reasonably low-complexity fashion. One such solution (known as *basis pursuit*) is based on recasting (3.30) as a linear program and then using the standard primal-dual algorithm for linear programming (whose solution procedure is based on the classical Newton method), see Chapter 2 in [49]. In Section 3.2.4 we investigate how this solution algorithm applies to and performs in the chosen example herein.

3.3 Performance assessment

The aim of this chapter is to investigate the performance of the previously described methods. We therefore present early numerical results from simulations in a variety of practically interesting scenarios.

3.3.1 Indoor (WLAN) and Outdoor (GSM) scenario investigation

This subsection gives a performance evaluation of the previously explained interpolation methods in simulated indoor and outdoor environments. The results are obtained in MATLAB [60], for the MSM and the GIDS method, and the R Random Fields package [61] for the ordinary Kriging interpolation method. The analysis targets two types of scenarios in terms of the sensor positioning, i.e. a scenario with *grid positions* and a scenario with *uniformly scattered* measurement positions. The comparison of the interpolation techniques is made in terms of the Relative Mean Absolute Error (RMAE) metric calculated as:

$$RMAE = \frac{1}{N} \sum_{i=1}^N \frac{|\hat{P}_r^i - P_r^i|}{P_r^i} \quad (3.31)$$

The indoor performance evaluation is conveyed using a simulated 2.4 GHz WLAN scenario. The emulated propagation characteristics comprise multiwall propagation model combined with log-normal shadowing with a variance of 8 dB. The tested simulation area is 36mx36m. Figure 29 shows a plot of the generated signal distribution.

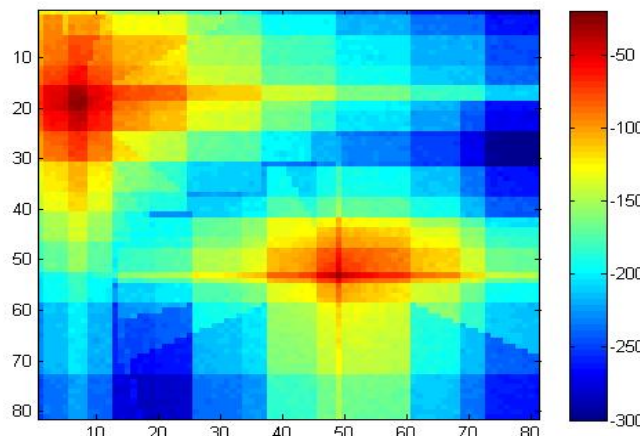


Figure 29: Simulated WLAN environment.

The outdoor performance evaluation focuses on a GSM system simulated with the Okumura-Hata propagation model and lognormal shadowing. The simulation area is 4.3kmx4.3km wide, and the working frequency is selected to be 915 MHz. Figure 30 plots the generated radio signal field.

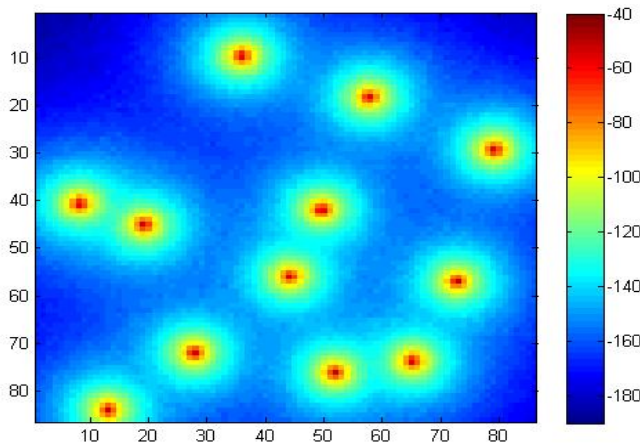


Figure 30: Simulated GSM environment.

The performance evaluations comprised a total of 30 simulated scenarios, i.e. 15 for each of the systems of interest. Six of these apply the regular sampling scheme (generating grids with varying number of observations), whereas the remaining 9 apply the random sampling scheme (generating maps with varying number of scattered observations).

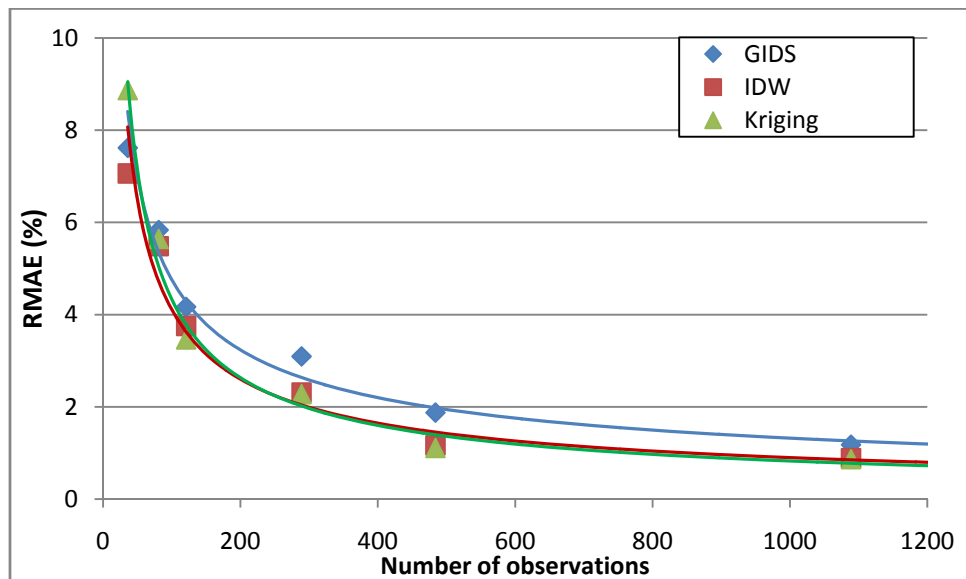


Figure 31: RMAE(%) vs. number of gridded observations for the simulated GSM scenario.

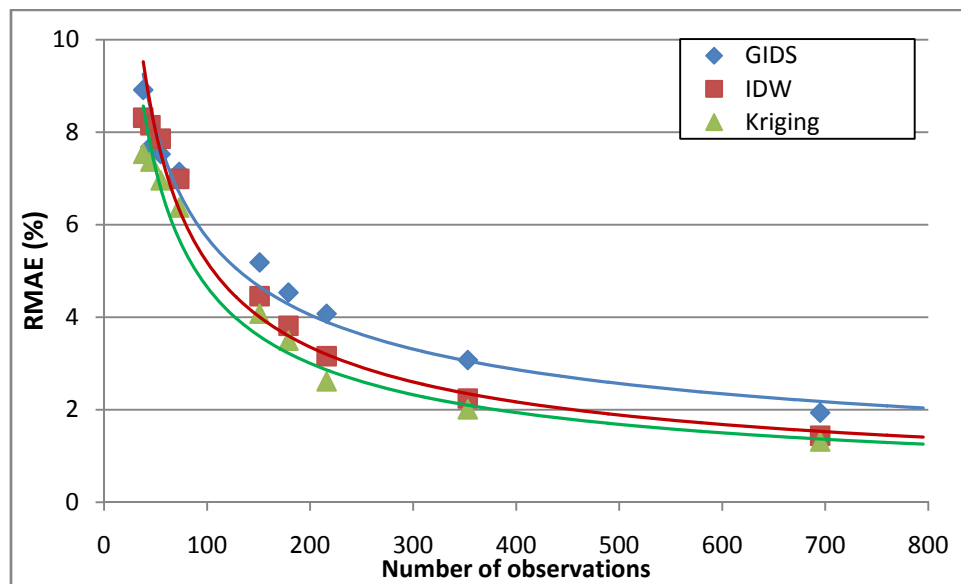


Figure 32: RMAE(%) vs. number of scattered observations for the simulated GSM scenario.

Figure 31 and Figure 32 depict the RMAE results with the elaborated interpolation methods, for the regular and irregular sampled GSM radio field maps, respectively. Figure 33 and Figure 34 plot the RMAE results for the WLAN radio maps. It is clear that the interpolation error decreases as the number of observations increases. Furthermore, the regular positioning of the sensors can produce better interpolation results in general for both inspected scenarios.

The comparison between the WLAN and the GSM scenarios shows a better interpolation performance in the outdoor environment. The outdoor environment model tends to produce higher correlation between two different observation points, which results in more predictable propagation properties, unlike the indoor propagation environment which often produces more uncorrelated measurements. Thus, interpolation in indoor scenarios results in higher prediction errors in general. In terms of the sampling, the results from both scenarios prove that the regular grid produces better interpolation performances than the scattered observations in general.

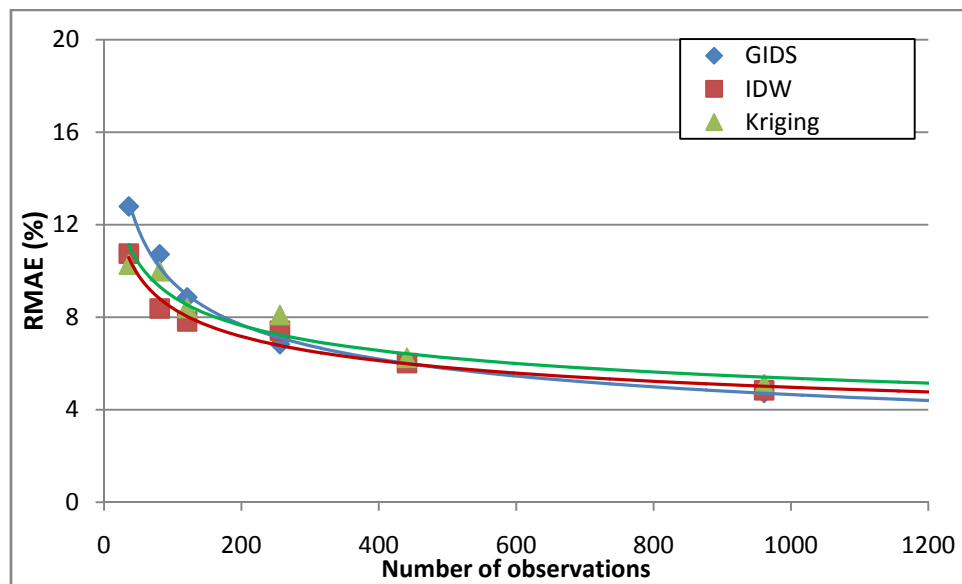


Figure 33: RMAE(%) vs. number of gridded observations for the simulated WLAN scenario.

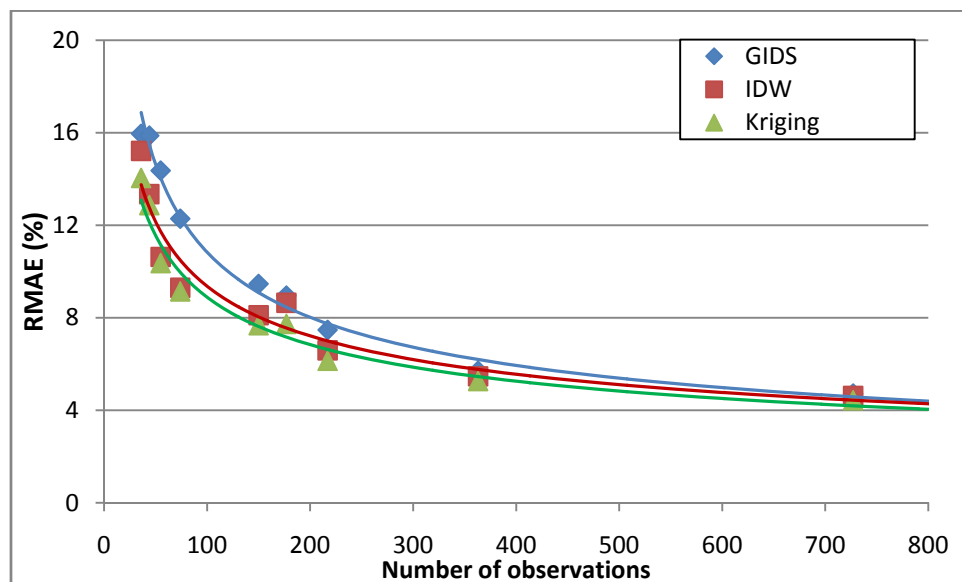


Figure 34: RMAE(%) vs. number of scattered observations for the simulated WLAN scenario.

The comparisons between the different interpolation methods prove that the GIDS interpolation results in significantly lower interpolation performances than the other two approaches. However, it is also the least flexible interpolation method because it has a small number of variable parameters. Besides the number of closest neighbors, which is determined a priori, and the three gradients, which are obtained by OLS regression, there are no available options for accuracy improvement. One possible improvement can be achieved by applying a Generalized or Weighted

Least Squares or even more advanced weights calculation methods. GIDS is also more computationally intense than IDW, because the LS fitting is performed for every interpolation point while IDW performs LS fitting only on the observations.

The IDW MSM interpolation is the second best interpolation method for both tested scenarios. It achieves better performances than the ordinary Kriging interpolation method in several test cases, i.e., when performing gridded observations. This is due to the major improvement of the MSM over the classical IDW method, the using of variable radii of influence and the usage of nodal functions emulating the propagation phenomena. Because of its highly parametric formulation, trade-off between its accuracy and computational cost is possible. Lowering the number of parameters used or choosing simpler fitting technique will decrease the processing time sacrificing the fidelity and vice versa. The simulations have proven that N_q influences the accuracy much more than N_w . This can be interpreted as a significant drawback of IDW compared to GIDS or Kriging, i.e. the number of closest neighbors used for the WLS fitting generally needs to be high in order to obtain good results.

The results prove that the ordinary Kriging interpolation method is most often the best solution for spatial interpolation. However, due to the flexibility of the IDW MSM method the difference is negligible in most of the cases. This can be explained by the fact that Kriging is highly sensitive to the accuracy metric being used. As explained previously, the Kriging interpolation minimizes the MSE, and, therefore, in terms of every other metric including RMAE, Kriging performance is suboptimal. Moreover, Kriging performs poorly when the number of observations is very low, unlike IDW or GIDS. However, Kriging is highly parametric which leaves space for many improvements. There are many advanced and robust semivariogram models and better interpolation approaches than the isotropic ordinary Kriging [50]. However, these improvements can result in significantly higher processing requirements than the other interpolation methods.

The general conclusion for the interpolation methods is that Kriging offers the best performance in terms of interpolation errors. However, due to the extensive processing and the weak performance in low observations point cases of the Kriging method, the IDW MSM is the most flexible and robust spatial statistics based interpolation method for direct REM estimation.

3.3.2 An in-band femto-cell urban scenario

The self-configuration and self-optimization of femto-cells, where REMs may provide environmental awareness for coverage and capacity enhancement in cellular networks [2] is an important scenario in this project. We assume a scenario where there are several neighboring femtocells. We further assume that a new femtocell is installed and is powered up, but it does not know its own (proper) transmit power. If the transmit power is too low, it may not cover the whole area that it is supposed to provide service to. If the transmit power is too high, it will probably cause interference to the neighboring femtocells (interference to the macrocells is not considered in this scenario). An optimum value of the transmit power should be set in order to compromise between coverage and interference.

In general, it is a challenging task to find this type of optimum value. One possible solution may be to proceed by trial-and-error, starting from a low value and gradually increasing until the interference limit is reached. In order not to exceed this limit, constant feedback from the neighboring femtocells is needed (the communication between femtocells should be carried out through the X2 interface which, however, does not necessarily exist in all the deployments). This creates excessive signaling overhead. Besides, it is prone to coverage holes and interference to neighboring femtocells, because the feedback depends only on the recently requested measurements from the mobile terminals. Since it is expected that a low number of mobile terminals will be connected to a femtocell, this will clearly be insufficient. If, for example, there is no interference feedback over a certain region, its requirements will be completely overrun during the reconfiguration. Then, when a mobile terminal happens to be in that particular region later on, it may experience interference.

A solution based on REMs may overcome this problem. In other words, REMs can provide the necessary environmental RF information so as to find the optimum transmit power. The exact coverage need and the coverage of neighboring femtocells in terms of geographic area can be retrieved from the REM. It may also provide statistical information on the propagation medium, so that the aforementioned optimum transmit power value can be calculated using a realistic propagation model.

As mentioned before a REM can be constructed using the geo-localized measurements coming from the mobile terminals (acting as sensors) as well as from the neighboring femtocells. The REM can either sit at the HeNB Gateway or at the Operation and Maintenance Center (OMC) for a global view of the RF environment that encompasses several neighboring femtocell coverage areas. An important requirement is to have the geo-location information with sufficient accuracy. Since most of the measurements for this scenario are *indoor*, geo-location accuracy through GPS is not guaranteed. Other methods of geo-localization, which make use of indoor access points, must be used to enhance the accuracy. Another important point to note is that the femtocells must also be equipped with geo-location capabilities (this is not mandatory by the 3GPP LTE standard).

Direct field estimation methods can be employed to construct REMs for this scenario, just as in the previous example. The details of the proposed construction method have been presented in Section 3.2.1.2.

The scenario we consider consists in a BS located in a urban area, on the rooftop of Orange Labs premises at Issy-les-Moulineaux, France. The antenna is 40m high and has isotropic gain. The radiated power is arbitrarily chosen as it simply offsets the path loss by a constant which will be determined by the parameters estimation. The resulting propagation is shown in Figure 35 with a 5m resolution. On this map we can identify the propagation effects resulting from the buildings configuration and guess where the street are located, although we do not account for penetration losses.

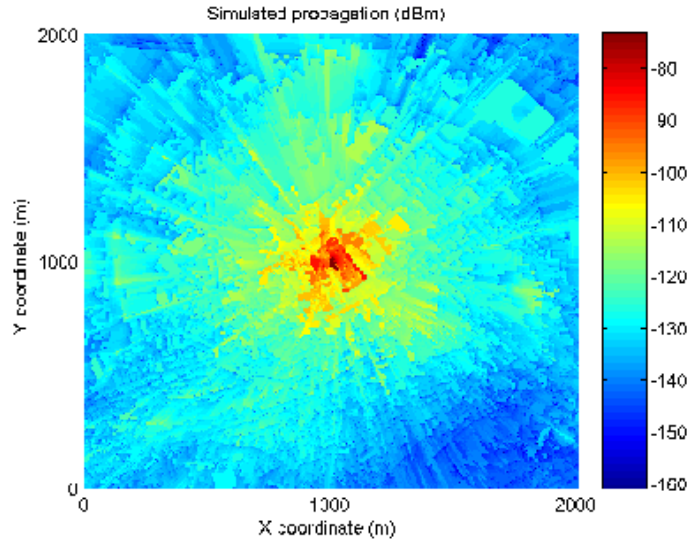


Figure 35: Received power in dBm from a single BS.

In order to estimate the parameters of the model as assumed in (3.5) we have to choose a sampling design. Here we simply want to validate the model and left aside the performance issues. Hence we choose a sampling for "measurements" at 2000 random locations on a disk centered on the BS and with 400m radius. This roughly represents 10% of the points located in the disk.

The prior are set according to (3.5), (3.35) and (3.36) and their parameters are given in Table 4 along with the estimated values.

Table 4: Parameters

Parameter	Prior parameters	Estimated values
β	$\mathbf{b} = \begin{pmatrix} -30 \\ -30 \end{pmatrix}$ $\mathbf{H} = \begin{pmatrix} 0.01 & 0 \\ 0 & 0.01 \end{pmatrix}$	(-38.7) (-31.3)
θ	$q = \frac{1}{30} \nu = 18$	0.041
ϕ	discrete 10m to 35m in 5m steps	15m
τ	discrete 0.01 to 1 in 0.1 steps	0.10

Figure 36 shows the propagation map with the trend removed so that only the shadowing and white noise terms remain:

$$\mathbf{y} - \mathbf{X}\mathbb{E}_{|\mathbf{y}}(\boldsymbol{\beta}) \quad (3.32)$$

It is notable that the shadowing is not isotropic, hence there is some room for propagation model improvement. Also the estimated correlation distance is quite low, although bigger patterns seems to appear on that Figure, for instance on the south east, there is a large zone where the shadowing has low values. On the terrain this zone matches quite well a small hill, suggesting for the addition of further regressors, providing that data are available, or alternatively a multi-scale covariance matrix.

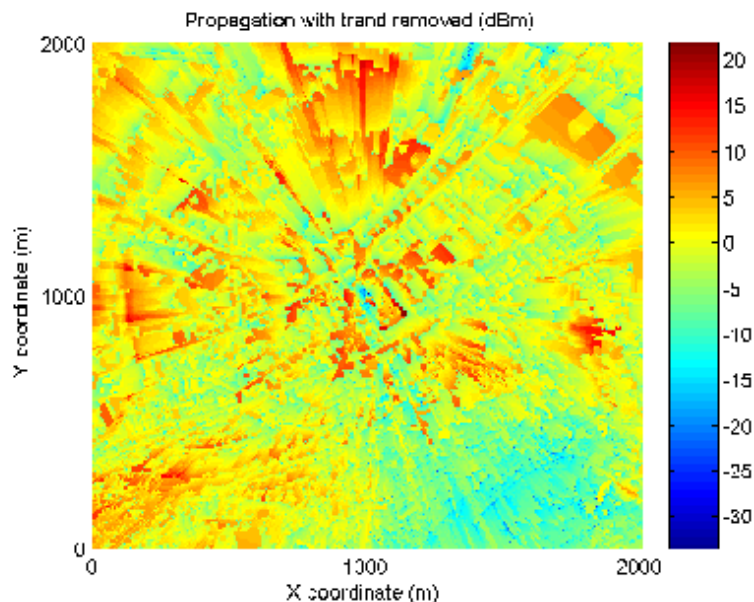


Figure 36: Propagation after removing the predicted trend.

We want to compute the field estimation capability of this approach. For that purpose we choose 1500 testing points on the above described disk at random locations and plot the cumulative distribution function (cdf) of the error. The resulting plot is shown on Figure 37. If the model was able to predict perfectly field, the cdf would be the one of white Gaussian noise: normal with variance $\frac{1}{\theta}$. Obviously this lower bound is never met because knowing the values of the shadowing at several points does not permit knowing exactly the value of the shadowing at another prediction point. On the other hand, if the estimation was useless, meaning the shadowing would be uncorrelated, the cdf would be normal with variance $\frac{1}{\theta}(1 + \tau)$. The variance we obtain from Figure 37 is 14, while the estimated variance of shadowing and noise is 24.4 and the variance of

the noise is 2.44. Then we can conclude that the Kriging method is probably worth the complexity. However, further work is needed to improve the model and increase the efficiency of the method.

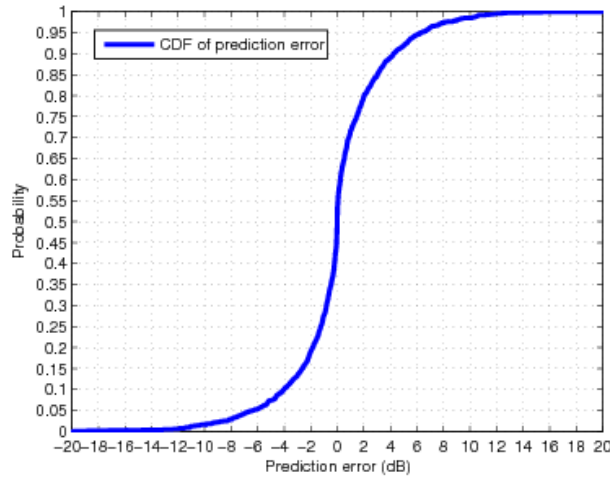


Figure 37: Cumulative distribution function (CDF) of the prediction error.

3.3.3 Compressed-sensing techniques for LTE in TVWS

In this section we assess the performance of the compressed sensing interpolation technique, described in Section 3.2.4. We choose to develop a specific example: REM generation for "out-of-band femto-cells", as detailed in [1], [2] and [3]. In particular, we assume the presence of only two kinds of radio transmitters: terrestrial broadcast television transmitters (fixed DVB-T transmitters) and cellular home base stations (fixed LTE-TDD transmitters); see Table 5.

Table 5: Main choices for the data models (from [3])

Parameter		modelling choice	alternative choice
Region		Europe	other regions
Frequency band		470-790 MHz, 8 MHz channels	
Primaries	Service	Terrestrial broadcast television	
	Technology	DVB-T	
	rate of change	order of weeks, months	
	REM provides	location, power, height	TV database available
Secondaries	service	cellular data	
	Technology	LTE TDD	
	Duplexing	TDD	FDD
	rate of change	order of hours	
	Regulation	exclusively licensed	shared use
Sensors	REM provides	location, power	
	reside in	UEs	
	Provide	RSS, location, timestamp	
	Mobility	0-50 km/h	

We further assume that the TV transmitter locations, transmit powers, antenna heights and other relevant transmitter characteristics are known to the secondary network by means of a nation-wide database. The transmitter characteristics of the home base stations, however, are *not* known to the network. The goal here is to estimate these unknown transmitter characteristics to such an accuracy that a useful map of the radio interference can be generated. To this end, radio field measurements are collected and reported to the network by a set of mobile sensors, typically residing in user equipment (mobile phones, laptops, etc.).

In accordance with further assumptions in [3], we concentrate on the local interference statistics in a region of a few blocks in a residential area. Within such an area of a less than a square kilometer, and within the frequency band of one particular TV channel, we assume that only very few transmitters are simultaneously active at a certain time.

The unknown characteristics of the (few) transmitters are:

1. their number: we will evaluate the performance of our algorithms in terms of the classical "probability of detection" and the "probability of miss" mentioned before.
2. their locations: we will evaluate the performance of our algorithms in terms of a "mean location error" in meters.
3. their power: we will evaluate the performance of our algorithms in terms of a mean power error.

Elaborating on the propagation model described in [3], we adopt the following for the received power:

$$P_r = C_1 \sum_t G_{rt}^{TV} d_{rt}^{-\alpha} P_t^{TV} + C_2 \sum_t G_{rt}^{LTE} d_{rt}^{-\alpha} P_t^{LTE} + \sigma_r^2 \quad (3.33)$$

We are thus interested in the unknown transmitters with transit power P_t^{LTE} and we assume that the TV transmitters with powers P_t^{TV} are known. The model reduces to

$$P_r(j) = \sum_t G_{rt}^{LTE} d_{rt}^{-\alpha} P_t^{LTE} + P^{TV} + \sigma_r^2 \quad (3.34)$$

An example of the radio power received at a grid of points is illustrated in Figure 38, for the situation where 2 active LTE transmitters operate in a region of interest.

In this section we will describe ways to determine the radio field P_r . We will denote the reconstructed field by \hat{P}_r . The following two performance measures will be relevant:

1. $e_1 = \Pr\{\max_i \{|\hat{P}_r(i) - P_r(i)|\} < \varepsilon\}$ is the probability that the reconstructed field is within ε from the true field in *all* relevant locations i . For small values of ε , we would typically speak about *perfect reconstruction* when e_1 is close to one. We will refer to this criterion as the *probability of perfect reconstruction*.
2. $e_2 = E\{|10 \log_{10} \hat{P}_r(i) - 10 \log_{10} P_r(i)|\}$ is the average error of the reconstructed field strength of the REM in dBm. We will refer to this criterion as the *average REM error*.

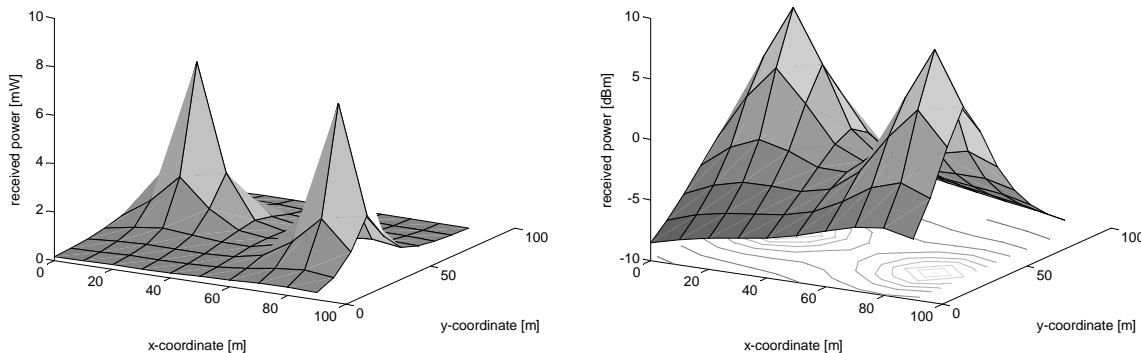


Figure 38: Example of a radio field (received power) with 2 separate transmitters measured at a 100m x 100m grid with 10m resolution. (in milliwatts (left) and in dBm (right)) .

In these error criteria, the probability and the mean are taken as averages over all the potential combinations of number of transmitters, transmitter powers and transmitter locations. In a strict conceptual sense, the “probability” above is thus merely the fraction and the “mean” is merely the sample average, as there are no stochastic variables involved in the model.

Simulation results for choices of the grid and the transmitter parameters corresponding to low-power transmitters are shown in Section 3.3.3.1, whereas results for a more realistic setup can be found in Section 3.3.3.2.

3.3.3.1 Low-power transmitter scenario

Consider a square grid of 100 gridpoints. These are spaced 10m apart, hence the area covered by this grid is 100mx100m. Transmitters are randomly placed on 1, 2, or 3 points of this grid, and so are the sensors. The powers of the transmitters are 20 mW.

In a first batch of simulations, we investigate the static sensors. Figure 39 shows the two error criteria (probability of perfect reconstruction and average REM error) in 2 subplots. In particular, these metrics are shown as a function of the number of static sensors. Note that perfect reconstruction is not accomplished unless there is a static sensor *at each gridpoint in the grid*. The more practical error metric in the right-hand plot illustrates that perfect reconstruction may not be needed in order to yield practical results. An average error below 1dBm is achieved when at least 75 gridpoints contain a sensor. This number is clearly still too high to have practical ramifications.

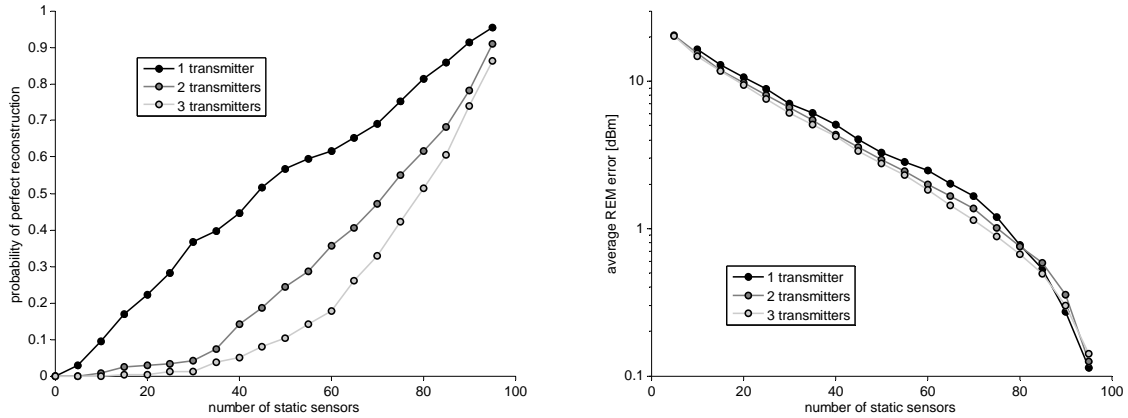


Figure 39: Static sensors.

Figure 40 shows the same curves for a scenario where ideal compressing sensors operate in the region of interest. Clearly, perfect reconstruction of the radio field is achieved with less than 20 sensors in place. These results are rather academic, however, as each of these sensors needs measurements of all the 100 gridpoints to generate its projected sample.

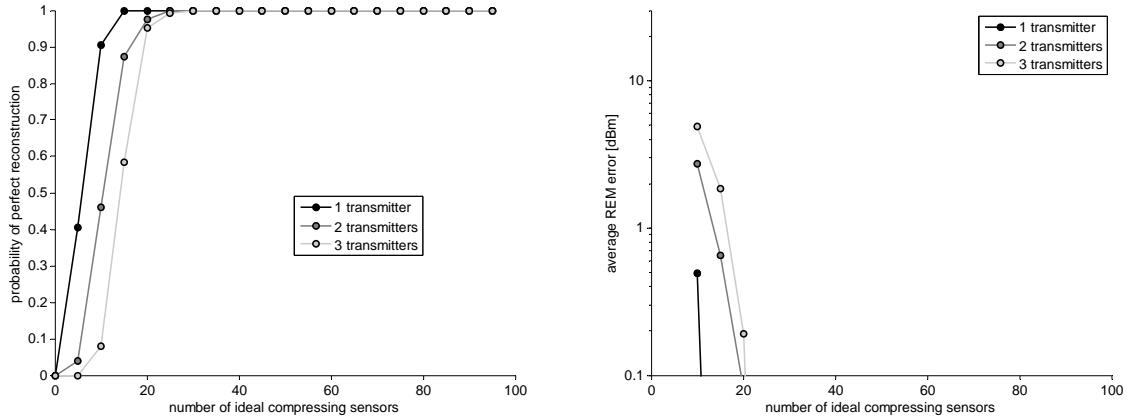


Figure 40: Ideal compressing sensors.

With the above two scenarios being rather extreme and non-practical cases, Figure 41 illustrates a practical situation for 2 transmitters, where mobile sensors appear in the region of interest. These sensors collect measurements in 5, 10 and 20 grid points respectively and project these measurements onto one single scalar sample each, which is uploaded to the network. These samples are then used to reconstruct the radio field. While the results are not as good as for the ideal sensors in Figure 5, perfect reconstruction is accomplished with 30 mobile sensors collecting measurements from 20 gridpoints each. Average REM error below 1 dBm is achieved with less than 25 mobile sensors even when these sensors only gather measurements in 10 points each.

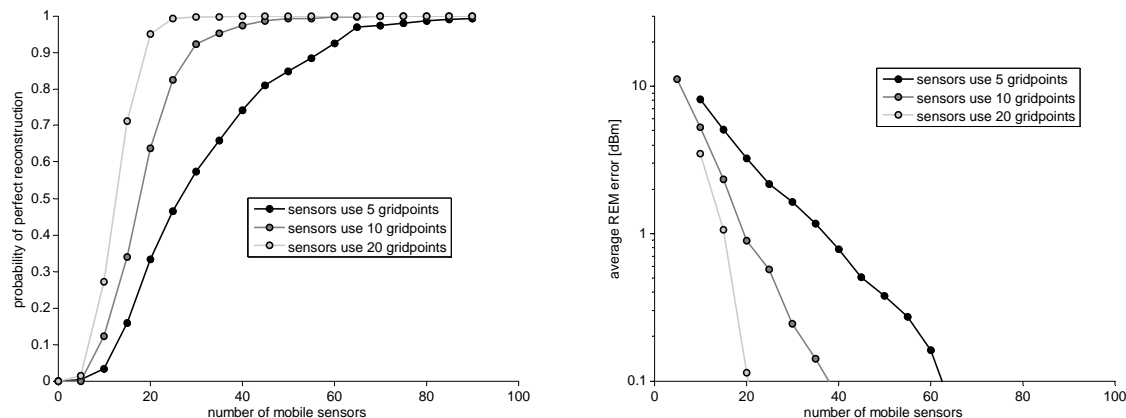


Figure 41: Mobile (compressing) sensors.

3.3.3.2 LTE in TVWS scenario

In this section, we evaluate a scenario where a grid of size 50x50 and a resolution of 10m. represents a residential area of 0.5 x 0.5 km, where a few unknown secondary transmitters operate. The power and the locations of these transmitters are not known to the network. Also, the network has no a priori knowledge about the number of the transmitters existing in this area. Using the algorithms explained in 3.2.4, we simulate the generation of maps reflecting the strength of the radio interference field at the grid points.

3.3.3.2.1 Randomly distributed measurements

In the first set of simulations, we explore the scenario where a number of field strength measurements are available at random positions in the area. The performance criteria we evaluate are the average field error as described in above, along with the standard deviation of this error.

Figure 42 illustrates the results of this simulation. The top left figure illustrates the true radio field, unknown to the network. The bottom Figures illustrate the estimated map when various number of random measurements are available (100, 500, and 1000 measurements respectively, from left to right). In the top center plot the average field error in dBm is illustrated as a function of the number of measurements and the top right plot illustrates the associated standard deviation.

The field estimation appears to be unbiased (average field error close to zero), and in order to reduce the error standard deviation below 1dB, at least 250 random measurements need to be available.

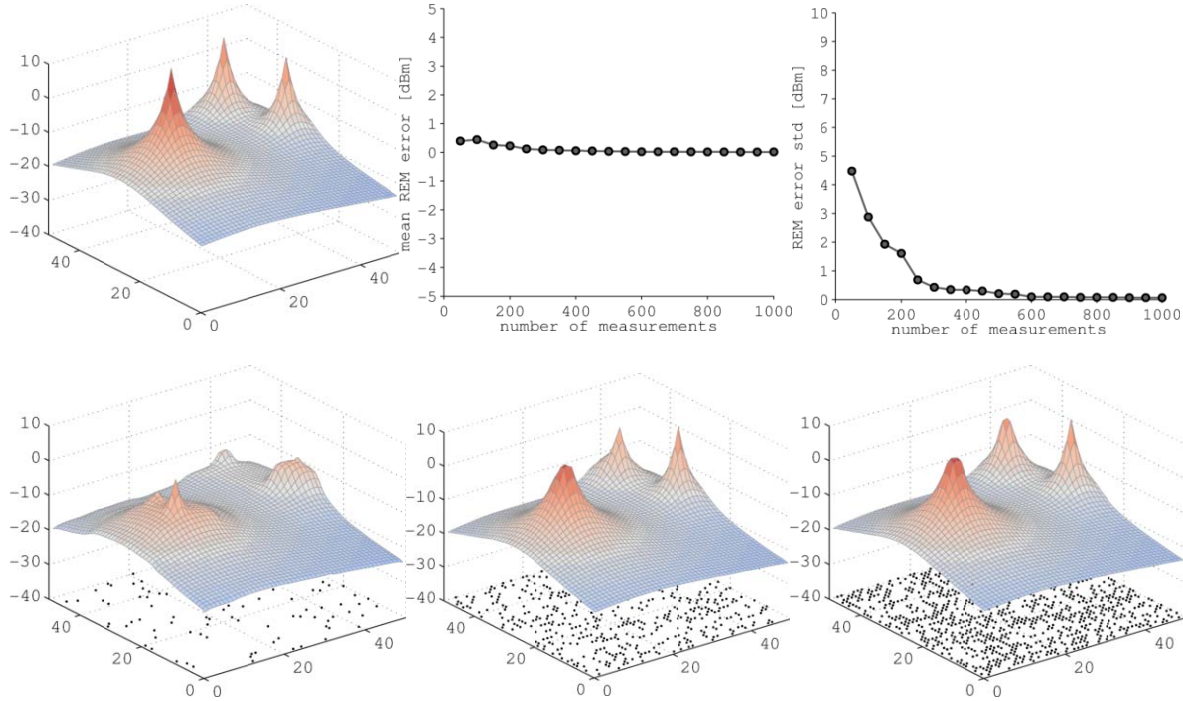


Figure 42: Figure 1: The true radio field (top left), the estimated radio field for various number of randomly located measurements (bottom left to bottom right), along with the average field error and the field error standard deviation as a function of the number of measurements (top center and top right, respectively).

3.3.3.2.2 Measurements by few moving mobile devices

In a realistic scenario, it is unlikely that measurements appear in random fashion as we have assumed in the previous section. Instead, measurements are envisaged to be carried out by mobile users and one mobile device could actually provide a series or burst of measurements, each sample representing a different location. In the following we present simulations results that reflect this reality. In particular, we assume that each mobile sensor crosses the area of interest in a straight line, this line appearing in a random position on the map. We apply a wrap-around topology in order to assure that each burst of measurements provided by the sensors contains exactly 50 measurements. The results are illustrated in Figure 43. Note that these simulation assumptions incorporate the situation where the true radio field is static and mobile sensors appear one after another in the area of interest, reporting their measurements at different time instants. The radio field is then estimated at any time new measurements are received, hence reflecting a gradual (adaptive) improvement of the field knowledge in the area. Again, the true field is shown in the top left plot and the bottom figures illustrate the estimated field based on the measurements indicated at the bottom of the respective plots. From left to right, these three figures represent (2, 10 and 20 mobile sensors, each reporting a burst of 50 measurements to the network). While the spatial correlation of the measurements slightly deteriorates the performance of the estimated field in terms of the standard deviation, it appears that with only a few mobile sensors the field is estimated to within 2dB standard deviation accuracy.

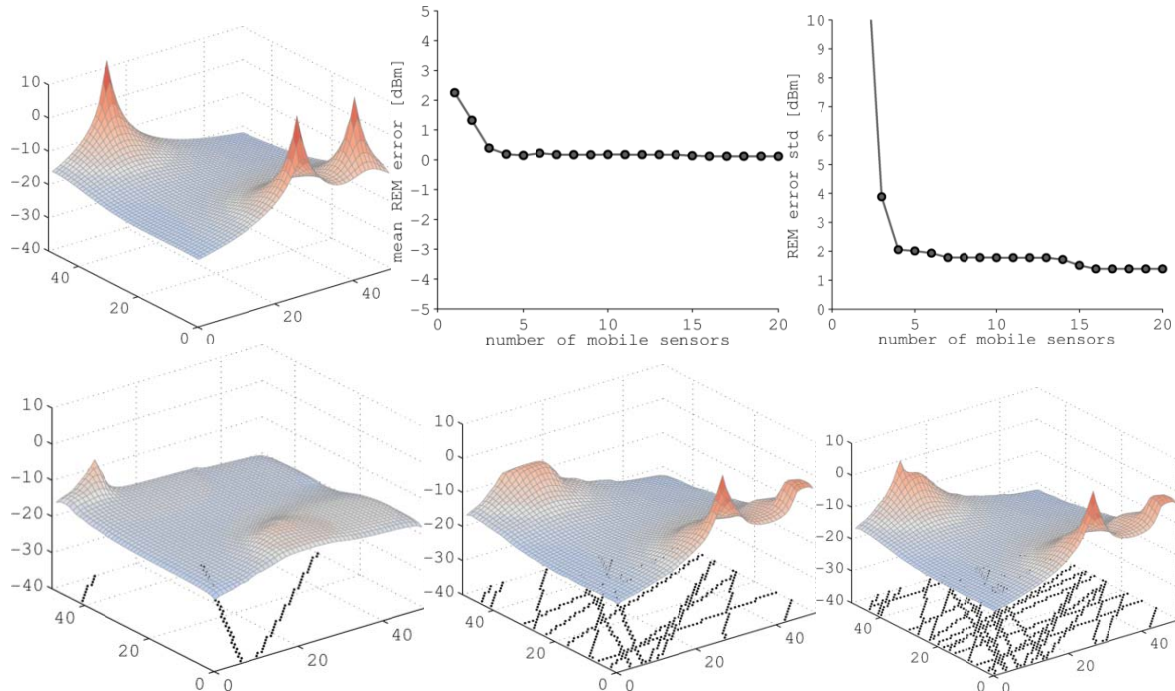


Figure 43: The true radio field (top left), the estimated radio field for various number of mobile sensors moving in straight lines (bottom left to bottom right), along with the average field error and the field error standard deviation as a function of the number of measurements (top center and top right, respectively).

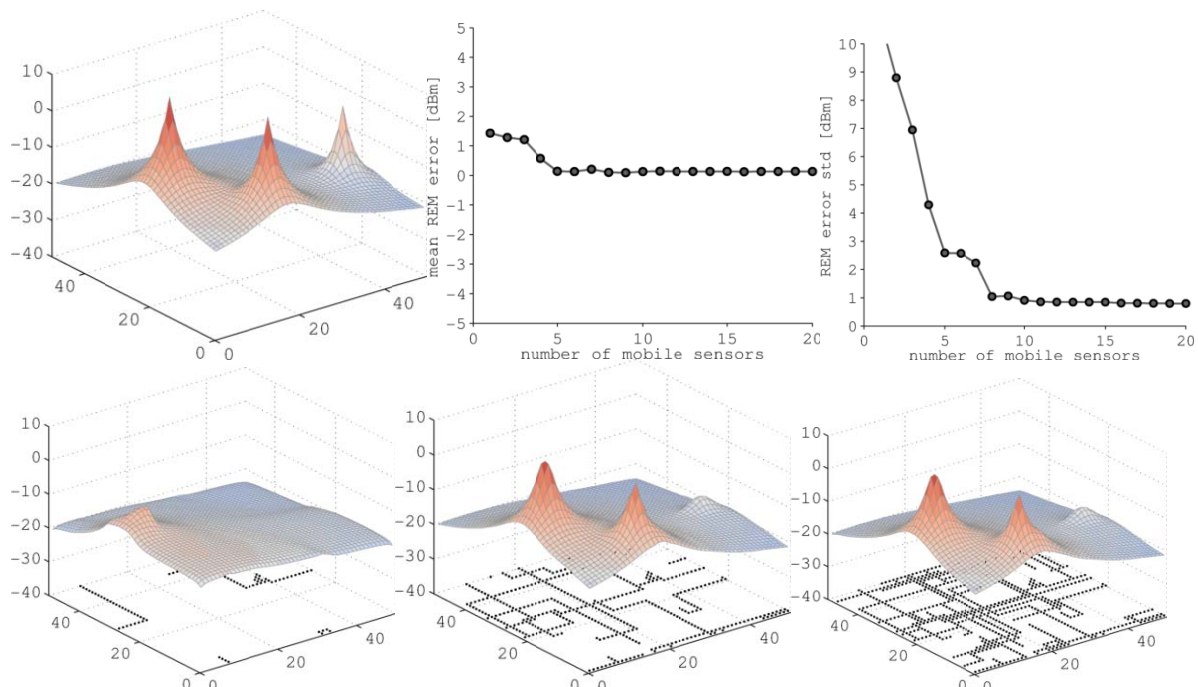


Figure 44: The true radio field (top left), the estimated radio field for various number of mobile sensors moving in random-walk fashion (bottom left to bottom right), along with the average field error and the field error standard deviation as a function of the number of measurements (top center and top right, respectively).

Finally, Figure 44 illustrates the scenario where the spatial correlation of the measurements is introduced through random walks in the area (again with the wrap-around topology that assures bursts of 50 measurements per sensor). A sensor now moves across the region with a 10% probability to turn left or right and a 90% probability to continue in the same direction. In this mobility scenario, a 1dB standard deviation accuracy) is accomplished with 8 mobile sensors.

4 Conclusions

The present deliverable has taken a broad view of the various techniques and methodologies suitable for radio field estimation and source characterization/localization (also known as “neighborhood mapping”), all of which are critical entries in a dynamic REM. It has exhaustively listed all possible (and currently known) approaches, including those based on pseudo-coherent (complex-gain-based) and non-coherent (power-based) measurements taken by sensors distributed in a given area. It has classified and catalogued all such techniques to the degree possible, and has also shown how the estimation of location-dependent parameters can in turn lead to actual source localization (the “fusion” problem). It has also performed analysis and performance assessment for a number of key FARAMIR scenarios. Although a comprehensive comparison of techniques for a common set of scenarios has yet to be performed (so preferential conclusions can be drawn), the groundwork has been laid for this to happen in the ongoing work.

In the process of researching these topics, a number of important results have been obtained. For example:

- A new framework for source detection and approximate localization has been proposed, based on a rather simple idea: first estimate appropriately-chosen parameters and then use the results to perform detection (a reversal of usual thinking). This type of statistical-inference test employs successive and independent estimates of signal features to decide upon the presence or absence of a signal. The trick here is to select features whose values are rather insensitive to modeling uncertainties (like the noise level). A highly accurate approximate analysis of the proposed test has been provided, enabling performance characterization and optimization. Two application examples have been provided that demonstrate the use of the concept in greater detail. This approach opens a new paradigm for source detection (sensing) and will be pursued further.
- It was also shown that it is possible to identify the AOAs of multiple distinct paths, all emanating from a single source, which arrive at a passively-receiving array in different temporal “energy piles”. This is possible via a two-stage processing approach, and this can be achieved regardless of whether there is training-data information or not (i.e., it can be done blindly). The main idea is to estimate the path-temporal separation first and then use these estimates, plus the overall-channel estimates, in order to estimate the path-AOAs. The theoretical performance results show that the AOA estimation performance is very close to the theoretical bounds (Cramer-Rao) in a variety of challenging propagation environments, even when only one observation data block is available. Furthermore, it was shown that, in the case of sufficient temporal separation between the propagation paths, the algorithm provides very reliable AOA estimation performance *even when the number of existing spatial paths exceeds the number of array elements* (a hitherto counter-intuitive result).
- A technique for obtaining field estimation via Maximum Likelihood in a shadow-fading environment has been derived, involving localization and power estimation of an

unknown number of sources in a given band. Numerical results were presented that confirm the theoretical claims.

- A direct field-estimation approach has been explored based on the recently-popular method of *compressed sensing* (sparsity). Here also an assessment of the proposed method for an LTE scenario in TVWS was also provided.
- Another direct field-estimation method has been proposed based on a Gaussian model, whereby estimation is performed under a Bayesian framework for incorporating partial information. Although a single transmitter source is assumed, the approach is generalizable to multiple sources as long as the RF measurements can be performed *per source*, i.e., source separation (through decoding) can be performed at the sensors/measurement devices. An assessment of the proposed method was based on the chosen application scenario of self-configuring and self-optimizing femto-cells.
- Finally, an analysis and related comparisons of three different interpolation techniques were presented. These were the ordinary Kriging interpolation, the Inverse Distance Weighting (IDW) modified Shepard's method and the gradient plus Inverse Distance Squared (GIDS) method. A comparison was performed for both indoor and outdoor scenarios.

A high-level view of the obtained results indicates that a good number of meaningful approaches have been laid out, examined in greater detail and assessed on various selected scenarios. Because the conclusions rely on a set of scenario-dependent and modeling-dependent assumptions each, a straightforward comparison between them is still elusive. As a first subsequent step, such a comparison should be performed under a commonly-agreed upon set of parameters for the models at hand. That, however, would be the first (conceptual) step. In practice, a result is as good as the model behind it. It is therefore meaningful to extract the most promising (and robust) solutions from those compared and to proceed with experimental verification in the field. This will pave the way for a truly meaningful and all-conclusive assessment of the exciting question of how to build an adaptive radio map from a set of sensor-based measurements.

5 Appendix – Derivations from Section 3.2.1.2

The joint posterior for β and θ can be derived as follows:

$$p(\beta, \theta | \phi, \tau, \mathbf{y}) = \frac{p(\mathbf{y} | \beta, \theta, \phi, \tau) p(\beta, \theta | \phi, \tau)}{\int_{\beta, \theta} p(\mathbf{y} | \beta, \theta, \phi, \tau) p(\beta, \theta | \phi, \tau)} \quad (3.35)$$

$$\propto \theta^{\frac{\mu''}{2}} \exp \left[-\frac{\theta}{2} (\beta - \mathbf{b}'')^T H'^{-1} (\beta - \mathbf{b}'') \right] \theta^{\frac{\nu''}{2}-1} \exp \left[-\frac{\theta}{2} \nu' q'' \right] \quad (3.36)$$

The prior pdf mentioned above is a conjugate prior, the expressions for the posterior parameters are given in [34] and the normalisation constant can be found easily by stating that the integral wrt θ and β is equal to one:

$$K(\phi, \tau, \mathbf{y}) = (2\pi)^{-\frac{\mu''}{2}} |H''|^{\frac{1}{2}} \left(\frac{\nu' q''}{2} \right)^{\frac{\nu''}{2}} \Gamma^{-1} \left(\frac{\nu''}{2} \right) \quad (3.37)$$

Now we can derive the posterior for the covariance parameters ϕ and τ noting that:

$$p(\beta, \theta, \phi, \tau | \mathbf{y}) = K_1(\mathbf{y}) p(\mathbf{y} | \beta, \theta, \phi, \tau) p(\beta, \theta, \phi, \tau) \quad (3.38)$$

and

$$p(\beta, \theta, \phi, \tau | \mathbf{y}) = p(\beta, \theta | \phi, \tau, \mathbf{y}) p(\phi, \tau | \mathbf{y}) \quad (3.39)$$

Hence we obtain that:

$$\begin{aligned} p(\phi, \tau | \mathbf{y}) &= K_1(\mathbf{y}) p(\mathbf{y} | \beta, \theta, \phi, \tau) p(\beta, \theta, \phi, \tau) \frac{1}{p(\beta, \theta | \phi, \tau, \mathbf{y})} \\ &= K_1(\mathbf{y}) (2\pi)^{-\frac{N}{2}} |R(\phi) + \tau I|^{-\frac{1}{2}} |H|^{\frac{1}{2}} |H''|^{-\frac{1}{2}} \left(\frac{\nu q}{2} \right)^{\frac{\nu}{2}} \left(\frac{\nu' q''}{2} \right)^{-\frac{\nu''}{2}} \Gamma^{-1} \left(\frac{\nu}{2} \right) \Gamma \left(\frac{\nu''}{2} \right) p(\phi, \tau) \end{aligned}$$

Denoting $S = R + \tau I$ we obtain:

$$\begin{aligned} p(\phi, \tau | \mathbf{y}) &= p(\phi, \tau) K_1(\mathbf{y}) (2\pi)^{-\frac{N}{2}} |S^{-1}|^{\frac{1}{2}} |H|^{\frac{1}{2}} \left(\frac{\nu q}{2} \right)^{\frac{\nu}{2}} \Gamma^{-1} \left(\frac{\nu}{2} \right) \Gamma \left(\frac{\nu+N}{2} \right) |H + X^T S^{-1} X|^{-\frac{1}{2}} \times \\ &\quad \left(\frac{\nu q + \mathbf{y}^T S^{-1} (\mathbf{y} - X\mathbf{b}) - (\mathbf{b}^T H + \mathbf{y}^T S^{-1} X)(H + X^T S^{-1} X)^{-1} X^T S^{-1} (\mathbf{y} - X\mathbf{b})}{2} \right)^{-\frac{\nu+N}{2}} \end{aligned} \quad (3.40)$$

where K_1 is a function of \mathbf{y} only and can be numerically evaluated.

It is interesting to derive the marginal posterior for θ and β :

$$p(\theta | \phi, \tau, \mathbf{y}) = \left(\frac{\nu' q''}{2} \right)^{\frac{\nu''}{2}} \Gamma^{-1} \left(\frac{\nu''}{2} \right) \theta^{\frac{\nu''}{2}-1} \exp \left[-\frac{\theta}{2} \nu' q'' \right] \quad (3.41)$$

$$\begin{aligned}
p(\beta|\phi, \tau, \mathbf{y}) &= \\
(2\pi)^{-\frac{\mu''}{2}} |H''|^{\frac{1}{2}} \left(\frac{\nu' - q''}{2}\right)^{\frac{\nu''}{2}} \Gamma^{-1}\left(\frac{\nu''}{2}\right) \times \Gamma\left(\frac{\mu' - \nu''}{2}\right) &\left(\frac{2}{\nu' - q' + (\beta - \mathbf{b}'')^T H' - (\beta - \mathbf{b}'')}\right)^{\frac{\mu' - \nu''}{2}} \\
&= \pi^{-\frac{\mu''}{2}} \left|\frac{H''}{q''}\right|^{\frac{1}{2}} \nu''^{-\frac{\mu''}{2}} \Gamma^{-1}\left(\frac{\nu''}{2}\right) \Gamma\left(\frac{\mu' - \nu''}{2}\right) \left(1 + \frac{1}{\nu''} (\beta - \mathbf{b}'')^T \frac{H''}{q''} (\beta - \mathbf{b}'')\right)^{-\frac{\mu' - \nu''}{2}}
\end{aligned} \tag{3.42}$$

Those are found by integrating (3.35) wrt β and θ respectively. (3.41) is a gamma 2 distribution with mean $\frac{1}{q''}$ and variance $\frac{2}{\nu'' q''^2}$ while (3.42) is a $\mu' - \nu''$ -multivariate student distribution with $\nu' - \nu''$ degrees of freedom, scaling matrix $q'' H''^{-1}$ and mean \mathbf{b}'' .

Then we can take the marginal wrt ϕ and τ :

$$p(\theta|\mathbf{y}) = \iint_{\phi, \tau} p(\theta|\phi, \tau, \mathbf{y}) p(\phi, \tau|\mathbf{y}) \tag{3.43}$$

$$p(\beta|\mathbf{y}) = \iint_{\phi, \tau} p(\beta|\phi, \tau, \mathbf{y}) p(\phi, \tau|\mathbf{y}) \tag{3.44}$$

Those two integrals use (3.41) and (3.42) respectively and can be evaluated providing that (3.40) is discrete.

We shall also compute the distribution (and the moments) of $p(\mathbf{y}_1|\mathbf{y})$. In the following, we assume that:

$$\begin{pmatrix} \mathbf{y}_1 \\ \mathbf{y} \end{pmatrix} \equiv \mathcal{N} \left(\begin{pmatrix} X_1 \\ X \end{pmatrix} \beta, \frac{1}{\theta} \begin{pmatrix} S_{11}(\phi) & S_{1y}(\phi) \\ S_{y1}(\phi) & S_{yy}(\phi) \end{pmatrix} + \tau I \right) \tag{3.45}$$

$$p(\mathbf{y}_1|\mathbf{y}) = \int \int \int \int_{\beta, \theta, \phi, \tau} p(\mathbf{y}_1|\beta, \theta, \phi, \tau, \mathbf{y}) p(\beta, \theta, \phi, \tau|\mathbf{y}) \tag{3.46}$$

$$= \iiint_{\theta, \phi, \tau} \left[\int_{\beta} p(\mathbf{y}_1|\beta, \theta, \phi, \tau, \mathbf{y}) p(\beta|\theta, \phi, \tau, \mathbf{y}) \right] p(\theta|\phi, \tau, \mathbf{y}) p(\phi, \tau|\mathbf{y}) \tag{3.47}$$

The inner integral, denoted $p(\mathbf{y}_1|\phi, \theta, \tau, \mathbf{y})$, turns out to be the marginalisation (wrt β) of a joint gaussian pdf. Its parameters are given in [34] equations (3.45) and (3.46).

$$p(\mathbf{y}_1|\mathbf{y}) = \iint_{\phi, \tau} \left[\int_{\theta} p(\mathbf{y}_1|\phi, \theta, \tau, \mathbf{y}) p(\theta|\phi, \tau, \mathbf{y}) \right] p(\phi, \tau|\mathbf{y}) \tag{3.48}$$

Now the inner integral is a student distribution according to [35] with mean and covariance:

$$\begin{aligned}
\mathbb{E}_{|\phi, \tau, \mathbf{y}}(\mathbf{y}_1) &= \\
(X_1 - S_{1y} S_{yy}^{-1} X) H''^{-1} H' - b' + (S_{1y} S_{yy}^{-1} + (X_1 - S_{1y} S_{yy}^{-1} X) H''^{-1} X^T S_{yy}^{-1}) \mathbf{y} &
\end{aligned} \tag{3.49}$$

$$cov_{|\phi, \tau, \mathbf{y}}(\mathbf{y}_1) = \frac{\nu'' q''}{\nu'' - 2} [S_{11} - S_{1y} S_{yy}^{-1} S_{y1} + (X_1 - S_{1y} S_{yy}^{-1} X) H''^{-1} (X_1 - S_{1y} S_{yy}^{-1} X)^T] \tag{3.50}$$

Glossary and Definitions

Term	Description
3GPP	3 rd Generation Partnership Project
AIC	Akaike Information Criterion
AOA	Angle Of Arrival
BS	Base Station
CFAR	Constant-False-Alarm-Rate
CRLB	Cramer-Rao Lower Bound Cyclic Prefix
CR	Cognitive Radio
C-N	Cognitive Node
DSA	Dynamic Spectrum Access
DVB	Digital Video Broadcasting
FOA	Frequency Of Arrival
GIDS	Gradient-plus-Inverse-Distance-Squared
GPS	Global Positioning System
GSM	Global System for Mobile Communications
HeNB	Home eNB
IC	Interference Cartography
IDW	Inverse Distance Weighted
LMS	Least Mean Squares
LOS	Line-Of-Sight
LS	Least Squares
LSE	LS-Estimates
LTE	Long Term Evolution

Term	Description
MCD	Measurement Capable Devices
MDL	Minimum-Description Length
MIMO	Multiple Input Multiple Output
MLR	Multiple-Linear Regression
ML	Maximum Likelihood
MLE	Maximum Likelihood Estimator
MSM	Modified Shepard's Method
MUD	Multi-User Detection
MUSIC	Multiple Signal Classification
NOPE	Number Of Paths Estimation
OCHIR	Overall Channel Impulse Response
OLS	Ordinary Least Squares
OMC	Operation and Maintenance Center
OFDM	Orthogonal Frequency Division Multiplexing
P-BS	Primary BS
PSD	Power Spectral Density
PSP	Per-Survivor Processing
PTS	Path Temporal Separation
PU	Primary User
REA	Radio Environmental Awareness
REM	Radio Environmental Map
RIFE	Radio-Interference Field Estimation-RIFE
RMAE	Relative Mean Absolute Error

Term	Description
RMSE	Root-Mean Squared Error
ROC	Receiver Operating Characteristic
RSS	Received Signal Strength
SINR	Signal to Interference plus Noise Ratio
TDOA	Time Difference Of Arrival
TIN	Triangular Irregular Network
TOA	Time Of Arrival
TPS	Thin Plate Spline
TVWS	TV White Spaces
White space	part(s) of spectrum allocated to a particular radio system (primary radio system) in particular location(s) that may be temporary unused by this primary radio system in some location(s) and thus allowed by radio regulations to be used by another radio system(s) (secondary radio system) on a temporary secondary basis without causing harmful interference to the primary radio system, where harmful interference and protection mechanisms are defined in the radio regulations
WCP	Worst Case Position

References

- [1] FARAMIR Deliverable D2.1: "State of the Art Review," <http://www.ict-faramir.eu/>.
- [2] FARAMIR Deliverable D2.2: "Scenario Definitions," <http://www.ict-faramir.eu/>.
- [3] FARAMIR Deliverable D4.1: "Radio Environmental Maps: Information Models and Reference Model," <http://www.ict-faramir.eu/>.
- [4] H. Urkowitz, "Energy Detection of Unknown Deterministic Signals," *Proceedings of the IEEE*, pp. 523-531, Apr. 1967.
- [5] R. Tandra, and A.Sahai, "SNR Walls for Feature Detectors," IEEE DySPAN 2007, pp. 559 - 570, Apr. 2007.
- [6] R. Tandra and A. Sahai, "SNR walls for signal detection," *IEEE Journal on Selected Topics in Signal Processing*, pp. 4-17, Feb. 2008.
- [7] T. Ikuma and M.Naraghi-Pour, "A Comparison of Three Classes of Spectrum Sensing Techniques", IEEE GLOBECOM 2011, New Orleans, L.A., USA, 1-5 Nov. 2008..
- [8] J. V. DiFranco and W. L. Rubin, "Radar Detection Prentice-Hall," NJ, USA:Englewood Cliffs, 1968.
- [9] F. Digham, M-S. Alouini, M.K Simon, M. K. "On the Energy Detection of Unknown Signals Over Fading Channels," *IEEE Transactions on Communications*, , vol. 55, pp. 21-24, Jan. 2007.
- [10] M. Naraghi-Pour and T. Ikuma, "Autocorrelation-Based Spectrum Sensing for Cognitive Radios," *IEEE Transactions on Vehicular Technology*, Feb. 2010.
- [11] Y. Zeng and Y. Liang, "Covariance based signal detections for cognitive radio," in 2nd IEEE DySPAN, Dublin, Ireland, 2007, pp. 202-207.
- [12] C. Sachin, L. Jarmo, K. Visa, "Collaborative Autocorrelation-Based Spectrum Sensing of OFDM signals in Cognitive Radios," 42nd Annual Conference on Information Sciences and Systems 2008, Princeton, NJ, USA, Mar. 2008.
- [13] K. Karil, D. Chawla, V. Sarwate, "Upper Bounds on the Probability of Error for M-ary Orthogonal Signaling in white Gaussian noise," *IEEE Trans. on Information Theory*, vol 36, no. 30, May 1990.
- [14] S. Boyd and L. Vandenberghe, "Convex Optimization," Cambridge University Press, 2004.
- [15] E. Gönen and J. M. Mendel, "Subspace-based direction finding methods," in Digital Signal Processing Handbook, V. K. Madisetti and D. B. Williams, Eds. Boca Raton, FL: CRC Press, Inc., 1997.
- [16] M. Wax and I. Ziskind, "On unique localization of multiple sources by passive sensor arrays," *IEEE Trans. Acoust., Speech, Signal Process.*, vol. 37, pp 996-1000, Jul. 1989.
- [17] R. O. Schmidt, "Multiple emitter location and signal parameter estimation," *IEEE Trans. Antennas Propag.*, vol. 34, pp. 276-280, Mar. 1986.
- [18] T.-J. Shan, M. Wax, and T. Kailath, "On spatial smoothing for direction of- arrival estimation of coherent signals," *IEEE Trans. Acoust., Speech, Signal Process.*, vol. 33, pp. 806-811, Aug. 1985.
- [19] I. Ziskind and M. Wax, "Maximum likelihood localization of multiple sources by alternating projection," *IEEE Trans. Acoust., Speech, Signal Process.*, vol. 36, pp 1553-1660, Oct. 1988.

- [20] M. C. Vanderveen, B. C. Ng, C. B. Papadias, and A. Paulraj, "Joint angle and delay estimation (JADE) for signals in multipath environments," in Proc. 30th Asilomar Conf. Circuits, Syst. Comput., Pacific Grove, CA, vol. 2, pp. 1250-1254, Nov. 1996.
- [21] K. M. Chugg, "Blind acquisition characteristics of PSP-based sequence detectors," *IEEE J. Sel. Areas Commun.*, vol. 16, pp. 1518-1529, Oct. 1998.
- [22] K. Lerdsuwanakij, "On receivers for multipath fading and random phase channels," Ph.D. dissertation, Communication Sciences Institute, Univ. of Southern California, Los Angeles, CA, 2000.
- [23] M. Wax and I. Ziskind, "On Unique Localization of Multiple Sources by Passive Sensor Arrays," *IEEE Trans. Acoust., Speech, Signal Process*, vol. 37, pp. 996-1000, July 1989.
- [24] M. C. Vanderveen, C. B. Papadias, and A. Paulraj, "Joint Angle and Delay Estimation (JADE) for Multipath Signals Arriving at an Antenna Array," *IEEE Comm. Letters*, vol. 1, pp. 12-14, Jan. 1997.
- [25] M. C. Vanderveen, "Estimation of Parametric Channel Models in Wireless Communication Networks," Ph.D. thesis, Stanford University, Palo Alto, CA, 1997.
- [26] H. Akaike, "A New Look at the Statistical Model Identification," *IEEE Trans. Automat. Contr.*, vol. 19, pp. 716-723, Apr. 1974
- [27] J. Rissanen, "Modeling by Shortest Data Description," *Automatica*, vol. 14, pp. 465-471, 1978.
- [28] M. Wax and T. Kailath, "Detection of Signals by Information Theoretic Criteria," *IEEE Trans. Acoust., Speech, Signal Process*, vol. 33, pp. 387-392, Apr. 1985.
- [29] P. Panagiotou, A. Polydoros, and C. Oh, "An efficient, PSP-based digital modulation classifier," in Proc. MILCOM, Orlando, FL, pp. 1-8, Oct. 2007.
- [30] C. Botteron, "A statistical analysis of the performance of radio location techniques," Ph.D. dissertation, Dept. Elec. and Comp. Eng., Univ. of Calgary, Calgary, Alberta, 2003.
- [31] C. Feng, S. Valace and Z. Tan, "Multiple target Localization Using Compressive Sensing," in Proc. IEEE GLOBECOM 2009, Honolulu, Hawaii, USA, 30-4 Dec. 2009.
- [32] NEWCOM++, Deliverable DB.1: "Review of Satellite, Terrestrial Outdoor, and Terrestrial Indoor Positioning Techniques," <http://www.newcom-project.eu/>.
- [33] A. Sayed, A. Tarighat, and N. Khajehnouri, "Network-Based Wireless Location," *IEEE Signal Processing Magazine*, Jul. 2005.
- [34] P. Kitanidis, "Parameter uncertainty in estimation of spatial function: Bayesian analysis," *Water Resources Research*, vol. 22, no. 4, April 1986.
- [35] H. Raiffa and R. Schlaifer, "Applied statistical decision theory," MIT Press, 1961.
- [36] L. F. Fenton "The sum of log-normal probability distributions in scattered transmission systems," *IRE Trans. Commun Systems*, vol 8, pp.57-67, 1960.
- [37] S. Kirkpatrick, C. D. Gelatt, M. P. Vecchi, "Optimization by Simulated Annealing," *Science*, vol 220, pp. 671-680, May 1983.
- [38] M. Zafer, B.J.Ko, I.Q-H.Ho, "Transmit Power Estimation Using Spatially Diverse Measurements Under Wireless Fading," *IEE/ACM Transactions on Networking*, vol. 18, pp. 1171-1180, Aug. 2010.

- [39] P. Chung, J. Bohme, C. Mecklenbrauker and A. Hero, "Detection of the Number of Signals Using the Benjamini-Hochberg Procedure," *IEEE Trans. on Signal Processing*, vol. 55, pp. 2497-2508, Jun. 2007.
- [40] M. Gudmundson, "Correlation Model in Shadow Fading Systems," in *Electronic Letters*, vol.27, Nov. 1991
- [41] I. F. Akyildiz, W.-Y. Lee, M. C. Vuran, and S. Mohanty, "Next generation/dynamic spectrum access/cognitive radio wireless networks: a survey," *Computer Networks: The International Journal of Computer and Telecommunications Networking*, pp. 2127–2159, May 2006.
- [42] Second report and order and memorandum opinion and order. in ET Docket No. 04-186 and ET Docket No. 02-380, FCC 08-260, Nov. 4, 2008.
- [43] A. O. Nasif and B. L. Mark, "Opportunistic spectrum sharing with multiple cochannel primary transmitters," *IEEE Transactions on Wireless Communications*, vol 8, pp. 5702–5710, Nov. 2009.
- [44] J. Nasreddine and J. Riihijärvi and P. Mähönen, "Location-Based Adaptive Detection Threshold for Dynamic Spectrum Access," the 4th IEEE DySPAN 2010, Singapore, 2010.
- [45] J. Nasreddine and O. Sallent and J. Pérez-Romero and R. Agustí, "Positioning-based framework for secondary spectrum usage," *Physical Communication*, vol. 1, pp. 121-133, 2008.
- [46] L. Maciel, H. Bertoni, and H. Xia, "Unified approach to prediction of propagation over buildings for all ranges of base station antenna height," *IEEE transactions on vehicular technology*, vol. 42, pp 41–45, Feb. 1993.
- [47] J. Nasreddine, N. Miliou, J. Riihijärvi, A. Polydoros, P. Mähönen, "Using Geolocation Information for Dynamic Spectruss Access in Cellular Networks," to appear in proceedings of the ACM PM2HW2N'11 (co-located with ACM MSWIM'11) and Poster Session of ACM MSWIM'11, Miami Beach, FL, USA, October 31-November 4, 2011.
- [48] B Bowu Zhang, Xiuzhen Cheng, Nan Zhang, Yong Cui, Yingshu Li and Qilian Liang, "Sparse target Counting and Localization in Sensor Networks based on Compressive Sensing", in *Proc. IEEE INFOCOM 2010*, San Diego, CA, USA, 15-19 Mar. 2010.
- [49] S. Boyd and L. Vandenberghe "Convex Optimization," Cambridge University Press, 2004.
- [50] N. Cressie, "Statistics for spatial data," *Wiley Interscience*, 1993.
- [51] R. J. Renka, "Multivariate Interpolation of Large Sets of Scattered Data," *ACM Transactions on Mathematical Software*, vol.14, pp. 139-148, Jun. 1988.
- [52] N. K. Newlands, A. Davidson, A. Howard, and H. Hill, "Validation and inter-comparison of three methodologies for interpolating daily precipitation and temperature across Canada," *EnvironMetrics* vol. 22, pp. 205-223, 2011.
- [53] W. Fa, F. Xu, Y.-Q. Jin, "SAR imaging simulation for an inhomogeneous undulated lunar surface based on triangulated irregular network," *Science in China Series F: Information Sciences*, vol 52, pp. 559-574, 2009.
- [54] J. Duchon, "Interpolation des fonctions de deux variables suivant le principe de la flexion des plaques minces," R.A.I.R.O., Analyse numérique 10, pp. 5–12, 1976.
- [55] L. Mitas, H. Mitasova, "Multivariate approximation by regularized spline with tension," Urbana, National Center for Supercomputing Applications, pp. 1–5, 1997.

- [56] D. L. Donoho, "Compressed sensing" *IEEE Trans. Inform. Theory*, vol 52, pp. 1289–1306, Apr. 2006.
- [57] I. A. Nalder, R. W. Wein, "Spatial interpolation of climatic normals: Tests of a new methods in Canadian boreal forests," *Agricultural and Forest Meteorology*, vol. 92, pp. 211-225.
- [58] M. Wellens, J. Riihijärvi, and P. Mähönen, "Spatial Statistics and Models of Spectrum Use," *Elsevier Computer Communications*, vol. 32, no. 18, pp. 1998-2011, December 2009.
- [59] R. Franke and G. Nielson, "Smooth Interpolation of Large Sets of Scattered Data," *Int. J. Numer. Methods. Eng.* vol. 15, pp. 1691-1704, Nov 1980.
- [60] MATLAB language of technical computing. Information available at: <http://www.mathworks.com/products/matlab/>
- [61] The R project for statistical computing – RandomFields package. Information at: <http://www.stat.ucl.ac.be/ISdidactique/Rhelp/library/RandomFields/html/RandomFields.html>